Design of Polymeric Substrates for Controlled Molecular Crystallization

by

Ying Diao
B.S. Tsinghua University, 2006

Submitted to the Department of Chemical Engineering in partial fulfillment of the requirements for the degree of

Doctor of Philosophy

at the

MASSACHUSETTS INSTITUTE OF TECHNOLOGY

February 2012

Author.....
Department of Chemical Engineering
September 23, 2011

Certified by.....
Bernhardt L. Trout T. Alan Hatton
Professors of Chemical Engineering
Thesis Supervisors

Accepted by.....
William M. Deen
Professor of Chemical Engineering
Chairman, Committee for Graduate Students

Design of Polymeric Substrates for Controlled Molecular Crystallization

by

Ying Diao

Submitted to the Department of Chemical Engineering on September 23, 2011, in partial fulfillment of the requirements for the degree of
Doctor of Philosophy

Abstract

It is essential to control crystallization in many areas of science and technology, such as the production of pharmaceuticals, pigments, concrete, semiconductors, as well as the formation of biominerals. In most practical circumstances, crystallization starts with heterogeneous nucleation at a foreign surface. Despite its widespread occurrence, mechanistic understanding of the role of a surface in heterogeneous nucleation is limited, especially in a solution environment.

My thesis aims at elucidating the roles of surface chemistry and nanostructure on nucleation to enable rational design of surfaces for controlling crystallization from solution. To this end, I systematically investigated the role of surface chemistry, morphology, in particular porous structures of various polymeric materials on heterogeneous nucleation using small organic molecules as model compounds.

I have demonstrated quantitatively the significance of surface chemistry to nucleation kinetics using a variety of polymer surfaces. By tuning the surface composition of the polymers, aspirin nucleation was promoted by up to an order of magnitude compared to the bulk. Further mechanistic investigations revealed that, macroscopically, it is through interfacial free energies that the surfaces influence the surface nucleation activity.

Equipped with nucleation induction time statistics as a powerful tool, I found that nanoscopic pores of 50-100 nm accelerated nucleation by up to two orders of magnitude compared with surfaces without pores. Moreover, I demonstrated for the first time that the shape of surface nanopores is essential in determining the nucleation behavior, using lithographic methods for nanopatterning the polymer films. A molecular mechanism was further proposed based on additional mechanistic investigations.

Furthermore, the nanoconfinement effect on nucleation was studied using polymeric microgels with tunable nanostructures and chemistry, whose mesh sizes range from 0.7-2 nm. We presented the first experimental evidence for the existence of an optimum confinement size at which the rate of nucleation was dramatically enhanced by up to four orders of magnitude. The degree of nucleation enhancement depends on the extent of polymer-solute interactions, whose role was elucidated from the perspective of adsorptive partitioning and nucleation-templating effect. In addition, the microgel nanostructure was also shown to play an important role in determining the crystal polymorphism of pharmaceutical compounds.

Thesis Supervisors:

Bernhardt L. Trout
Title: Professor of Chemical Engineering

T. Alan Hatton
Title: Ralph Landau Professor Professor of Chemical Engineering

Acknowledgments

I am deeply grateful for my graduate school experience at MIT Chemical Engineering Department. My five years spent here have been filled with memorable moments and intellectual enjoyment. I have received numerous advice and guidance, which supported me through difficult times and helped shaping me into an independent researcher.

First and foremost, I would like to acknowledge my thesis advisors, Prof. Bernhardt Trout, Prof. T. Alan Hatton. Over the five years of my Ph.D., Bernhardt has given me ample freedom to explore, even the little-known territories while keeping me in the right direction. By setting the standard high, he instilled in me scientific rigor and challenged me to innovate and improve continuously. I have also learnt from him to always keep the big picture in mind and to be willing to take risks, which I believe will equally benefit other aspects of my life. Alan was the first MIT professor I met back in the spring of 2006 at Beijing, when he deeply impressed me with his personable and humorous manner as an inspiring scientist. Alan has always been very encouraging and supportive. When I was upset over the research problems encountered, he went beyond his way to help me out of negative emotions. Alan has been a great source of creative ideas and novel concepts. Without his invaluable input, some research directions I have taken could have been unimaginable.

Having Allan in my thesis committee in the third year into my Ph.D has proven to be the turning point of my research. His wealth of knowledge has guided me through the depressing phase of scientific research when the input was close to infinity and the output was almost zero. He also set a great example as a caring mentor for me to look up to. I am genuinely indebted to Allan for his advice and concern over my future career development. I am also indebted to Prof. Rutledge and Prof. Cima for devoting time to serve on my thesis committee and for their insightful comments on my research.

I would like to acknowledge my collaborators, Dr. Matthew Helgeson, Dr. Takuya Harada, Surasak Chunsrivirot, Dr. Manju Sharma. Without the contributions from Matt Helgeson, several projects with polymer microgels would not have been possible. Takuya Harada supplied me with his well-facted magnetic nanoparticles, which greatly facilitated the investigation on the nanopore shape effect. Surasak Chunsrivirot and Manju Sharma help provided molecular level insight using their computational techniques.

I greatly enjoyed company and enlightening discussions with Trout, Hatton and Myerson group members, particularly Dr. Lev Bromberg, Ying Yang, Diwakar Shukla, Liang Chen, Gregg Beckham, Jie Chen, Keith Chadwick, Erik Santiso, Manas Shah, Fei Chen, Vilmali Lopez-Mejias. I am grateful to Prof. Karen Gleason and Jingjing Xu for use of their surface treatment instrumentation. I received a lot of help from Dr. Scott Speakman and Dr. Libby Shaw at the MIT CMSE for X-ray diffraction and Atomic Force Microscopy studies, and from Tim Savas and Mark Mondol at MIT MTL for their assistance with lithographic techniques.

Last but not the least, I am truly blessed with my wonderful parents. They reserved nothing to support me through the 'grill' of MIT from the other side of the planet. Although they have never attended college due to historical reasons, they have been very keen on learning about my research. With their wisdom, they help me to look at a problem from a fresh perspective and to

face a difficult situation with the right attitude. They give me all their love when I stumble and fall, and they share their deepest joy with me to celebrate my success.

Contents

List of Figures

List of Tables

Chapter 1

1. Introduction

1.1. Motivation and Objectives

It is essential to control crystallization in many areas of science and technology, such as the production of pharmaceuticals, pigments, concrete, semiconductors, optics, as well as the formation of biominerals. Everyday, there are more than 200,000 materials being crystallized all over the world. These materials can be divided into several categories, i.e., ionic crystals (e.g. salt), metallic crystals (e.g. iron), covalent crystals (e.g. diamond) and molecular crystals (e.g. aspirin). We are particularly interested in molecular crystals of pharmaceutical compounds, the crystallization process of which is very challenging to control compared with other types of crystals due to relatively weak intermolecular interactions and flexible molecular conformations.[1]

Crystallization starts with nucleation, the birth of a new phase, followed by crystal growth.[2] Nucleation is the crucial step in controlling the crystallization process. Current industrial practice for the control of primary nucleation (nucleation from a system without pre-existing crystalline matter) during crystallization from solution involves control of supersaturation generation, impurity levels, solvent composition, agitation methods, etc. Nucleation behavior remains largely unpredictable, however, due to the presence of container surfaces, dust, dirt and other impurities. This is because, in most practical circumstances, crystallization starts with heterogeneous nucleation, which occurs at a foreign surface.[2-4] -The presence of random impurities provides heterogeneous nucleation sites, as such making the control and scale-up of crystallization processes difficult. Despite widespread occurrences of heterogeneous nucleation, mechanistic understanding is limited as for the role of a surface in the nucleation process, especially in a

solution environment. My thesis aims to elucidate how various interfacial properties contribute to the nucleation activity of a substrate, for enabling rational design of substrates to control crystallization from solution. This knowledge is of broad technical implications. In particular, we intend to apply our learning to achieve reliable, efficient and economical pharmaceutical manufacturing process by engineering polymeric excipients to control the crystallization of pharmaceuticals.

Current pharmaceutical manufacturing process remains as a series of batch operations since late 19th and early 20th centuries, even though other industries have moved on to continuous manufacturing. A typical manufacturing chain can be divided into the upstream API (Active Pharmaceutical Ingredient) synthesis and the downstream pharmaceutical formulation, as shown in Figure 1-1. The downstream processes, comprised of solid-state operations, are particularly problematic. Specifically, the process operations are very sensitive to drug substance properties, which are constantly varying due to the upstream batch production mode. Consequently, the downstream processes are often plagued by poor controllability and final product uniformity. Moreover, process scaling-up, which is based on trial and error, is very costly and time-consuming. Motivated by this pressing need, Novartis-MIT Continuous Manufacturing Center aspires to transform the entire drug manufacturing chain into one seamlessly integrated continuous process (Figure 1-1). At the conjunction of the upstream API synthesis and the downstream continuous separation, my project seeks to heterogeneously crystallize API from solution on the surface of excipient, so that the subsequent API compaction, granulation, and blending with excipients can be ultimately eliminated. Furthermore, API nucleation kinetics and final crystal form, especially API polymorphs, can be tuned by controlling the excipient surface properties. Particularly, acceleration of API nucleation kinetics using designed excipients is

desired for the following reasons. First, it enables crystallization of API directly on or inside excipients to make API-excipient composite particles and helps minimize precipitation of API crystals from the bulk. Second, it facilitates the conversion of batch crystallization to the continuous mode. Crystallization from the bulk has been extensively used as a high yield and high purity separation step, but it is currently not amenable to continuous processing. This is because crystallization consists of several events with distinct time scales: sudden burst of nucleation following a long induction time, subsequent crystal growth and ripening. Besides, nucleation is extremely sensitive to experimental parameters, some of which are uncontrollable, such as the aforementioned impurity concentration, which has a huge impact on the induction time. Nucleation and crystallization on designed substrates has the promise to resolve these issues. The long induction time can be dramatically reduced using designed substrates to facilitate nucleation process. In addition, effective nucleation sites on the designed substrates render the impurities inactive, as such enhance the controllability of the process and make continuous processing possible.

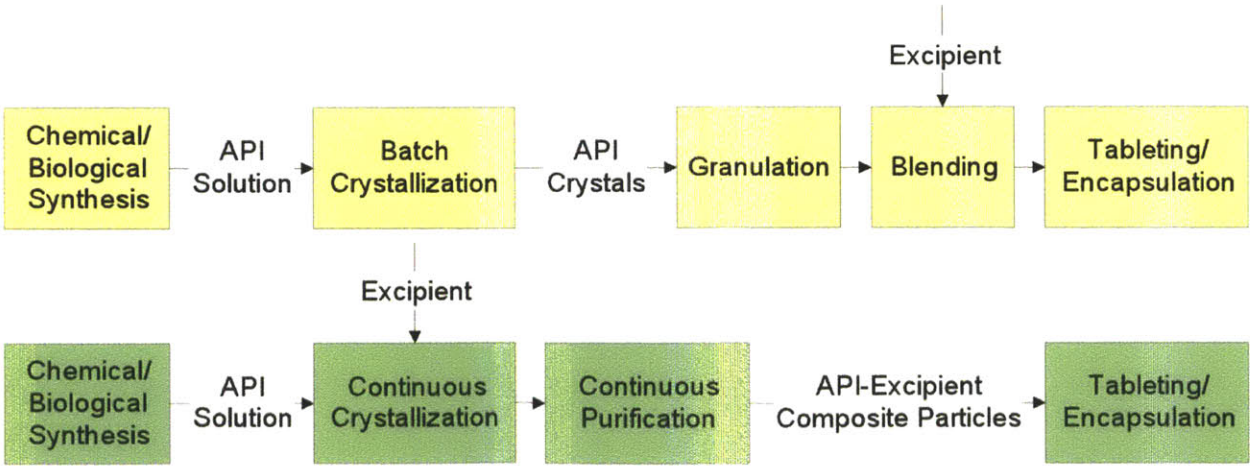

Figure 1-1 Current (top) vs. envisioned (bottom) pharmaceutical manufacturing chain

To summarize, the specific aims of my thesis are the following.

1. To elucidate the effects of key interfacial properties on nucleation for the purpose of rationally designing substrates for controlling crystallization from solution. The key surface properties include surface chemistry or interfacial interactions; surface morphology, particularly nanoscopic features (>10nm); microstructures of the interface (<10nm).
2. To promote nucleation kinetics via design of substrates
3. To control API polymorphism by tuning interfacial properties
4. To shed light on the mechanism of heterogeneous nucleation

Bio-benign polymers are chosen as nucleation templating substrates, given the wealth of polymers among pharmaceutical excipients, with a wide range of functionality, and freely adjustable morphologies and microstructures. The API model compounds selected for nucleation kinetics study are aspirin and acetaminophen, both containing functional groups characteristic of many drug molecules. Aspirin predominantly crystallizes into monoclinic form (From I), and From II, the metastable form remains elusive.[5] Acetaminophen crystallization from solution also primarily yields the monoclinic Form I, the stable form, and special procedure was needed to obtain the orthorhombic Form II.[6] Therefore, both the systems are ideal for nucleation kinetics study and the complexity of polymorphism can be avoided. For investigating polymorphism, carbamazepine and 5-methyl-2-[(2-nitrophenyl)amino]-3-thiophenecarbonitrile (ROY) were chosen as model compounds to represent both packing polymorphism (CBZ) and conformational polymorphism (ROY). CBZ possesses 4 known anhydrous forms, and ROY has 10 known forms with 7 structurally characterized.

1.2. Nucleation Theories

Nucleation is the birth of a new phase within a metastable medium. It is a first order phase transition involving an activation barrier. The kinetic theory of homogeneous nucleation from solution was originally developed by Volmer[7] in 1939 by assuming a series of sequential 'reactions' between molecular clusters of size N and N+1. The theory thus developed conceptually resembles the Transition State Theory for describing chemical reactions, except that the complex at the 'transition state' is not a covalently bonded compound, but a supermolecular assembly associated via much weaker forces for molecular crystals. Therefore, the transition pathways for nucleation could be poorly defined,[8] unlike those for chemical reactions, which result in one of the intrinsic deficiencies in the Classical Nucleation Theory. Nonetheless, it has been extensively applied till today, due to the lack of quantitative and generally applicable nucleation theories that better describe the physical phenomenon. Here, I briefly summarize the Classical Nucleation Theory below.

The Gibbs free energy change of the nucleation process incorporates contributions from the volume of the nucleus generated from the old phase, and from the new interface generated between the nucleus and the parent phase and other foreign surfaces, as described by

$$\Delta G = \Delta G_v V_n + \sum_i \gamma_{ni} A_{ni} \qquad \textbf{1-1}$$

Where V_n is the volume of the nucleus, ΔG_v the volume free energy change associated with the formation of the aggregate (negative) and A_{ni} is the area of the interface between the nucleus and the solvent or foreign surfaces, γ_{ni} the corresponding interfacial free energy (positive). When its size is small, the nucleus tends to diminish, because the interface term dominates due to a large surface area to volume ratio. When the nucleus reaches a certain critical size due to large density fluctuations in the metastable liquid, it has 50% of chance to continue its growth into a crystal,

and this radius is referred to as the critical radius R^*, corresponding to the critical Gibbs free energy change ΔG^*.

The Gibbs free energy change of heterogeneous nucleation differs from the homogenous case as there is an additional interface between the nucleus and the substrate (**Figure 1-2**).

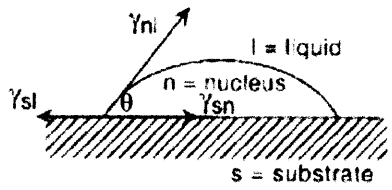

Figure 1-2 Schematic of heterogeneous nucleation from solution

$$\Delta G_{homo} = \Delta G_v V_n + \gamma_{nl} A_{nl} \quad (1\text{-}2)$$

$$\Delta G_{hetero} = \Delta G_v V_n + \gamma_{nl} A_{nl} + (\gamma_{sn} - \gamma_{sl}) A_{sn} \quad (1\text{-}3)$$

$$\gamma_{nl} \cos\theta = \gamma_{sl} - \gamma_{sn} \quad (1\text{-}4)$$

$$\Delta G^*_{hetero} = \Delta G^*_{homo} f(\cos\theta, r_n^* / R_s) \quad (1\text{-}5)$$

The extra term $(\gamma_{sn} - \gamma_{sl})A_{sn}$ in equation 1-3 tells us that when there is stronger affinity between the nucleus and the substrate as compared to the solvent and the substrate, heterogeneous nucleation is favored. The extent to which the energy barrier is lowered can be gauged using the f factor, which is the ratio of the critical Gibbs free energy changes in hetero-case and in homo-case (Equation 1-5). The f factor is a function of interfacial free energies, the shape and the curvature of the nucleus versus the substrate.

One of the limitations of the classical nucleation theory is its reliance on the concept of interfacial free energies, which assume sharply delineated nucleus interfaces. Because these interfaces become diffusive and ill-defined when the nucleus consists of only a few molecules, such as when the supersaturation is very high. In addition, the size of the nucleus is not necessarily the key and the only reaction coordinate to describe nucleation, according to recent publications by our group and other researchers.[8-12] Particularly, the orientational order of molecules within the nucleus has not been accounted in the theory, which is another key factor dictating the crystal nucleation process. To overcome these limitations, other theories have been proposed, such as the phase field theory[13], density functional theory[14,15] and two-step nucleation

theory.[10,12,16] Especially, recent years have witnessed increasing volume of evidence supporting the two-step nucleation theory,[17-19] which hypothesizes that the moleculer cluster formation via density fluctuations precedes the molecular re-orientation via structural flucturations, or more specifically, 'crystalline nucleus appears inside pre-existing metastable clusters of size several hundred nanometers, which consist of dense liquid and are suspended in the solution'.[20] Besides, Molecular Dynamics and Kinetic Monte Carlo are also powerful tools to gain a molecular level understanding of the physical picture.[8,21,22]

One of the main challenges preventing the quantitative formulation of a more physical nucleation model is that crucial questions, such as the actual shape and the interfacial features of the nucleus, or even whether the nucleus is more liquid like or resembles the final crystalline state, have not been hitherto fully addressed.[17,23,24] The difficulty lies, at least partially, in the lack of powerful techniques for detecting and imaging nucleus formation at molecular level. Although direct observation of nucleation event has been reported recently for colloidal systems,[18,23] calcium carbonate,[19,25] globular proteins,[17] there still exists a substantial hurdle to observe nucleation events in small molecular systems.

1.3. Nucleation on Substrates

Nucleation on substrates has been studied in a wide range of systems, including inorganic, small organic molecules, protein and polymer systems. The substrates applied cover self-assembled monolayers or SAM,[26-28] highly ordered pyrolytic graphite or HOPG,[29] metal surfaces such as Ag, Pt,[30] molecular single crystal substrates,[1,31-35] and crystalline or crosslinked polymer surfaces.[6,36-39] Fine control over nucleation density, spatial pattern, crystal orientation etc has been achieved for inorganic crystals,[26] but when it comes to small organic molecules, which are much more complicated due to weaker inter- and intra-molecular interactions, it is proven to be

difficult to achieve the same level of control as with inorganic crystals,[40] and therefore the focus has been primarily on polymorph screening and selective crystallization.[6,41] It is one of my thesis objectives to take the level of control for organic molecules to a higher level, such as directing nucleation kinetics, by surface design.

Generally speaking, for crystalline or molecularly structured substrates, epitaxy relationship or lattice match between the nucleating phase and the substrate has been shown to play an important role, esp. when dispersive interactions dominate.[32] Surfaces may also affect nucleation via polarization matching with the crystallizing molecule when both the surface and the crystal exhibit net dipole across the surface/crystal interface.[42,43] For amorphous substrates in organic systems, there has been some effort to selectively crystallize polymorphs by tuning the polarity or hydrophobicity of side chains,[6,36-39] but even the qualitative correlation was not clear, let alone quantitative descriptions. This can be partially attributed to the fact that the crystallization condition and surface properties were not strictly controlled, such as uncontrolled evaporation rate of solvent, and the microscopic details of the surface morphology. In fact, the role of surface morphology is much less explored, owing to the technical challenges in tuning and controlling the surface features in a systematic manner on the length scale relevant to nucleation. Although there have been a few experimental studies on the surface morphology effect on nucleation,[35,44,45] the level of control over the surface topology, particularly on nanometer scale, is far from sufficient to draw firm conclusions. Overall, there has been a lack of microscopic understanding on how the surfaces interact with the solute molecules and the role of other contributing surface properties to the nucleation process.

Recent advances in computational studies and high resolution imaging techniques have begun to shed light on the possible mechanism of surface-induced nucleation. One of the hypotheses is

that the surface enrichment effect of nucleating species contributes to nucleation promotion. A recent work from the Frenkel group[46] has shown via Monte Carlo simulations that at a disordered flat wall, a thin layer of protein is adsorbed that facilitated its nucleation near the wall, although the diameter of a critical crystal nucleus exceeds the width of the liquid layer. A similar conclusion was drawn from a previous computational study by Sear.[47] Correspondingly, there have been experimental studies reporting, for instance, the presence of an organic film facilitated the densification of calcium phosphate pre-nucleation clusters on the film, which resulted in surface-induced nucleation.[19] Interestingly, the solute layer adsorbed to the surface was observed to nucleate in a planar fashion given the anisotropic nature of the solute molecule.[17,18] When it comes to the role of surface morphology, Page and Sear found by Monte Carlo simulation of Lennard-Jones molecules that nucleation in grooves formed by two intersecting planes is many orders of magnitude faster than on a flat surface,[48] which provided an explanation to the popular practice of surface scratching for enhancing nucleation. Cacciuto and coworkers[49] used Monte Carlo simulations to show that freezing of hard sphere colloids is frustrated on curved surfaces, on which crystals cannot grow free of strain, and that the resulting defects increased the barrier to nucleation. The predicted surface curvature effect has been verified experimentally using spherical colloids as the crystallization system.[50]

Another area of increasing interest is nucleation in nanoscopic porous substrates.[51-54] Ha et al[54] showed that different polymorphs were obtained just by tuning the pore size. Frenkel[53] reviewed that protein crystallization can be speed up by using seeds with disordered pores. Porous substrates are beneficial to us because the large surface to area ratio may make heterogeneous nucleation much more favorable, thus reducing the interference from bulk crystallization. Besides, dwelling inside the pore, API properties will hardly influence the downstream

processing, which can greatly simplify the manufacturing process. In recent studies reported, the role of inner wall properties have largely been neglected. It is expected that by adjusting the pore size, pore shape and surface chemistry, a high level of nucleation control could be achieved.

Chapter 2

2. Role of Surface Chemistry in Surface-Induced Nucleation

2.1. Introduction

The presence of interfaces can modify the nucleation process through various means, such as via favorable molecular interactions with the crystallizing molecule, and a lattice match between the substrate and the compound to be crystallized. In addition, surface morphology, especially porous structures, is also shown to play an important role in controlling nucleation kinetics[51,53] and polymorphism.[52,54] The epitaxy mechanism is well developed for nucleation on crystalline surfaces, such as self-assembled monolayers or SAMs,[26,55-57] molecular single-crystal surfaces,[35] crystalline polymer surfaces,[58] etc. Relative to crystalline surfaces, amorphous surfaces such as crosslinked polymers, functionalized glass, and plastics are easier to fabricate. Furthermore, there is greater flexibility to achieve complex morphologies with various surface chemistries. Thus, amorphous surfaces have been explored extensively for the control of crystallization, especially polymorphism.[6,59,60] These studies have clearly demonstrated the important role of surface chemistry in heterogeneous nucleation, but there is little mechanistic understanding of how various surface chemistries lead to different nucleation outcomes. In addition, surface chemistry and morphology of amorphous surfaces often jointly determine the crystallization behavior. However, the contributions of these two factors are seldom quantified separately in molecular systems, and one of the two factors is often neglected when its contribution is not necessarily trivial. It is also worth noting that the role of surfaces in crystallization is rarely

investigated from the perspective of nucleation kinetics, despite the fact that nucleation is inherently a kinetic process.

In this part of my thesis, I have successfully quantified the effect of surface chemistry on nucleation kinetics and investigated the underlying molecular interactions via crystal orientation study. I also established nucleation induction time statistics as a powerful tool to gain insight into the mechanism of nucleation on controlled surfaces. With the help of this tool, I distinguished quantitatively the effects of the surface chemistry and morphology on the activity of an amorphous surface in inducing nucleation. Furthermore, I found that nanoscopic pores with the right surface chemistry facilitated nucleation significantly.

Polymers synthesized with commercially available monomers were employed to provide a wide range of surface chemistries. The polymers were crosslinked to make rigid and amorphous surfaces, Crosslinking helps to stabilize the surface chemistry in a solution environment, to minimize solvent uptake and to avoid crystallinity so that the epitaxial mechanism is negligible. Aspirin was selected as the model compound to crystallize, since it contains the carboxyl group and the benzyl ring characteristic of many organic compounds, especially drug molecules.

2.2. Experimental Methods

2.2.1. Initial Screening of Polymer Surfaces

The polymer films were synthesized by UV curing 100μl mixture of the monomer, the crosslinker ethylene glycol dimethacrylate (EGDMA) and the initiator IRGACURE 2022 sandwiched between a glass slide and a Teflon plate, with the glass slide facing the UV lamp. This configuration was adopted to avoid oxygen inhibition and surface oxidation. The molar ratio of monomer to EGDMA was 2:1. The concentration of IRGACURE 2022 was 3 v% with respect to EGDMA. UV irradiation was provided by 5000-EC UV Curing Flood Lamp

purchased from Dymax Corporation. The glass slide was silanized with vinyl trichlorosilane to yield a homogenous polymer film adhered to the glass substrate. After 4-8 min of UV irradiation depending on the polymers, the Teflon plate was removed to expose the polymer surfaces. The polymer films were then vertically immersed in 3mg/ml Aspirin-Toluene solutions and quenched from room temperature to 3°C. After 18 hours, the polymer films were taken out of the solution and washed with toluene for three times and air dried to remove the loosely attached aspirin crystals.

2.2.2. Nucleation Induction Time Measurement

The polymer synthesis procedure was modified from the one described in 'Initial Screening of Polymer Surfaces' catering to the specific requirement imposed by the nucleation induction time measurement. For initial screening, a large polymer surface area is necessary to achieve better statistics of nucleation area density, hence a large polymer film were synthesized (50 x 25mm^2). For nucleation induction time measurement, much smaller polymer surface (5 x 5mm^2) was needed in a large quantity, because 50-100 independent samples were required to obtain the probability distribution of induction time, and small solution volume was chosen to better control the impurity level in each sample so as to minimize crystallization from the bulk. Specifically, polymer plates were prepared by UV polymerizing a mixture of monomer, crosslinker divinylbenzene (DVB), initiator IRGACURE 2022, all dissolved in ethanol. The molar ratio of monomer to DVB was 2:1. The concentration of IRGACURE 2022 was 4 v% with respect to DVB. The volumetric ratio of ethanol to DVB was 2:1. 15μl monomer solution was irradiated for 20min inside each Teflon holder under N_2 protection. UV irradiation was provided by 5000-EC UV Curing Flood Lamp purchased from Dymax Corporation. After irradiation, the polymer plates were annealed at 70°C in a vacuum oven for 4h to remove the residual solvent and

unreacted monomer. For non-porous polymer synthesis, all conditions were kept the same, except for the absence of ethanol in the monomer mixture formulation. Once synthesized, each polymer plate was inserted together with the Teflon holder vertically into a 1ml Shell Vial containing 200μl 38mg/ml Aspirin solution, 38v% Ethanol-Water mixture being the solvent. For each polymer sample, 48 vials were assembled and immersed in a thermostat stabilized at 2±0.1°C, and the solution was quenched from 25°C to 2°C to achieve a supersaturation level of 4.2, where supersaturation is defined as the ratio of the initial solution concentration to the solubility at the crystallization temperature, and the solubility was expressed in mass of solute per volume of solution. The number of vials crystallized within time t_i was counted and recorded at half-hour interval at the beginning of experiment and increased to two-hour intervals at later stage when the number vials crystallized significantly reduced. All the operations involving exposing polymer surfaces, Teflon holders, aspirin solutions and shell vials to the atmosphere were conducted inside the Bio Safety Cabinet, so that the possibility of impurity contamination was reduced to the lowest level. Other efforts to reduce impurity concentration were, cleaning of Teflon holders and Shell Vials before usage and filtration of aspirin solution with Acrodisc 0.2μm PTFE syringe filter.

2.2.3. Crystal Orientation Study

Polymer films were prepared following the same procedure as described before in the initial surface screening, and the formulation of monomer mixtures was the same as that used for making nonporous polymer plates in nucleation induction time study. After preparation, the polymer films were then immersed in 20mg/ml Aspirin solution in 38v% EtOH/Water mixture, and kept at 2°C for 7h. Numerous small crystals formed on the polymer films within this time. The sample was then rinsed with deionized water for three times to remove the loosely attached

crystals, then air blew to dry. Bulk crystals were prepared under the same condition and used as a reference. The experiment was repeated three times and all the samples were analyzed with XRD.

It is necessary to remove the loosely attached crystals because a small amount of plate-like aspirin crystals tend to adhere to both sides of the substrate via the largest (100) plane identified by the optical microscope. Hence, the (100) peak intensity in Figure 10 would be slightly higher without appropriate cleaning procedure. Since the crystals attached to both sides, front being the polymer film and back the bare glass, the backside was used as the control surface during the removal of loosely attached crystals from the polymer film, so as to make sure the washing procedure was repeated just enough times to remove crystals from the backside. We also characterized both sides of the samples with XRD before and after washing and confirmed the reduction of (100) peak intensity after washing was comparable for both sides, and that other peak intensities were not significantly affected.

2.2.4. Characterization

Polymer films were analyzed with Atomic Force Microscopy (AFM), X-ray Photoelectron Spectroscopy (XPS) and contact angles with five probing liquids to obtain information on surface morphology, surface chemistry and surface energy components, respectively. AFM images were obtained with a Dimension 3100's XY closed loop scanner (Nanoscope IV, VEECO) equipped with NanoMan software. Height and phase images were obtained in tapping mode in ambient air with silicon tips (VEECO). Only height images were shown in this paper. XPS spectra were collected with Kratos AXIS Ultra Imaging X-ray Photoelectron Spectrometer with a charge neutralizer and Al X-ray source. The polymer samples were surveyed for elemental analysis followed by high resolution spectra of C 1s, O 1s, and N 1s peaks, the

deconvolution of which allows semi-quantification of surface functional group concentration. The XPS spectra of porous and non-porous polymers were compared to ascertain comparable surface chemistry. Contact angles were measured by the sessile drop method with KRÜSS Drop Shape Analysis (DSA10) system. The probing liquids include water, formamide, diiodomethane, ethylene glycol and glycerol. The surface energy components of probing liquids were taken from the Kruss Liquid Database [61,62]. A 2μl droplet of the probing liquid was lowered onto the polymer surface and images were recorded until the contact angle stabilized. At least 6 measurements were performed to obtain an average contact angle for each probing liquid, and in each measurement a fresh polymer surface was used.

The aspirin crystals were characterized with Optical Microscope to determine the nucleation density and crystal morphology. The crystal orientation was studied with Powder X-ray Diffraction to obtain the specific crystallographic planes attached to the polymer film. The optical images were captured by a Zeiss Axiovert 200 microscope in transmission mode. The X-ray diffraction patterns were recorded with a PANalytical X'Pert PRO Theta/Theta Powder X-Ray Diffraction System with Cu tube and X'Celerator high speed detector. No less than ten XRD patterns were collected for crystals on each polymer sample.

2.3. Results and Discussion

A surface is nucleation active when it is rich in nucleation sites that decrease the nucleation barrier significantly for the active pharmaceutical ingredient (API) of interest. The heterogeneous nucleation rate, or the number of nuclei surpassing the nucleation barrier per unit area per unit time, is a direct measure of the API nucleation activity of a surface. However, it is difficult to measure the nucleation rate directly for molecular crystals because the nuclei constituted by small organic molecules may be too small to observe with the current analytical tools, as such,

the nucleation rate has generally been approximated with the number of detectable crystals per unit area per unit time.[2,7] Instead of measuring the nucleation rate directly, nucleation density and induction time probability distribution are used to evaluate the API nucleation activity of the surface. To rapidly screen a large number of polymer samples in search for nucleation active surfaces, we established a simple method to measure the nucleation area density on a variety of polymer films. The best candidates that emerged from the initial screening were further studied, with nucleation induction time used to quantify the nucleation activity.

2.3.1. API Nucleation Activity of Surfaces via Nucleation Density

Initial surface screening was performed by comparing the nucleation area density on polymer films after a fixed period of crystallization time. The nucleation area density, approximated by the number of crystals observed under the optical microscope per unit area of the substrate, is indicative of the average nucleation rate over this period of time. Crosslinked polymeric films for the heterogeneous nucleation of aspirin crystals were prepared using UV curable monomers of a wide range of functionalities. Many of these monomers can be polymerized into pharmaceutical excipients or drug delivery carriers, but for comprehensiveness, the selection was not restricted to this criterion, The selected monomers contain functional groups that are expected to interact with aspirin via either hydrogen bonds or pi-pi stacking, and they were divided into five groups according to the main functionality characterizing the monomer (Figure 2-1). Group (a) includes 2-hydroxyethyl methacrylate (HEMA), acrylic acid (AA) and methacrylic acid (MAA) which contain carboxyl or hydroxyl groups that provide both hydrogen bond donors and acceptors. Groups (b) and (c) include tertiary amides and amines that are rich in hydrogen bond acceptors, i.e., N,N,-dimethylacrylamide (DMAA), vinylpyrrolidone (VP), and 4-acryloylmorpholine (AM) in group (b) and 4-vinylpyridine (4VP), vinylimidazole (VI), and 2-dimethylamino ethyl

methacrylate (DMAEMA) in group (c). Monomers in group (d), methyl methacylate (MMA) and tert-butyl methacrylate (t-BuMA), contain the carboxylic acid ester functionality that is also seen in aspirin. In group (e) are two phenyl-ring-containing monomers, styrene (STY) and chloromethylstyrene (CIMSTY). The polymer films were synthesized by UV curing of a mixture of a monomer and the crosslinker ethylene glycol dimethacrylate (EGDMA), then immersed in supersaturated aspirin-toluene solution to perform static isothermal crystallization. The crystal densities on the polymer films were found to be vastly different, as shown in Figure 2-2. In addition, the morphology of crystals on the polymer films also differed from the hexagonal bulk crystals (Figure 2-3), indicating the influence of polymer surfaces on the crystal orientation, which was later studied via X-ray diffraction (XRD).

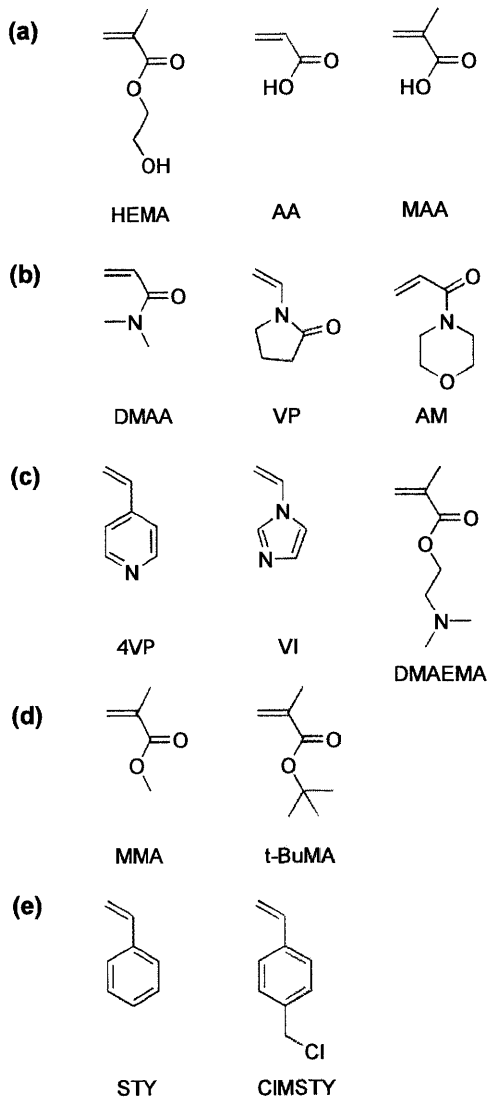

Figure 2-1. Chemical structures of monomers investigated in the initial screening. Monomers containing (a) carboxyl or hydroxyl groups, (b) tertiary amide functionality, (c) tertiary amine functionality, (d) carboxylic acid ester group, and (e) phenyl ring.

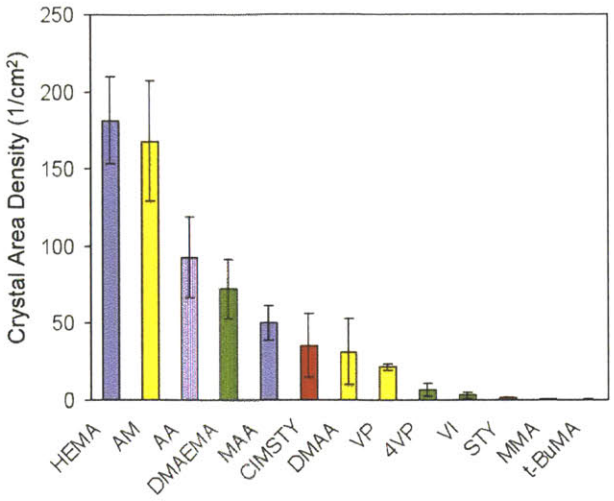

Figure 2-2. Nucleation density of aspirin on polymer films. Columns representing polymers from groups (a), (b), (c), (d), (e) are colored blue, yellow, green, pink, and red, respectively. Error bars were derived from three repeats.

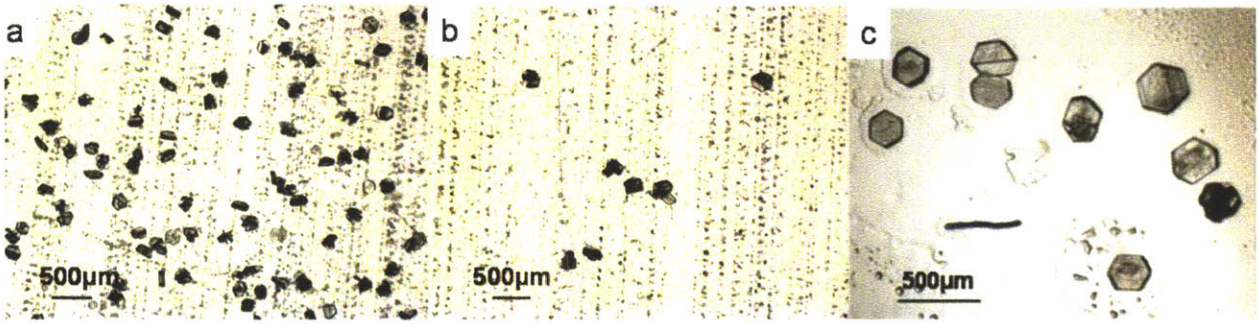

Figure 2-3 (a) and (b) depict aspirin crystals on polymer films AM and DMAEMA, respectively. (c) shows aspirin crystals crystallized from the bulk of 3mg/ml aspirin/toluene solution.

From the initial surface screening, we observed that compounds from the same group do not necessarily have the same effects on the nucleation density (Figure 2-2), which is not unexpected. As mentioned before, the polymers tested were divided according to the main functionalities contained, which implies that the chemical characteristics of the group could not completely represent those of individuals (Figure 2-1). This observation reaffirmed that heterogeneous nucleation is highly sensitive to the surface chemistry, which is in line with observations by other researchers.[6] Nonetheless, grouping the polymers was helpful because a general trend was observed that compounds from group (a) and (b) induced nucleation more effectively than those from group (d) and (e). Specifically, polymer films made from HEMA,

AM and AA, which are polar and contain multiple hydrogen-bonding sites, exhibited relatively high nucleation activities compared with the less polar films from groups (d) and (e). Supposedly, the carboxylic acid group on the surface of AA and MAA is able to interact strongly with aspirin by forming cyclic dimers of carboxylic acids. However, these two polymers did not exhibit the anticipated high API nucleation activity in the initial screening. One possible reason is that the crosslinker EGDMA formed hydrogen bonds with the carboxyl groups in AA and MAA, and thus reduced the extent of interaction with aspirin. To eliminate this possibility and to increase the exposure level of carboxyl groups, the crosslinker was changed to divinylbenzene (DVB), and 2-carboxyethyl acrylate (CEA), an analog of AA and MAA, was used instead in later studies. X-ray Photoelectron Spectroscopy (XPS) results showed that the exposure level of the carboxyl group on the polymer surface made from CEA and DVB is 1.5 and 1.8 times higher than that on AA and MAA surfaces, respectively. To further quantify the effect of these polymers on nucleation kinetics and to gain insight into the nucleation mechanism, nucleation induction time measurements were performed using polymers with promising functionalities and negative controls. Three polymers exhibited high nucleation activity from the initial screening results were selected, and one polymer that didn't induce nucleation was chosen as a negative control. Four out of thirteen polymers were chosen for the induction time study because 1) it is time-consuming and labor-intensive to systematically quantify induction time probability distribution; 2) four compounds were sufficiently representative and diverse to gain insight into the polymer-induced nucleation and the added benefit is small to study all thirteen polymers.

2.3.2. Nucleation Induction Time Statistics

Nucleation is an activated process, the kinetic barrier to which determines the time it takes for sufficiently large fluctuations to occur to bring a supersaturated solution into growing regions of

the new phase.[11] This period of time is also known as the nucleation induction time and is defined as the time elapsed prior to the formation of a detectable amount of the new crystalline phase.[7] Nucleation induction time is a good indicator of the API nucleation activity of a surface because it can be shortened dramatically when the presence of a surface lowers the kinetic barriers to nucleation. The experimental measurement of nucleation induction time offers several challenges. Firstly, the stochastic nature of nucleation events requires statistical measurements of the induction time to be performed under exactly the same conditions. Secondly, induction time is extraordinarily sensitive to the temperature, the initial concentration, the supersaturation level, the cooling rate and other external disturbances. In particular, it is often, if not always, strongly affected by unregulated impurities in the solution. This trait of induction time requires precise control of the nucleation conditions and the purity of the system. Despite careful design, such as nucleating in nanoliter droplets,[63] the interference of impurities is still hard to eliminate. However, impurities in the system could be inactivated when nucleation preferentially occurs on designed surfaces with high API nucleation activity.

To conduct induction time measurements, polymer plates were prepared by UV polymerization of the mixture of a monomer and the crosslinker divinylbenzene dissolved in ethanol held by a Teflon holder. Subsequent drying under vacuum removed residual solvent and unreacted monomer. Monomers used to synthesize polymer plates were 4-acryloylmorpholine (AM), 4-hydroxybutyl acrylate (HBA), 2-carboxyethyl acrylate (CEA), and styrene (STY), shown in Figure 2-4. HBA and CEA were used as analogues of HEMA and AA, correspondingly, because the crosslinked polymer plate made from HEMA easily cracks after UV irradiation, and CEA was used for the aforementioned reasons. AM, HBA, and CEA served as positive controls in the induction time study based on the initial screening results (Figure 2-1), whilst STY served as a

negative control. Each polymer plate was inserted together with the Teflon holder vertically into a 200μl aspirin solution, and then the solution was quenched by cooling to achieve a supersaturation level of 4.2. The starting concentration was chosen such that the supersaturation produced was high enough to give reasonably short induction times but low enough to suppress bulk nucleation. Forty-eight vials of each polymer sample were tested simultaneously and the fraction of vials in which crystallization occurred was recorded as a function of time to produce a plot of cumulative probability distribution of induction time, as shown in Figure 2-5a.

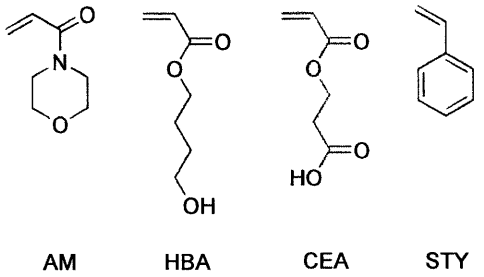

Figure 2-4. Monomers used for the preparation of polymer surfaces in the nucleation induction time study.

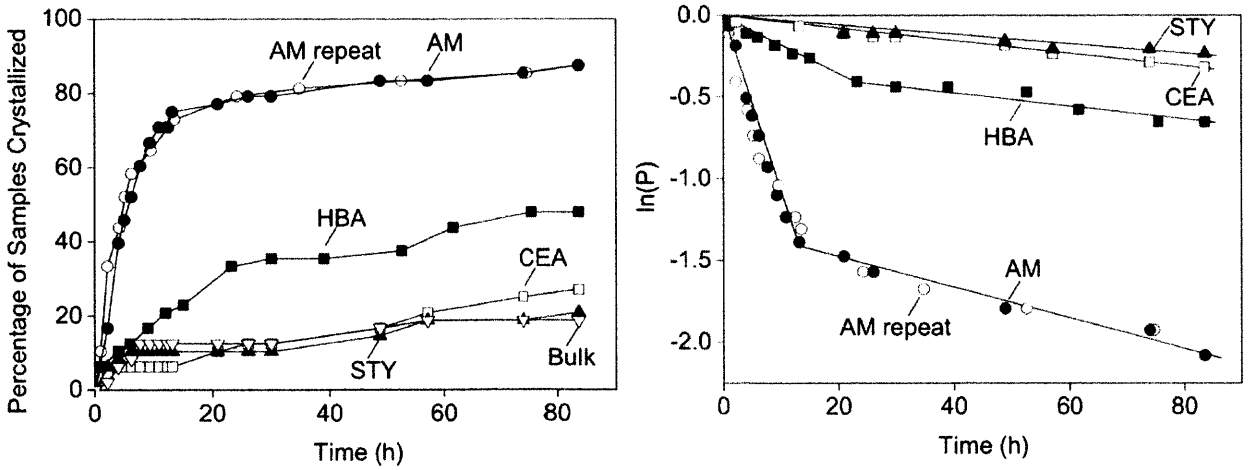

Figure 2-5. Cumulative probability distribution of nucleation induction time (left) and statistical analysis on the same data sets (right). The experiments were performed with polymers synthesized via UV polymerization with solvent ethanol. Crystallization was conducted at supersaturation S=4.2. The linear regression follows the formula $\ln(P)=-t/\tau$ to obtain the average induction time τ. P is the probability for no crystallization event to occur within time t.

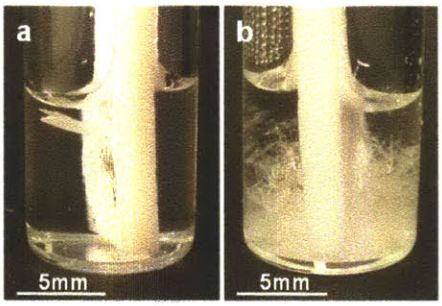

Figure 2-6. Comparison of aspirin crystals from (a) the surface of AM, and (b) the bulk with Teflon only.

The probability for a nucleation event to occur within time t was approximated by the fraction of vials in which crystallization occurred within time t, assuming all the samples with the same type of polymer plates were identical. This approximation is appropriate when (1) the heat transfer rate is sufficiently high that the time taken for the solution to achieve the desired level of supersaturation is negligible, and (2) crystal growth is sufficiently fast that the time taken for a nucleus to grow into a detectable size is minimal compared with the nucleation induction time. Both conditions were satisfied in this study, since the small solution volume and the high coolant flow rate enabled fast heat transfer, and centimeter-sized aspirin crystals grew within minutes, which is sufficiently short compared with ten- to hundred-hour-long induction times. To obtain the average induction time τ, statistical analysis was performed on the induction time data based on the assumption that nucleation events follow the Poisson distribution. According to the Poisson distribution, if the expected number of occurrences in the interval of interest is λ, the probability of k occurrences is $f(k;\lambda)=\frac{\lambda^k e^{-\lambda}}{k!}$. By setting k=0 and $\lambda=t/\tau$, the probability of observing no nucleation event (P) within time t is $P=\exp(-t/\tau)$. This expression is consistent with the formula used by other researchers who have assumed nucleation follows first-order kinetics.[63-65]

Figure 2-5 shows that polymer sample AM was most effective in inducing aspirin nucleation with the shortest induction time, followed by HBA, CEA and STY. As expected, the negative

control STY was inactive since the solutions with STY crystallized at almost the same rate as did the bulk samples, where only the Teflon holders were inserted into the solution. Figure 2-6 shows typical scenarios observed in vials with the polymer (a) and without (b). Clearly, a few large crystals nucleated and grew from the polymer surface, while numerous small crystals precipitated out from the bulk. This implies that nucleation on polymers occurred much earlier than in the bulk and the rapid crystal growth depleted aspirin molecules from the solution, which suppressed crystallization from the bulk. A statistical analysis revealed good linear fits of the induction time data obtained with STY and CEA (Figure 2-5b). However, for AM or HBA, there was a dramatic change in slope, marking a significant slowdown in the nucleation rate during the later stages of the experiment. To determine the reason for this behavior, induction time measurements were repeated for AM and it was found that, as in the first trial, one sixth of the solutions crystallized consistently at a much lower rate. This observation implies that the change in the nucleation mechanism was a result of the variability in polymer plates. The morphological differences in the polymer samples were characterized by AFM, showing that most of the effective polymers exhibited surface pore structures, while less effective surfaces were mostly non-porous. Representative samples are shown in Figure 2-7a, b. The pores found on effective polymer sample AM were around 100nm in width and 4nm in depth (Type I pores). Comparatively, polymer sample HBA exhibited pores about 50nm in width and 5-8 nm in depth (Type II pores). A third type of pore (Type III) found on some of the CEA and STY as well as on AM and HBA was much larger in size and much lower in area density, as shown in Figure 8. The reason for the bimodal pore size distribution on AM and HBA is not clear. The surface features of all the samples are summarized in Table 1. The possible pore formation mechanism was attributed to polymerization-induced phase separation. A mixture of monomer and

crosslinker dissolved in ethanol was subjected to UV irradiation to initiate the polymerization. With an increase in polymer molecular weight during the polymerization process, an increasing dynamic asymmetry[66] between solvent molecules and the polymer leads to nucleation and growth of solvent-rich regions within the polymer matrix. Subsequent evaporation of the solvent during the vacuum drying leaves pores on the polymer films. A common feature shared by most porous surfaces is a raised edge surrounding the pore region, probably due to an eruptional behavior caused by fast solvent evaporation under vacuum.

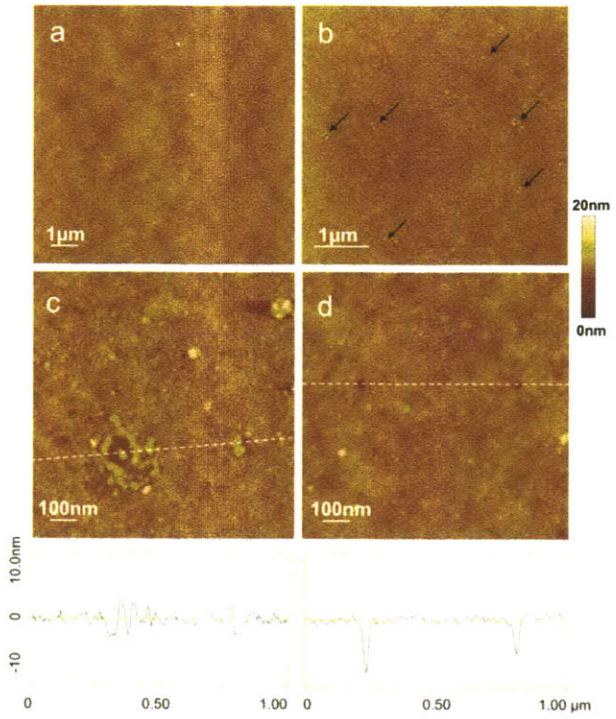

Figure 2-7. AFM images of type I pores on AM and type II pores (Table 2-1) on HBA synthesized with solvent ethanol and used in the induction time study. (a) The smooth surface of polymer sample AM less effective in nucleating aspirin. (b) Polymer sample AM more effective in nucleating aspirin. The pores, around 100nm in width, are indicated by arrows. (c) Higher resolution image of a pore found on effective AM. The pore is around 100nm in width and 4nm in depth. (d) Polymer sample HBA, with two pores of around 50nm in width and 5-8nm in depth. The cross-sectional depth profiles along the dotted lines on Figure 7c and 7d are shown below the respective AFM images.

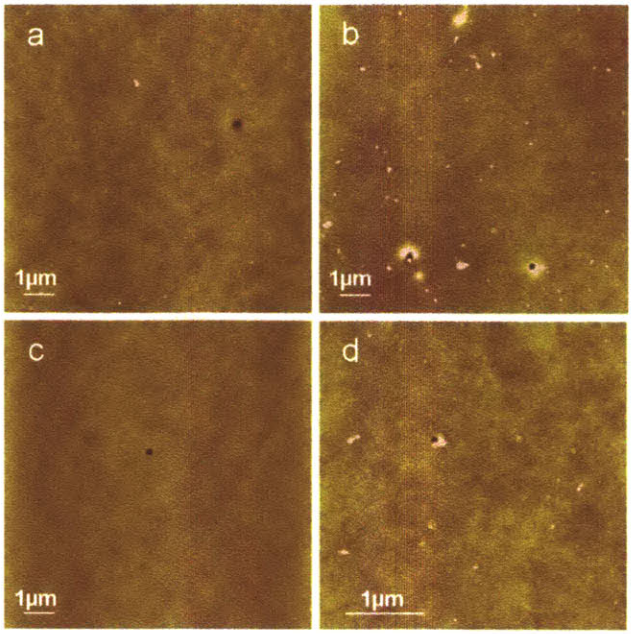

Figure 2-8. AFM images of type III pores (Table 2-1) on polymer samples prepared with solvent ethanol and used in the induction time study. (a) CEA (b) STY (c) AM (d) HBA. The bright dots are impurities adhering to the surface during sample preparation. The dark dots signify pores on the polymer surface.

Pore	Polymer	Pore Density ($1/100\mu m^2$)	Pore Width (nm)	Pore Depth (nm)
Type I	HBA	100~150	35~60	5~8
Type II	AM	20~50	70~120	4~10
Type III	AM, HBA, CEA, STY	≤1	200~400	10~50

Table 2-1. Summary of porous structure on polymer samples prepared with solvent ethanol.

To differentiate the contribution of the nanoscopic pores from that of the surface chemistry to the API nucleation activity of the polymer surfaces, each of the forty-eight AM and HBA samples was divided into two sets for statistical analysis, one comprised of polymers with pores, the other with non-porous polymers. As summarized in Table 2-2 for the case of S = 4.2 (the S = 4.75 results will be discussed later), the aspirin nucleation rate tripled in the presence of nonporous polymer AM, and polymer AM with pores further enhanced the nucleation rate up to twenty-six times that without pores. Similarly, the non-porous HBA showed no effect on the aspirin nucleation rate, whilst the nanoscopic pores on polymer HBA dramatically improved its

effectiveness in promoting aspirin nucleation. Although type III pores were found on some of the CEA and STY surfaces, it may not have affected their API nucleation activities, given that no apparent slope changes were observed from the statistical analysis. In that case, a comparison of the average induction times not affected by pores (Table 2-2) may indicate that AM is the most effective surface chemistry in inducing aspirin nucleation, followed by CEA, while HBA and STY remain ineffective. To further verify the effect of surface chemistry, induction time measurements were conducted with non-porous polymer surfaces.

Polymer type	Superaturation	Average induction time τ (h)			
		AM	CEA	HBA	STY
With pores	S=4.2	4.3±0.2	252±8	12.6±0.4	340±20*
Without pores	S=4.2	111±3		330±30*	
Without pores	S=4.75	38.1±0.3	113±3	210±30*	242±5*

Table 2-2. Average nucleation induction times of aspirin with the presence of polymers with and without pores. The standard errors of average induction times were calculated from the standard error values for the slopes regressed from the ln*P* vs. *t* plots (Figure 2-5, Figure 2-9) following the formula ln*P*=-*t*/τ. *The average induction time not statistically different from that of the bulk.

2.3.3. Effect of Surface Chemistry on Nucleation

Non-porous polymer samples were prepared by polymerizing mixtures of the monomer and the crosslinker without ethanol, in other words, by bulk polymerization. The surface morphology was characterized by AFM and the surface roughness was between 5 and 9 Å for all the non-porous samples, similar to roughness of the polymers with pores. The surface chemistry of non-porous polymers was also shown by XPS to be the same as that of porous samples, although we couldn't exclude the possibility that the local surface chemistry on the pore wall might be different. Here we assume that the difference between the polymer surfaces prepared with or without solvent lies mainly in the pore structure.

Induction time measurements were conducted with non-porous polymers at a higher supersaturation level (S) of 4.75 rather than the 4.2 used previously to further separate the performance of the polymer substrates. The nucleation induction time study revealed a similar distinction in the API nucleation activities of the four samples, with AM still the highest followed by CEA, while HBA and STY turned out to be ineffective with performances barely distinguishable from that of the bulk (Figure 2-9a). This result provided strong evidence that surface chemistry was responsible for the API nucleation activity of the substrates. Later in the paper, the surface chemistry effect is further investigated in terms of a model based on interfacial free energy components. Figure 2-9b illustrates that the experimental data from samples AM and HBA followed the Poisson distribution faithfully, which supported the hypothesis that the previous changes in slope (Figure 2-5b) were due to the variation in the polymer morphology. Although the nucleation kinetics of HBA and bulk samples deviated slightly from the Poisson distribution (Figure 2-5a), their average induction times were not statistically different from that of STY (Table 2-2). Therefore the nonporous HBA and STY couldn't be considered as nucleation-active for aspirin, which is consistent with previous observations at lower supersaturation. For polymer sample AM, even at a higher supersaturation, aspirin nucleation induced by non-porous polymers was still much slower than that by porous polymers. Similarly, compared with the ineffective nonporous polymers, HBA was activated even at lower superaturation by 50nm pores on the surface. Both these examples attest to the fact that the nanoscale pores on the surfaces of AM and HBA enhanced nucleation kinetics and significantly increased the API nucleation activity of these polymers. However, the pores found on polymer samples STY and CEA, with a size of several hundred nanometers and a much lower area density, were not as effective, if at all.

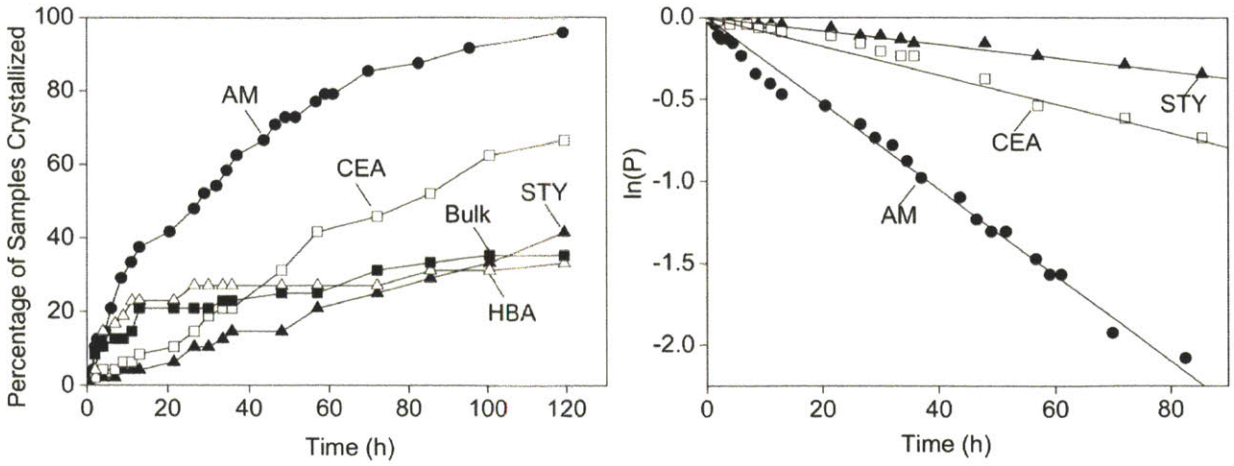

Figure 2-9. Cumulative probability distribution of nucleation induction time (left) and statistical analysis on the same data sets (right) obtained with polymers synthesized via bulk polymerization. Crystallization was performed at supersaturation S=4.75. The linear regression in 10(b) follows the formula $\ln(P)=-t/\tau$ to obtain the average induction time τ. P is the probability for no crystallization event to occur within time t. Since the STY, HBA and bulk samples produced comparable overall nucleation rates judged from the regressed average induction time (Table 2), thus only the STY data were displayed in 10(b).

Nanoscale pores have been shown to affect the nucleation process either in solution[67,68] or in the melt.[69,70] However, in contrast to this study, pore sizes less than 10nm were generally needed to observe any confinement effect on nucleation kinetics or melting/freezing behavior, particularly for small organic molecules. Researchers also found that pores less than 50nm could influence the polymorphic outcome of small molecular compounds.[54,71,72] An explanation for the mechanism for the effect of pores on nucleation commonly preferred links the pertinent pore size to the critical nucleus size of the crystallizing compound. The problem with this approach based on the classical nucleation theory is that it is hard or impossible to compute an accurate critical nucleus size and it is unclear to what extent size is the key order parameter for nucleation in a confinement environment. Several factors other than pore size may come into play, such as the surface chemistry and the geometry of the pore. Firstly, the pore wall may exhibit different functionalities from those on the flat surface due to its contact with the solvent ethanol during the pore formation, while the rest of the polymer surface was in a nitrogen environment during the

synthesis. Its contact with ethanol may have facilitated the exposure of polar functional groups to the pore interior and hence enhanced the interaction between the pore wall and aspirin. However, such differences in the surface chemistry were not detected by XPS perhaps because the pore area densities were too low. The effect of surface chemistry on nucleation was further investigated by preferred crystal orientation on flat polymer surfaces and the interfacial free energy approach as discussed later in the paper. Secondly, the pore shape may play an important role in promoting nucleation. Recently, Page and Sear found by Monte Carlo simulation of Lennard-Jones molecules that nucleation in grooves formed by two intersecting planes is many orders of magnitude faster than on a flat surface.[48] Moreover, when the wedge angle was the same as an intrinsic angle of the crystal, nucleation rate was maximized. It was also shown experimentally that particular polymorphs of organic crystals grew preferentially in orientations guided by ledges on cleaved single crystal surfaces when the dihedral angle of the ledge matches that of the prenucleation aggregate,[35] although the underlying assumption that the prenucleation aggregate is multifaceted has not been verified. Besides, it was also not clear if the micron-sized ledges as cleaved preserved their shape on a nanometer scale comparable to the prenucleation aggregate. Nonetheless, these studies clearly demonstrated the important role of surface geometry on the nucleation behavior. In this work, most pores on all polymer surfaces were conical in shape, with cone angles ranging from 130° to 170°, as revealed by the depth profiles measured via AFM. Some of the pores observed on the polymer AM surface appeared to be truncated cones with base angles ranging from 150° to 170°. Nucleation may occur favorably in such cavities rather than on a flat surface because the free energy penalty for creating a new interface during the nucleus formation is lowered due to increased contact area of the cavity surface with the nucleus, when the nucleus preferentially interacts with the cavity wall.

However, if the nucleus does not match perfectly the geometry of the cavity, the formation of defects during crystal growth would introduce additional free energy cost, which implies there may exist an optimum conical pore aperture that promotes nucleation to the largest extent. For further investigation on pore-induced nucleation, a method should be developed to better control the geometry, the dimensions, the surface chemistry and the area density of the pores, which will be discussed in future publications.

In summary, we employed nucleation induction time statistics to quantify the API nucleation activity of polymers with various surface chemistry and morphology. Differences in polymer surface chemistry led to distinct nucleation activities, and polymer AM performed best for aspirin crystallization from 38v% EtOH/Water, followed by CEA. On the other hand, polymer samples with less polar functionalities, STY and HBA were ineffective under the same conditions. We also found the presence of specific pore structures on polymer samples AM and HBA greatly improved the API nucleation activity of the polymers, but less dense pores on polymer samples CEA and STY did not seem to have an effect. However, further study is needed to understand the effect of pore size, pore shape, pore chemistry and area density on the effectiveness of a porous substrate in facilitating nucleation.

2.3.4. Preferred Crystal Orientation

A number of mechanisms which attempt to describe the effect of the substrate on nucleation have been proposed. Of these mechanisms, epitaxy or charge/polarization matching[1,42,73] is not applicable to our systems. The mechanism, complimentary functional group interactions[43], was investigated through studies of preferred crystal orientation. The purpose of this study was to elucidate molecular interactions between the aspirin crystal and polymer surfaces. From the manufacturing perspective, it is desired to control the crystal morphology by designing the

nucleation substrate. Researchers[55,58] have oriented calcite crystals via electrostatic interactions and lattice matches between the crystal and the substrate in aqueous systems. However, there is little study on the orientation of small organic molecules on solid substrates, especially amorphous substrates.

We have investigated preferred orientations of aspirin crystals on polymer films AM, CEA and HBA. The negative control sample STY was not included in the study since it was shown to be ineffective in this particular system, according to the nucleation induction time results. Aspirin crystals nucleated heterogeneously on the polymer films were prepared following the same procedure as described in the initial surface screening. The preferred orientation of the aspirin crystal with respect to the top surface of the polymer film was identified with XRD by comparing the diffraction pattern with that of bulk crystals. The representative patterns are shown in Figure 2-10. The configuration in the XRD measurement was such that only the crystal planes parallel to the polymer film surface were seen by the X-ray, and thus the peak that was significantly more intense relative to the reference peak corresponds to the preferred nucleation face. A quantitative analysis of crystal orientation (Table 3) was performed by normalizing the measured peak intensities with the reference peak intensities from the bulk sample, in which aspirin crystals were randomly oriented. The method is described elsewhere.[55]

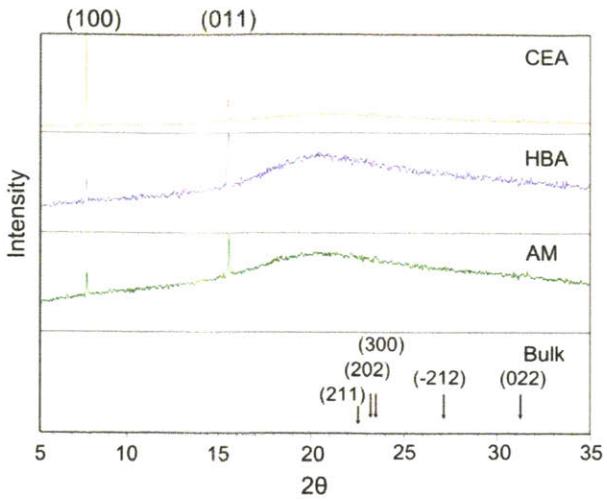

Figure 2-10. X-ray diffraction patterns of aspirin crystals nucleated from polymer surfaces and in the bulk. The (hkl) indices of the crystallographic planes are labeled over their corresponding peaks. The broad peak around 20° seen in the top three diffraction patterns is attributed to the amorphous polymer film. Two primary peaks were observed in all four patterns, one around 7.7°, and the other around 15.6°. Since the (011) peak is separated from the (002) peak by a 2θ angle of only 0.17 degree (Primary reference: Calculated from CSD using POWD-12++; Structural reference: Harrison, et al., Faraday Discussions. 2003.[74]), the 2θ angle differences between the two primary peaks were carefully measured to determine that the peak around 15.6° matched with the (011) plane.

Polymer film	(100), %	(011), %
CEA	**69.3**	30.7
HBA	20.4	**79.6**
AM	24.8	**75.2**

Table 2-3. Percentages of aspirin crystals in different orientations (hkl) on polymer films, estimated from the XRD data by normalizing the measured peak intensities with the reference peak intensities from the bulk sample.

It is apparent from Figure 2-10 and Table 2-3 that the aspirin (011) face grows preferentially from polymer films HBA and AM, while the (100) face predominates on CEA. This is consistent with the observation via optical microscopy (Figure 2-11). The possible underlying molecular interactions that steer the crystal orientation can be inferred from the molecular structure of the corresponding crystal facet (Figure 2-12) and the polymer surface. The carbonyl groups on the aspirin (100) plane provide predominant hydrogen bond acceptors, and thus impart slight Lewis basicity to the facet. Comparatively, the (011) plane is more acidic with the presence of

undimerised carboxylic acid functional groups. Since the CEA polymer surface mainly bears carboxyl groups, it is sensible for it to nucleate the (100) facet via hydrogen bonds with carbonyl groups. The AM and HBA polymer surfaces which are rich in hydrogen-bond acceptors could preferentially nucleate the (011) facet through hydrogen bonds with carboxyl groups. This hydrogen donor-acceptor relationship is consistent with our experimental observations. It is also worth noting that out of the three main facets present in the aspirin crystal crystallized from 38% ethanol-water, both (100) and (011) are much more polar than (002), as shown experimentally by Heng, et al. via XPS as well as contact angle measurements.[75] This observation indicates that all three polymer films tend to nucleate polar facets of aspirin.

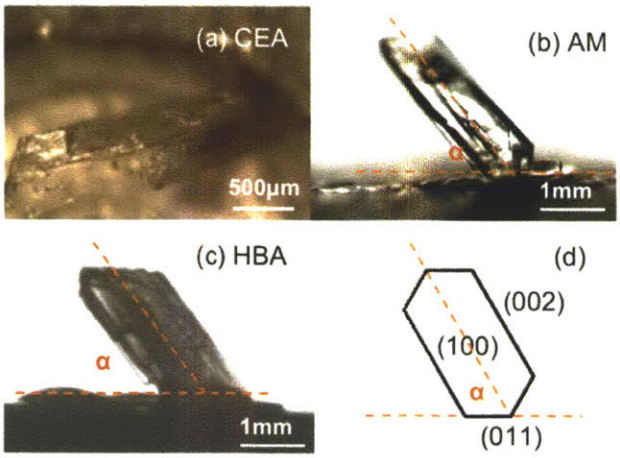

Figure 2-11. Representative optical microscope images of the aspirin crystal grown from polymer surfaces. (a) Aspirin crystals lying on the (100) face on polymer plate CEA. (b, c) Aspirin crystals standing on polymers AM and HBA. The tilt angle α of the (100) face with respect to the face in contact with the polymer is approximately 60°, which is very close to the dihedral angle between the (002) face and the (011) face. (d) Schematic of the crystal habits of aspirin.

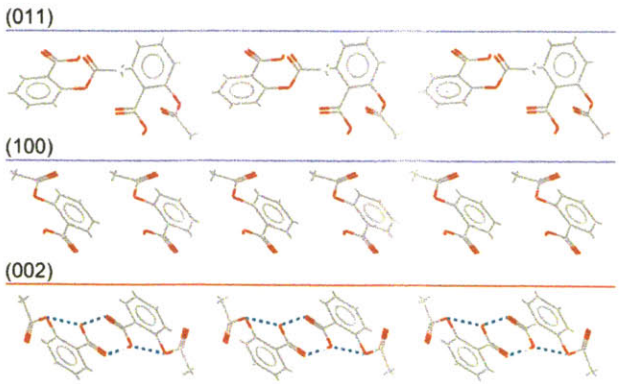

Figure 2-12. Molecular structures of (011), (100) and (002) facets of aspirin crystal. The blue line indicates the facet is polar, and red non-polar.

Preferred crystal orientation was also tested on polymer films with pores. We observed the same average crystal orientation on polymer surfaces with pores as those without pores. This observation does not necessarily mean the presence of pores has no effect on the crystal orientation. Instead, it is probably due to the low area density of surface pores (Figure 2-7, Table 2-1) that the overall crystal orientation remained unaffected. The current method we used for probing preferred crystal orientation is only applicable to large homogeneous surfaces. For future investigations, characterization techniques such as high resolution Atomic Force Microscopy will be explored that allow determination of crystal orientation in nanoscopic local domain.

2.3.5. Interfacial Free Energy Approach

The objective of this approach is to explain qualitatively the surface chemistry effect on the kinetics of heterogeneous nucleation. The parameter of choice is θ, the contact angle between a cap-shaped nucleus and a flat substrate in the solution environment, as depicted in the classical nucleation theory (CNT) shown in Figure 2-13. According to CNT, the smaller θ is, the greater the affinity between the nucleus and the substrate in the crystallizing medium, and the lower the free energy barrier for heterogeneous nucleation.[7] θ is used to denote the CNT contact angle in the rest of the paper.

Since this approach is based on the classical nucleation theory, it is assumed 1) the nucleus is cap-shaped rather than multi-faceted 2) the boundary of the nucleus is well defined rather than diffusive; 3) the microscopic interfacial free energies are the same as that of macroscopic crystals. It has been shown by many researchers that these assumptions may be nonphysical.[10-12,16] Given its limitations, this approach is not intended for a precise description and prediction of the effect of substrates on heterogeneous nucleation. Instead, it is utilized to estimate

qualitatively the extent of interactions between the solute and the substrate in the solution environment from the perspective of interfacial free energies and to explore the correlation between this interaction with the nucleation activity of the surface. To realistically model surface-induced nucleation, a complete molecular level understanding is a pre-requisite, for which molecular dynamic simulations are performed and will be discussed in future publications.

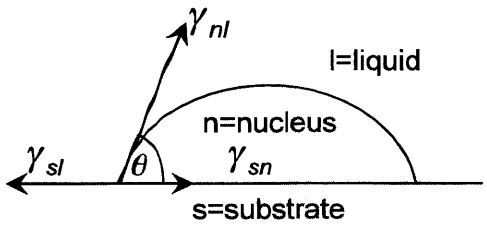

Figure 2-13. Contact angle θ in the classical nucleation theory (CNT). γ_{nl}, γ_{sl}, and γ_{sn} refer to the interfacial free energies between the nucleus and the liquid, the substrate and the liquid, and the substrate and the nucleus, respectively.

θ can be calculated from the interfacial free energies γ_{nl}, γ_{sl}, and γ_{sn} using Young's equation.

$$\cos\theta = \frac{\gamma_{sl} - \gamma_{sn}}{\gamma_{nl}} \qquad \textbf{Equation 2-1}$$

According to the geometric mean approach,[76] γ_{nl}, γ_{sl}, and γ_{sn} are related to surface energy components γ_d, γ_p, γ_h, which denote the surface energy contributions from the dispersive, permanent dipole-dipole and hydrogen binding interactions, respectively, viz.,

$$\gamma_{AB} = \gamma_A + \gamma_B - 2\sqrt{\gamma_A^d \gamma_B^d} - 2\sqrt{\gamma_A^p \gamma_B^p} - 2\sqrt{\gamma_A^h \gamma_B^h} \qquad \textbf{Equation 2-2}$$

The surface energy components of the polymer surface (γ_s^d, γ_s^p, γ_s^h) were obtained by measuring the contact angles (θ') between the polymer surface and five probing liquids of known surface energy (γ_l) and surface energy components (γ_l^d, γ_l^p, γ_l^h). The values of γ_s^d, γ_s^p, and γ_s^h were then obtained by regression of the data using the equation

$$\gamma_l(1+\cos\theta') = 2[\sqrt{\gamma_s^d \gamma_l^d} + \sqrt{\gamma_s^p \gamma_l^p} + \sqrt{\gamma_s^h \gamma_l^h}] \qquad \textbf{Equation 2-3}$$

A similar procedure applies in determining the surface energy components of a crystal face. The surface energy components of the nucleus were approximated with those of the macroscopic crystal face which preferentially nucleates on the polymer surface, i.e., the (100) and (011) faces according to previous crystal orientation studies. The contact angles of (100) and (011) faces with the probing liquids were taken from Heng, et al.[75] The surface energy components of the solvent were determined from its contact angles with eight probing surfaces. Figure 2-14 summarizes the surface energy components of polymer surfaces, clearly showing that polymer AM has the most polar surface, followed by CEA and HBA, while STY is essentially non-polar.

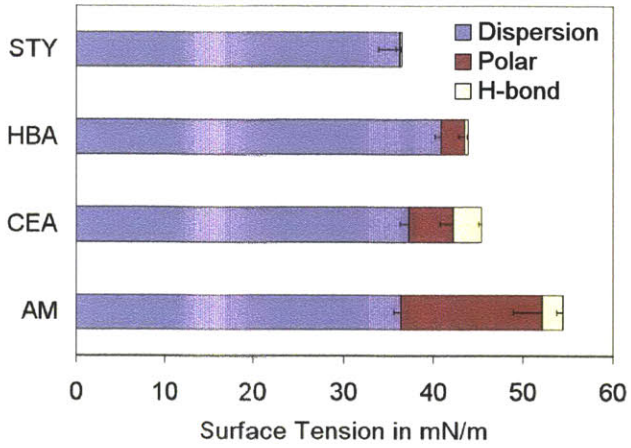

Figure 2-14. Polymer surface energy components. The advancing contact angle between a polymer and a probing liquid was measured at least six times for each of the five probing liquids applied on each polymer.

The CNT contact angle θ was calculated from the surface energy components of the polymer substrate, the crystal facet and the solvent. The relative API nucleation activity of polymer substrates predicted by θ matches well with that quantified by τ (Table 2-4). In particular, a CNT contact angle of 180° indicated that HBA and STY surfaces are non-wetting for the nucleus of aspirin, and correspondingly, induction time experiments showed that HBA and STY were not able to induce aspirin nucleation. Though AM and CEA were able to enhance nucleation of aspirin, the wetting conditions are not ideal given the fairly large CNT contact angles, which leaves room for further improvement in their surface nucleation activities by varying the solvent

or modifying the surface morphology. To derive surface design principles, it is necessary to understand what surface chemistry leads to a low CNT contact angle with a given compound. Since the polymer substrates investigated preferentially nucleate polar facets of aspirin, the polarity of a polymeric substrate was quantified by γ_p, the polar component of surface energy, and % HSA, the percentage of hydrophilic surface area of the monomer (Table 2-4). As expected, the surface polarity correlates qualitatively with the API nucleation activity of the substrate for the system under investigation. If further verified, %HSA could provide direct guidance to surface design for controlling nucleation.

Polymer samples	AM	CEA	HBA	STY
τ (h) –nonporous	38.1±0.3	113±3	210±30*	242±5*
θ (°) –nonporous	110.7	140.4	180	180
γ_p (mN/m)	15.7±3.2	5.0±1.5	2.6±0.7	0.7±0.5
% Hydrophilic surface area	78.7	70.4	58.5	0

Table 2-4. Qualitative correlations of the average nucleation induction time with the CNT contact angle (θ), polar component of polymer surface energy (γ_p) and percentage hydrophilic surface area (%HSA) of the monomer used in synthesizing polymers. %HSA was calculated with Molecular Modeling Pro by means of atomic contributions. *Aspirin nucleation rates with HBA and STY were not statistically different from the bulk case.

2.4. Conclusions

To enable rational design of surfaces for controlling nucleation, the effect of surface chemistry on the API nucleation activity of polymer substrates was investigated systematically and quantified in terms of the nucleation kinetics of aspirin. Of the variety of functional polymers explored, poly(4-acryloylmorpholine) and poly(2-carboxyethyl acrylate), each crosslinked by divinylbenzene significantly enhanced aspirin nucleation kinetics, while other less polar polymers such as polystyrene and poly(4-hydroxybutyl acrylate) remained ineffective. A model based on the interfacial free energies was developed and successfully predicted the relative API

nucleation activity of non-porous polymer surfaces. The model indicates that it is through interfacial free energies that the surface chemistry influences the surface nucleation activity. Further analysis of polymer surface energy components helped to reveal the importance of surface polarity to the API nucleation activity of the polymer surfaces provided that the crystal facets preferentially nucleated are polar. To probe molecular level interactions, I studied the preferred orientation of aspirin crystals on polymer films and found that the hydrogen bond donor-acceptor relationship may play an important role in steering the crystal orientation. Specifically, the aspirin (011) face rich in carboxyl groups prefers to interact with the tertiary amide functionality on the surface of poly(4-acryloylmorpholine), while the (100) face dominated by carbonyl groups grows on poly(2-carboxyethyl acrylate) surfaces abundant in carboxyl groups. These findings underpinned the significance of surface chemistry to nucleation kinetics and the final crystal form, which has not been studied systematically in pharmaceutical systems as far as we know. I also demonstrated nucleation induction time statistics as a powerful tool for probing the mechanism of heterogeneous nucleation on controlled surfaces. With the aid of this tool, I successfully separated and quantified the effects of surface morphology and surface chemistry on the API nucleation activity of a polymer surface and found that the presence of nanoscopic pores can greatly enhance the nucleation activity of a polymer surface. Poly(4-acryloylmorpholine) and poly(4-hydroxylbuyl acrylate) with pores around 100nm and 50nm respectively, nucleated aspirin orders of magnitude faster than did the non-porous polymers. However, comprehensive investigations are needed to understand the effect of surface pore structures on nucleation kinetics and the final crystal form, which are discussed in Chapter 3.

Chapter 3

3. Role of Nanopore Shape in Surface-Induced Nucleation

3.1. Introduction

It is well recognized that surfaces play a crucial role in liquid-solid phase transformations, and surface morphology has been shown to impact nucleation and crystallization significantly.[1,49,77] Roughening of the surface in a crystallization system leads to accelerated nucleation, and in industrial practice, surface scratching has long been used to promote nucleation.[48] However, without knowledge of the geometrical features of the surface cavities at a microscopic scale relevant to nucleation, the surface roughness alone, as a macroscopic parameter, may be insufficient, and even misleading, to describe the effect of surface morphology on nucleation. Recently, there has been an increase in the number of studies on crystal nucleation in sub-100 nm pores, which were demonstrated to affect nucleation kinetics,[68] polymorphism[54] and crystal orientation.[78] These studies focused mainly on the effect of pore size in the context of nanoscopic confinement, but the role of pore shape has been neglected. The lack of systematic investigation on the effect of pore shape is due, in no small part, to the challenges in making macroscopic material with nanopores of tunable geometry, particularly with pores under 100nm in size.

In Chapter 2, the dramatic effect of surface nanopores (50-100 nm) on nucleation was demonstrated and it was hypothesized that the pore geometry plays a key role in determining the kinetics of nucleation from solution. In this chapter, I present the first experimental evidence to support this hypothesis. The importance of favorable surface chemistry in mediating the observed 'pore shape effect' is also demonstrated. Angle-directed nucleation is proposed as a

possible mechanism for interpretation of the 'pore shape effect' on nucleation of a model compound, and a molecular mechanism is put forward.

3.2. Experimental Methods

3.2.1. Fabrication of Polymer Films with Spherical Nanopores

Quartz slides (75mm x 25mm) were treated with O_2 plasma to enrich the surface in hydroxyl groups. Two hundred microliters of 5w% colloidal silica (commercially available) were spread on the quartz slide and allowed to self-assemble during slow water evaporation over 12 hours. The self-assembled SiO_2 and the quartz slide were then sintered at 800°C for 5min to coalesce the particles with the quartz slide and form the imprint mold. The film substrate (25mm x 5mm) was prepared by treating a glass slide with O_2 plasma followed by silanization with trichlorosilane in a vacuum oven at 40°C. Silanization is necessary to 'glue' the polymer film to the substrate via covalent bond and thereby avoid film cracking and peeling off from the substrates. One microliter prepolymer mixture of monomer acrylic acid (AA), crosslinker divinylbenzene (DVB), and initiator IRGACURE 2022 were sandwiched between the imprint mold and the film substrate. The molar ratio of monomer to DVB was 2:1. The concentration of IRGACURE 2022 was 4 v% with respect to DVB. The prepolymer mixture was then polymerized under UV irradiation for 15min, at 72mW/cm^2. After irradiation, the imprint mold was peeled off and the polymer films were annealed at 70°C in a vacuum oven for 3h to remove unreacted species. Whenever possible, parts were pre-cleaned and assembled in a Bio-safety cabinet to reduce contamination by impurities, which can interfere with polymer film induced nucleation.

3.2.2. Fabrication of Polymer Films with Angular Nanopores

3.2.2.1 Synthesis of Faceted Fe_3O_4 Nanoparticles

Materials. Iron tri(acetylacetonate) (Fe(acac)3) (97 %), 1,2-tetradecanediol (90 %), oleic acid (OA) (90 %), and benzyl ether (99 %) were purchased from Sigma Aldrich. n-Decane (99 %) was purchased from Alfa Aesar. Methanol (99.8 %) was purchased from Mallinckrodt. All chemicals were used as received. All water utilized in the experiments was Milli-Q (Millipore) deionized water.

Synthesis method. Colloidal dispersions of faceted Fe_3O_4 nanoparticles was prepared by a slightly modified procedure of the method for the synthesis of spherical Fe_3O_4 nanoparticles reported previously.[79] In brief, iron tri(acetylacetonate) (2 mmol), 1,2-tetradecanediol (10 mmol), oleic acid (12 mmol), and benzyl ether (20 mL) were mixed and stirred magnetically under flowing nitrogen. The mixture was heated gradually to 200 °C and kept at this temperature for 2 h. Then, the temperature was increased up to the reflux condition (300 °C) under a blanket of nitrogen, and kept for 1 h at reflux. The black reacted liquid was cooled to room temperature by air-cooling and transferred from the reaction flask to a centrifugation bottle. On addition of methanol (40 mL) to the reaction mixture, the black nanoparticles precipitated and were separated via centrifugation (9000 rpm, 10 min). To remove the residual reacting materials, the precipitated nanoparticles were rinsed with methanol several times. After the precipitated nanoparticles were well-dried, 10 mL of n-decane was added to the precipitate and the mixtures were ultrasonicated.

3.2.2.2 Polymer Films Synthesis and Imprinting

Polymer films with hexagonal nanopores were synthesized following a procedure similar to that described above, templated with iron oxide magnetic nanoparticles (MNP). The presence of

sufficient surfactants (oleic acid) during synthesis was important for obtaining sharply defined facets of MNP crystals. As in the case of making spherical nanopores, colloidal self-assembly was utilized for preparing the imprint mold, which was made by spreading 20μl MNP-decane solution (~9 w%) on a plasma cleaned quartz slide (75mm x 25mm) and allowing the decane to evaporate over a period of 6 hours. The excessive surfactants present in the nanocrystal dispersion also participated in the assembly process leaving space for polymers to form between the nanocrystals. After polymerization, the imprint mold was peeled off from the polymer film, the nanocrystals on the film were subsequently dissolved with dilute hydrocholoric acid (~1N), and the film was rinsed with deionized water followed by acetone and vacuum dried. The imprint mold for making square pores was fabricated by Achromatic Interference Lithography[21] at the MIT Research Laboratory of Electronics. The mold took the form of 120nm Si square pillar arrays with 200nm pitches covering a 3-inch Si wafer. The top edges of the pillars were sharply defined with radii of curvature less than 5nm. Large area patterning is necessary for making sufficient copies of polymer films to obtain the induction time probability distribution. The polymer film synthesis and post-processing procedures were the same as those used in the preparation of spherical nanopores. The effects of polymer films with pores on nucleation kinetics were compared against those in the absence of pores, which were synthesized following the same procedure with the quartz surface as the template.

3.2.3. Nucleation Induction Time Measurement

Once synthesized, the polymer film with its substrate was inserted vertically into a 1ml glass shell vial containing 200μl 47mg/ml aspirin solution in butyl acetate. For each polymer sample, 20-50 vials were assembled and immersed in a circulator stabilized at 50±0.1°C to dissolve any pre-existing crystals, and then the solution was quench cooled to 5±0.1°C by immersing into a

second circulator. The supersaturation at the start of each experiment was 2.2, which is defined as the ratio of starting concentration to the equilibrium concentration at the crystallization temperature. The number of vials in which crystallization occurred was recorded as a function of time. All the operations involving exposing polymer films, aspirin solutions and shell vials to the atmosphere were conducted inside a Bio Safety Cabinet to reduce impurity contamination to the lowest possible level. Efforts were made to clean all components before usage and aspirin solutions were filtered with an Acrodisc 0.2μm PTFE syringe filter.

3.2.4. Polymer Chemistry Screening

Polymers with smooth surfaces were synthesized directly in the glass shell vials used for crystallization, instead of on a glass substrate as in the case of polymer films with nanopores. In this way, the impurities and active nucleation sites from the glass substrates were eliminated, hence the real extent of nucleation acceleration induced by the polymer surface could be measured.

30μl prepolymer mixture of monomer, crosslinker divinylbenzene (DVB), initiator IRGACURE 2022 were injected into the 1ml pre-cleaned glass shell vials under the Bio-Safety Cabinet. The monomers tested were 4-acryloylmorpholine (AM), 4-Hydroxybutyl acrylate (HBA), and acrylic acid (AA). The molar ratio of monomer to DVB was 2:1. The concentration of IRGACURE 2022 was 4 v% with respect to DVB. The prepolymer mixture was subsequently polymerized under UV irradiation under N_2 protection for 30min, at ~10 mW/cm^2. Less UV intensity and longer irradiation time were applied to avoid polymer cracking during rapid polymerization. After polymerization, the polymers and the shell vials were allowed to slowly cooled down for 30min before annealed at 70°C in a vacuum oven for 5h to remove unreacted species.

The nucleation induction time study followed the same procedure as described in 3.2.3. It is worth noting that to the bottom of the vials were attached 3/8-inch thick rubbers to block heat transfer from the bottom of the vials. This was necessary because the polymers conformed to the bottom of the vials differed in heat conductivity, resulting in different cooling rates in the solution if the heat transfer were allowed through the bottom of the vial; and the cooling rate significantly impacted the nucleation induction time. In addition, enough vial spacing was designed to allow equivalent cooling rate around each vial.

3.2.5. Characterization

Atomic Force Microscopy (AFM) and Powder X-ray Diffraction (XRD) were employed to study the aspirin crystal orientation inside the angular nanopores on the polymer films after the nucleation induction time study. AFM images were obtained with a Dimension 3100 XY closed loop scanner (Nanoscope IV, VEECO) equipped with NanoMan software. Height and phase images were obtained in tapping mode in ambient air with silicon tips (VEECO). The crystal orientation was verified with XRD to identify the specific crystallographic planes parallel to the polymer film. The X-ray diffraction patterns were recorded with a PANalytical X'Pert PRO Theta/Theta Powder X-Ray Diffraction System with Cu tube and X'Celerator high-speed detector. No less than five polymer films were examined with XRD on each type of polymer sample.

3.3. Results and Discussion

3.3.1. Polymer Films with Spherical and Angular Nanopores

We are interested in comparing the effects of angular pores to those of spherical pores of similar size. For this purpose, a fabrication technique is required to control both the surface pore geometry and the pore size down to length scales relevant to nucleation, especially, to enable

surface patterning with pores from a few to hundreds of nanometers. Nanoscopic pores with high area density are preferred, providing a sufficient number of pores to ensure statistical significance of the observed effects on nucleation. Sub-10 nm pores are avoided because reported volume confinement effects on nucleation[69,70,80] may mask the effects of pore shape. In addition, the resolution requirement for the fabrication technique is set by the length scale of molecular events preceding nucleation, namely the molecular clustering and re-orientation that occur in domains of, probably, a few nanometers for small organic molecules. To meet these requirements, we developed 'Nanoparticle Imprint Lithography' (NpIL) drawing inspiration from Nanoimprint Lithography (NIL)[81] and Nanosphere Lithography (NSL).[82] NpIL can be used to fabricate nanopatterned polymer surfaces with nanopore arrays of various shapes ranging from ten to hundreds of nanometers, using nanoparticle assemblies as templates.

The fabrication of polymer films with spherical nanopores by NpIL is illustrated in Figure 3-1. First, spherical silica nanoparticles were self-assembled on a quartz slide driven by capillary forces during water evaporation,[82] and then anchored to the substrate via calcination to form the imprint mold (Figure 3-1a). Second, a mixture of monomer, crosslinker and initiator was sandwiched between the imprint mold and the substrate, and subsequently polymerized under UV irradiation. The imprint mold was then easily peeled off to reveal a polymer film conforming to the substrate, with the nanopattern inversely transferred from the imprint mold (Figure 3-1b). Polymer films with spherical nanopores ranging from 15 nm to 300 nm were fabricated in this manner (Figure 3-1c), templated by commercially available monodispersed colloidal silica of various sizes. This method combines many of the advantages of NSL and ultraviolet-assisted NIL, such as low cost, high throughput,[83] and high-resolution.[81] Moreover, in contrast to the commonly practiced NSL technique, where hydrofluoric acid is needed to dissolve the silica

nanoparticles,[82] our method removes the template nondestructively by a simple liftoff from the polymer film, allowing the mask to be recovered easily and reused.

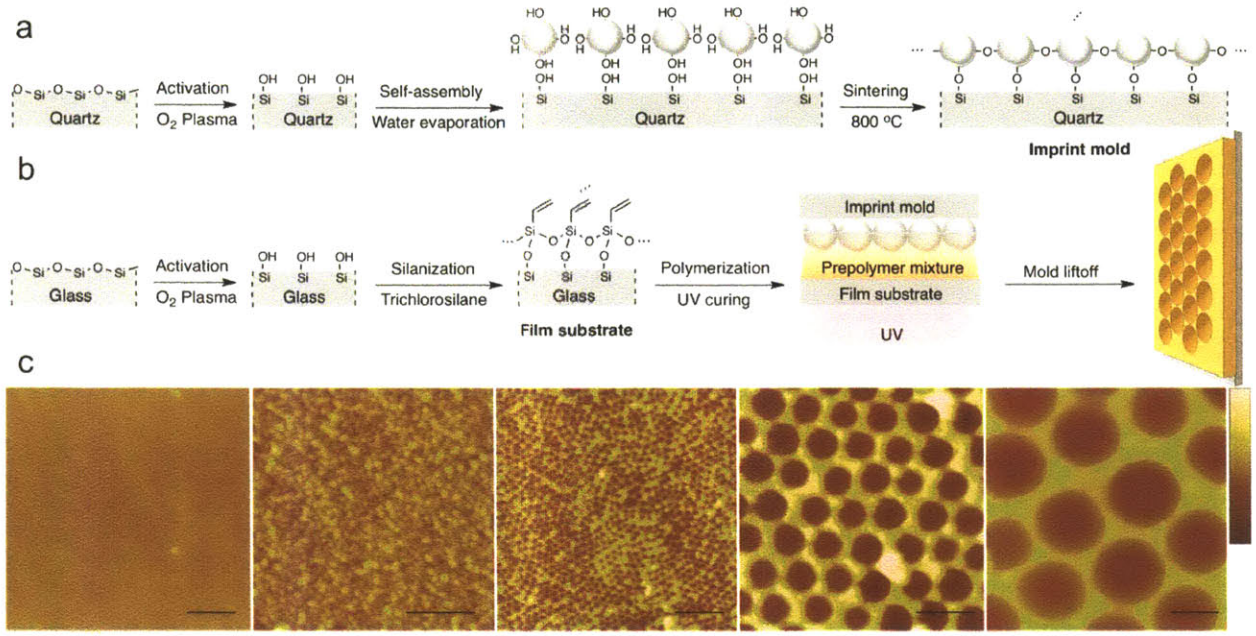

Figure 3-1. Fabrication of polymer films with spherical nanopores by NpIL. (a) Template preparation via colloidal silica self-assembly and its anchoring to the quartz substrate. (b) Film substrate preparation and polymer film synthesis by UV polymerization. (c) AFM height images of polyacrylic acid films crosslinked with divinylbenzene (AA-co-DVB) with and without spherical nanopores templated with colloidal silica of various sizes. The average pore size is (from left to right) none, 15 nm, 40 nm, 120 nm, and 300 nm. The scale bar is 200 nm. The data scale in height is (from left to right) 50 nm, 50 nm, 50 nm, 100 nm, and 400 nm.

Polymer films with hexagonal pores (Figure 3-2a) were also prepared by NpIL following a similar procedure (see 'Methods' section), templated with iron oxide magnetic nanocrystals with well-defined facets (Figure 3-2b). For making square nanopores (Figure 3-2c), square-shaped nanoposts (Figure 3-2d) were fabricated by Achromatic Interference Lithography (AIL)[84] as the imprint mold. The imprinted square pores are comparable to the spherical ones in width and depth (Figure 3-2e), with sharply delineated pore angles (radius of curvature < 3 nm, Figure 3-3). In addition, the nanopatterning procedures employed in this study preserved the molecular level surface roughness with respect to the nonporous polymer surface (Table 3-1), which enables unambiguous differentiation of the effects of pore shape on crystal nucleation.

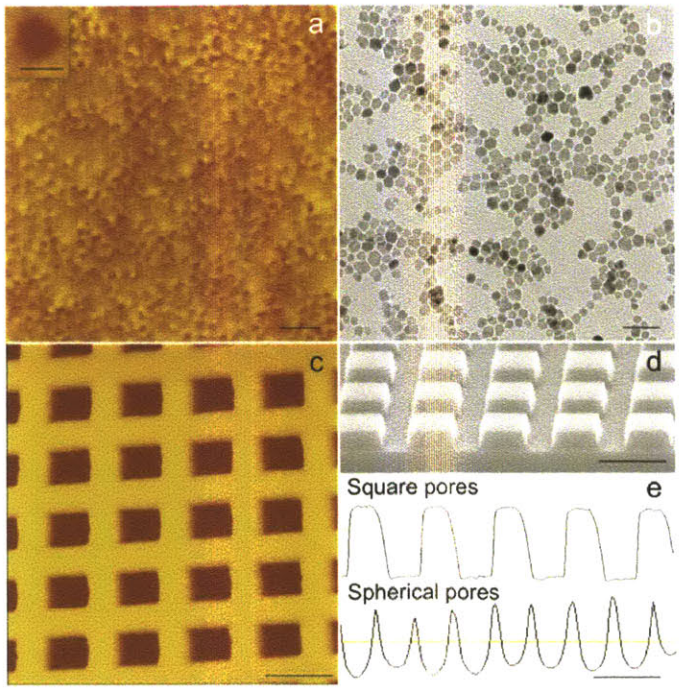

Figure 3-2. Angular nanopores on AA-co-DVB polymer films and their templates. (a) AFM height image of hexagonal nanopores on the polymer surface templated with iron oxide magnetic nanocrystals via NpIL. The scale bar is 50nm. (Inset) Higher resolution image of a hexagonal nanopore. The scale bar is 10nm. (b) TEM image of iron oxide magnetic nanocrystals as synthesized. The scale bar is 50nm. (c) AFM height image of square nanopores on the polymer surface templated with Si square posts. The scale bar is 200nm. (d) High resolution SEM image of Si square posts on Si wafer fabricated by AIL for templating square pores. The scale bar is 200nm. (e) Depth profiles of square and spherical nanopores of similar sizes. The scale bar is 200nm. The square pores are 125nm in width, 48nm in depth, and the spherical pores are 120nm wide, 45nm deep on average.

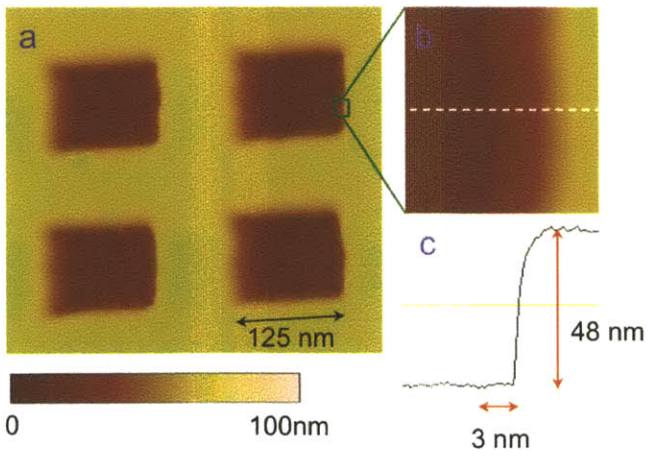

Figure 3-3. Radius of curvature at the angle of square pores characterized via AFM. (a) AFM height image of AA-co-DVB polymer surface. (b, c) High-resolution AFM height image and its corresponding depth profile. High-resolution solid carbon cone tip AFM probe was utilized for the high-resolution imaging, with a tip spike > 300 nm, and tip radius < 3 nm.

Table 3-1. Molecular level surface roughness of nanopatterned polymer films characterized by AFM.

Pore shape	Nonporous	Spherical	Square	Hexagonal

RMS surface roughness (nm)	0.39±0.02	0.42±0.02[a]	0.36±0.04[b]	0.34±0.02[c]

a, AFM scans were performed inside the 40nm and 120nm spherical pore. Plane fit routine was carried out to project the spherical surface to a 2D plane. RMS surface roughness was calculated from the height profile inside the pore.

b. Surface roughness inside the pore was the same as that on the flat region between the pores. The average value is reported here.

c. Given the small pore size and dense packing of pores on the surface, it was difficult to obtain the surface roughness either inside the pore or in-between the pores. Instead, nonporous control surfaces were prepared following the same fabrication procedure, but without the addition of nanocrystals as porogen. The surface roughness of control surfaces is reported here.

3.3.2. Effect of Nanopore Shape on Nucleation Kinetics

The effect of nanopatterned polymer films on the kinetics of nucleation from solution was quantified by the nucleation induction time of aspirin, a representative compound for small organic molecules. The relative extent of reduction in the nucleation induction time serves as a measure of the effectiveness of polymer films in promoting nucleation. The polymer film was made from acrylic acid crosslinked with divinylbenzene (AA-co-DVB), with which aspirin could interact via hydrogen bonding. Polymer crosslinking was designed to avoid solvent uptake and to maintain the surface morphology when in contact with the solution. Due to the stochastic nature of nucleation events, 20 to 50 samples were tested simultaneously to obtain the probability distribution for the nucleation induction time. The average induction time, τ, was determined from a statistical analysis on the induction time data based on the knowledge that nucleation follows a Poisson distribution, $P(t)=\exp(-t/\tau)$,[77,80] where P is the probability that no nucleation event occurs within time t.

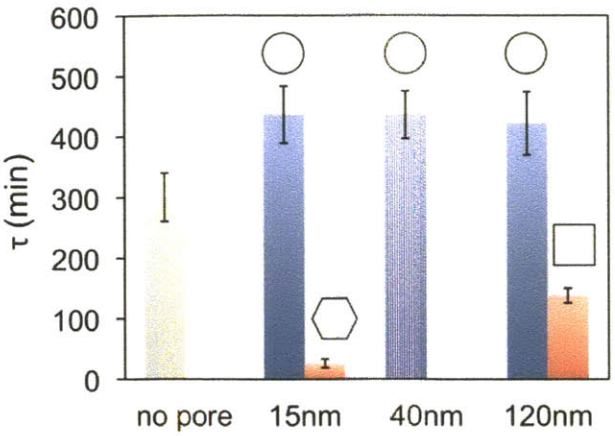

Figure 3-4. Effect of the nanopore shape in AA-co-DVB polymer films on the nucleation kinetics of aspirin: spherical pores vs. hexagonal pores and square pores of the same size. Nanopatterned surfaces are compared against flat and smooth surfaces without pores, labeled as 'no pore'. τ is the average nucleation induction time. The standard errors of τ were calculated from the regression on the induction time probability distribution following the Poisson distribution.

As shown in Figure 3-4, increasing the surface roughness by modifying the nonporous film with spherical nanopores surprisingly inhibited nucleation, as evidence by the lengthened nucleation induction times. The size of the spherical nanopores appeared to have little effect on the nucleation kinetics, within the range tested, but nucleation was promoted when angular pores of the same size were used, as shown in two cases. With hexagonal pores, the polymer film reduced aspirin nucleation induction times by more than an order of magnitude relative to those observed with spherical pores, while in the case of square pores, a three-fold reduction was observed. These results indicate that the angles that distinguish faceted from spherical pores acted as nucleation sites, which has been verified via Atomic Force Microscopy (AFM) and X-ray Diffraction (XRD), as discussed later. Our observations can be interpreted in terms of recent computational results. Cacciuto and coworkers[49] used Monte Carlo simulations to show that freezing of hard sphere colloids is frustrated on curved surfaces, on which crystals cannot grow free of strain, and that the resulting defects increased the barrier to nucleation. Page and Sear found by Monte Carlo simulation of Lennard-Jones molecules that nucleation in wedges is many orders of magnitude faster than on a flat surface and that there exists an optimum wedge angle at

which nucleation is the fastest.[48] This optimum wedge angle corresponds to an intrinsic angle within the crystal, formed by two close-packed planes, at which the crystal can grow defect-free along both sides of the wedge.

3.3.3. Angle-Directed Nucleation

'Angle-directed nucleation' is a possible mechanism in our case, where an angle characteristic of the topological feature on the substrate directs the crystal nucleation in a minimum-strain configuration, exhibited as a geometrical match between the substrate and the crystal. The aspirin crystal possesses intrinsic angles formed by close-packed, low-index facets close to the characteristic angles in the nanopores tested (Figure 3-5c, d, f). In the square nanopore, the angle at the intersection of the pore wall and the pore floor (L_{wf}, its dihedral angle abbreviated as α) could induce the growth of either (011) and (100), or (002) and (100) facets of aspirin ((011)$\wedge$(100) or (002)$\wedge$(100), with dihedral angles abbreviated as $\theta_{011\wedge100}$ and $\theta_{002\wedge100}$, respectively) (Figure 3-5c, d), where (100), (011) and (002) are the three major facets of aspirin crystallized from bulk solution. To estimate the extent of angular match, the cross-section of the square nanopore was examined via High Resolution Scanning Electron Microscopy (HRSEM), and α was measured to be 96 ± 7° in one corner of the cross-section and 101 ± 5° in the other. This asymmetry was consistent through the cross-section for all pores observed, which may have arisen from the asymmetric stress applied to the polymer film during the template liftoff. Both $\theta_{011\wedge100}$ and $\theta_{002\wedge100}$ fall in the vicinity of the smaller α, 96 ± 7°, with $\theta_{002\wedge100}$ being the closer match ($\theta_{002\wedge100}$= 95.84°, $\theta_{002\wedge100}$ = 92.94°). Specifically, about 30% of pores contained an angle α of within 1° of $\theta_{002\wedge100}$, and around 8% within 1° of $\theta_{002\wedge100}$.

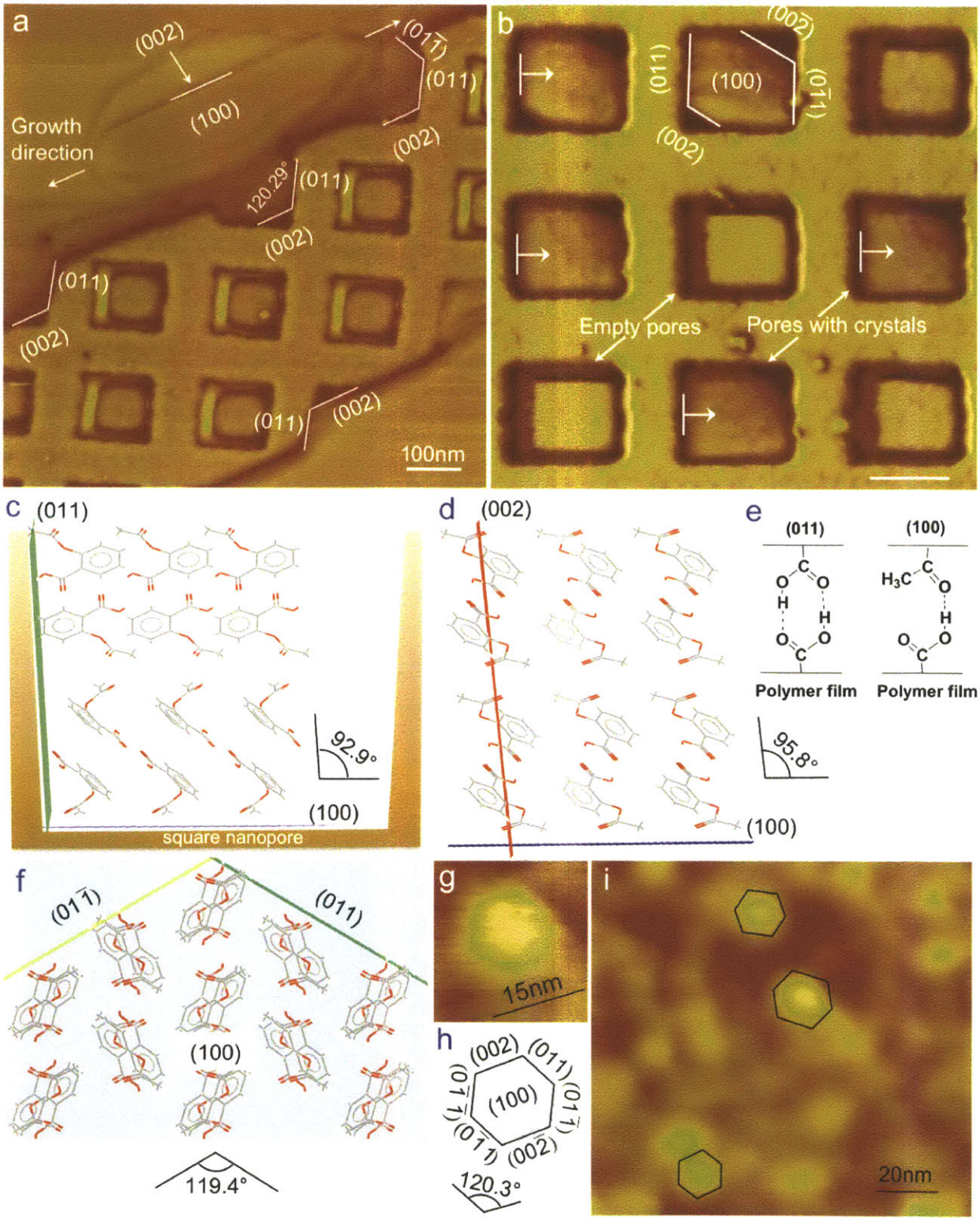

Figure 3-5. Angle-directed nucleation of aspirin crystals induced by angular nanopores. (a) AFM phase image of aspirin crystals grown out from the square pores. (b) AFM phase image showing (100) layers of aspirin crystals nucleated at ledges in the square pores, indicated with white lines for all pores containing crystals. The scale bar is 100nm. (c, d) Possible configurations of aspirin crystal facets in the square pore,

whose cross-section is depicted. (e) Proposed aspirin-polymer interactions at the crystal-polymer interface. (f) Proposed configuration of aspirin crystal facets at the corner of an hexagonal pore. (g, h) AFM phase image of an aspirin crystallite grown from the 15nm hexagonal pores and its possible orientation. (i) AFM height image of the surface of an aspirin crystal grown on and detached from the AA-co-DVB polymer film with hexagonal pores. The contours of the crystallites are traced at a small distance from the crystal edges so as not to obscure them.

If angle-matching were the only factor dictating nanopore-induced nucleation, (002)∧(100) would be nucleated preferentially from L_{wf} within the pore. The AFM images of aspirin crystals grown from the pores suggest it was the (011)∧(100) facets that emanated from L_{wf}, whereas the (002) facet was not in contact with the pore surface (Figure 3-5a, b). The crystal facets were assigned based on the following observations. First, layered growth of aspirin parallel to the pore floor is evident in both the crystal grown out from the pore (Figure 3-5a) and the crystals contained in the pore (Figure 3-5b), which originates from the aspirin dimerization via the carboxyl group within the (100) layer, and a much weaker van der Waals interaction between the layers. It is these layers that constitute the aspirin (100) plane, which was confirmed by XRD that the (100) plane grew parallel to the film surface (Figure 3-6). Second, the terrace formed by the edges of developing layers points towards the crystal growth direction (Figure 3-5a), which is along the (010) axis, and the slow growing face (002) is left to define the crystal edges.[85,86] This assignment is in agreement with the dihedral angles exhibited by the crystals in the pore (Figure 3-5a,b).

Figure 3-5b shows that these (100) crystal layers seem to extend from the pore wall with which the (011) face is in contact. Moreover, the layer extension direction as denoted with white arrows is consistent in all pores containing crystals, indicating nucleation occurs predominantly from one side of the pore. In addition, only a fraction of the pores induced nucleation. These observations provide evidence that the (011)∧(100) and not (002)∧(100) facets were nucleated from L_{wf}, but only from those with the appropriate angle α. These growth patterns can be

attributed to the favorable interactions between (011)∧(100) and the polymer surface, as inferred from the characteristic functionalities displayed on their respective surfaces (Figure 3-5c-e). (011) and (100), rich in carboxyl and carbonyl groups, can form hydrogen bonds with the carboxyl groups on the AA-co-DVB polymer surface, whereas the nonpolar (002) plane is likely to interact with the polymer much more weakly. This result suggests that solute-polymer interactions play an important role in determining nucleation behavior in angular pores, and not just the geometrical match.

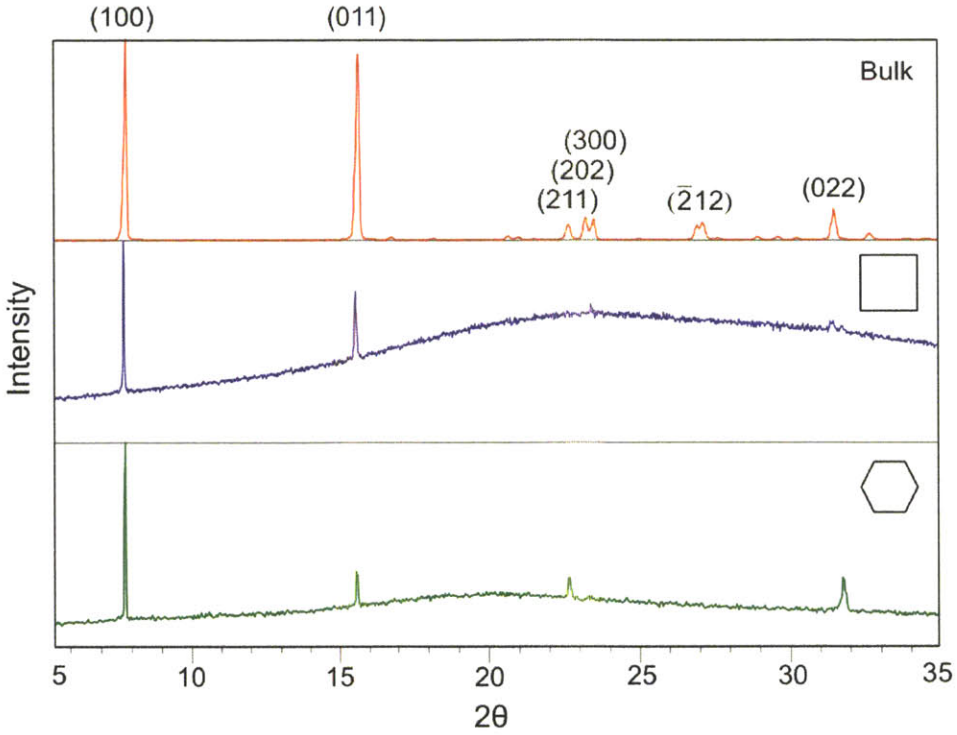

Figure 3-6. X-ray diffraction pattern of aspirin crystals grown from the butyl acetate bulk solution (top), on AA-co-DVB films with 125nm square nanopores (middle), and on AA-co-DVB films with 15nm hexagonal nanopores (bottom).

Directed by both favorable interactions and angular match, the single crystals in square nanopores exhibited a high degree of alignment, providing further evidence for nucleation at pore angles. Shown in Figure 3-7a, the ASA crystal nucleated from a square nanopore as a single crystal with well defined (002)/(00$\bar{2}$) and (011)/(0$\bar{1}$1) facets, delineated with white lines.

Compared with the bulk crystal habits (Figure 3-7b), crystals from the nanopores did not show clearly defined $(01\bar{1})$ crystal facet possibly due to the rapid crystal growth in the (010) direction until the growth front meets the corresponding pore corners, which results in the elimination of the $(01\bar{1})$ crystal facet. It is particularly interesting that all single crystals in the pores seem to align with respect to each other, evidenced by the parallel $(002)/(00\bar{2})$ facets which are free-standing and not confined by the pore wall. Besides, the (100) layer extension direction is also the same for all crystals in the pores (Figure 3-5b), which confirmed the observed alignment effect.

To quantitatively measure the degree of in-plane alignment of crystals in the pores, we represent the ASA crystal orientation with the orientation of the fastest growing axis, (010), indicated as the blue dotted line shown in Figure 3-7b. Since the ASA crystal structure is centrosymmetric, it is not necessary to specify the direction of the axis. In the square nanopores, the relative crystal orientation can be quantified by the angle α between the (010) axis and the pore sidewall in contact with the (011) facet (Figure 3-7c). Since the (002) facet is parallel to the (010) axis, α is also equal to the acute angle formed by the (002) facet and the pore sidewall indicated by the red dotted line. To verify the generality of the observed alignment effect, we measured α for 33 crystals in the square pores from 8 independent polymer films to obtain the distribution of α. The result is shown in Figure 3-8. Close to 80% of measurements fell between 55° and 65°. The mean of α is 59.2°, which is very close to the intrinsic angle between the (010) axis and the (011) facet, 59.7°, and the standard deviation is 4°. Such a narrow distribution of α provided strong evidence of nucleation affected by the pore angles.

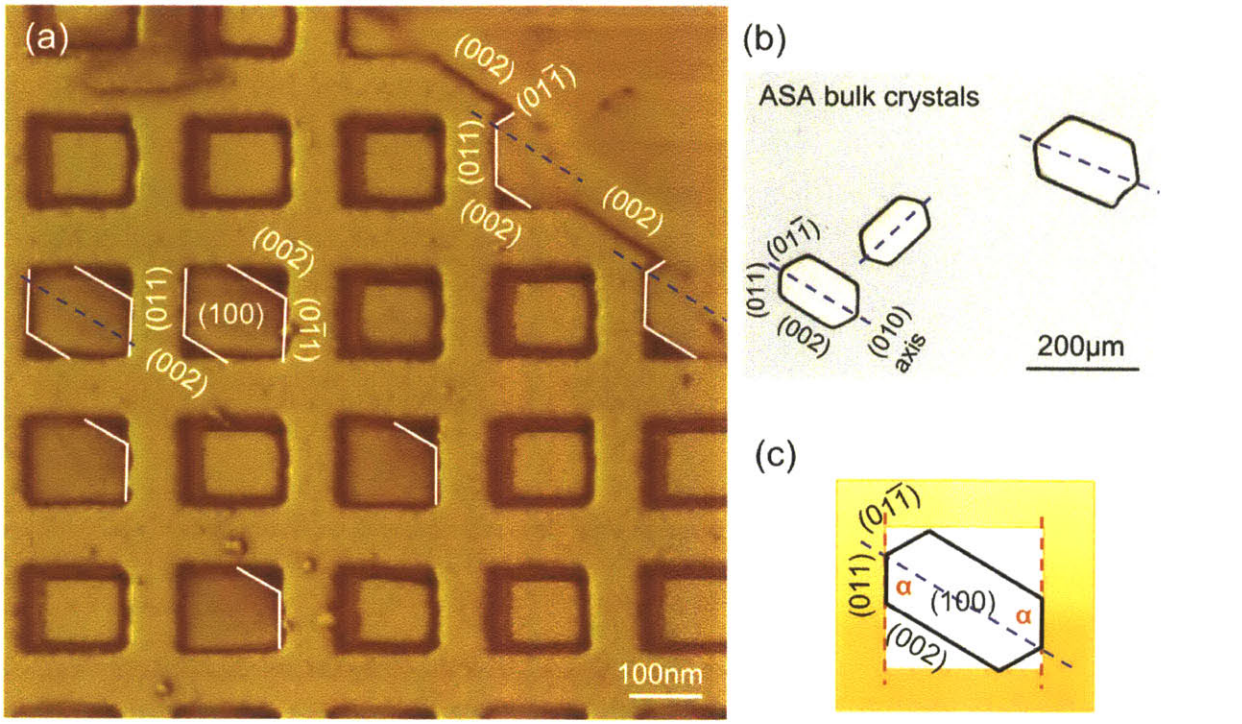

Figure 3-7. Alignment of ASA crystals in square nanopores. a) AFM phase image of ASA crystals inside the square pores and those grown out from the pores (upper right corner). All ASA crystals nucleated from the pores are delineated with while lines at least partially, and those pores without labels are empty confirmed with the corresponding height image. b) Optical micrograph of ASA bulk crystals. The blue dotted line denotes the (010) axis, which represents the orientation of a crystal. c) Schematic illustrating the orientation of an ASA single crystal inside a square nanopore. *α* is the acute angle between the blue dotted line and sidewalls of the nanopore indicated by the red dotted line.

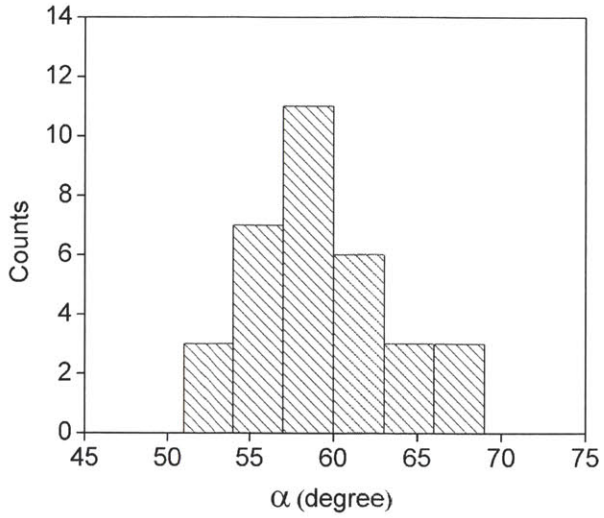

Figure 3-8. Histogram of ASA crystal orientation (quantified by *α*) distribution in square nanopores. *α* is defined in Figure S4. The mean of *α* is 59.2° and its standard deviation is 4°.

Following the principle of angle-directed nucleation assisted by favorable interactions of the crystal facets with the substrates, we propose that the corners within hexagonal pores acted as

nucleation sites to induce the growth of $(011)\wedge(01\bar{1})\wedge(100)$ with (100) in contact with the pore floor, and $(011)\wedge(01\bar{1})$ with the pore walls (Figure 3-5f). This is plausible because the angle mismatch is very small in this configuration, and all three faces of aspirin could interact with the polymer surface via hydrogen bonding. If nucleation ensued from the corner, the growth thereafter would have resulted in an aspirin crystallite that fit comfortably inside the pore and took on the shape of a hexagon, given that other intrinsic angles of the crystal also matched quite well with the pore geometry (Figure 3-5h). Indeed, crystallites with comparable shape and size to those of the pore were observed via AFM on the surface of aspirin crystals detached from the polymer film (Figure 3-5g, i). In addition, XRD results verified that the (100) face was in contact with the pore floor (Figure 3-6). Moreover, in-plane alignment of hexaganol crystallites was also evident in local domains (Figure 3-9). These observations support our hypothesis of corner-induced nucleation from hexagonal pores.

In-plane alignment of crystals is observed only locally instead of globally due to the lack of long-range order of the hexagonal nanopores on the polymer film. In other words, the hexagonal nanocrystals self-assembled on the imprint mold arrange in poly-crystalline domains of several hundred nanometers, and each domain exhibits a different overall orientation, instead of a single crystalline superlattice. This phenomenon is commonly observed with self-assemblies of nanoparticles on solid substrates. The poly-crystalline nature of the imprint mold then transfers into the short-range ordering of the hexagonal nanopores via the imprinting step. Shown in Figure 3-9, where crystallites delineated with the same color exhibit similar orientation and are possibly nucleated from the same domain on the polymer film.

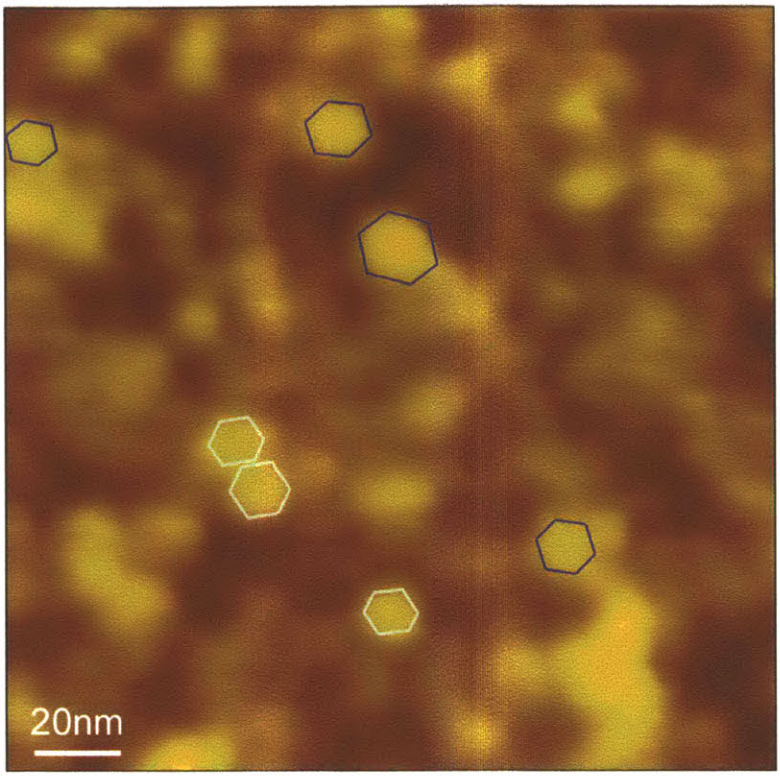

Figure 3-9. Alignment of ASA crystallites nucleated from hexagonal nanopores. AFM height image of the surface of an aspirin crystal grown on and detached from the AA-co-DVB polymer film with hexagonal pores. The contours of the crystallites are traced at a small distance from the crystal edges so as not to obscure them. Crystallites exhibiting the 'same' orientation are delineated with the same color. The orientation is considered the same when the contours of the two crystallites can overlay with each other just by re-scaling without re-orienting.

3.4. Molecular Mechanism

Based on the experimental and computational evidence, we propose a molecular mechanism to interpret the pore shape effect on nucleation. Crystal nucleation from solution is preceded by molecular cluster formation via density fluctuations and molecular re-orientation through structure fluctuations; both are necessary for nucleation.[16] The rate of nucleation can be modified in two ways by the presence of an amorphous, nanoporous surface in a metastable solution. First, favorable surface-solute interactions enrich solute concentrations near the surface, and molecular recognition events between the surface and the solute induce partial orientational order within the enriched solute layers; both effects could facilitate nucleus formation.[46,77] Second, angles in the pore further enhance the orientational order of the solute in domains close to the surface via

geometrical confinement, which promotes the solute molecular realignment. When the molecular orientation imposed by the angle geometry resembles that in the crystal, the rate of nucleation is increased to the greatest extent, the macroscopic expression of which is angle-directed nucleation.

As implied by our hypothesis, favorable surface-solute interaction is a prerequisite for angular nanopores to promote nucleation. To verify this point, we changed the chemical makeup of the polymer film from AA-co-DVB to AM-co-DVB (Figure 3-10). This chemistry was selected out of the polymer films tested because, in the absence of pores, it exhibited no effect on aspirin nucleation from butyl acetate, indicating that surface-solute interactions are not sufficiently strong to affect nucleation under these conditions. As expected, patterning of the AM-co-DVB surface with the same angular nanopores did not lead to enhanced nucleation kinetics relative to nucleation on nonporous films.

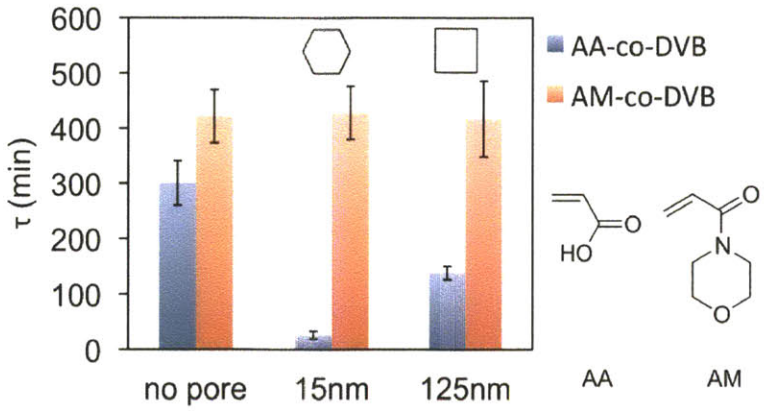

Figure 3-10. Effect of polymer surface chemistry on kinetics of angular nanopore-induced nucleation of aspirin: AA-co-DVB vs. AM-co-DVB. τ is the average nucleation induction time. AM denotes 4-acryloylmorpholine. AA denotes acrylic acid. AM-co-DVB refers to poly 4-acryloylmorpholine crosslinked with divinylbenzene.

It is worth noting that the concept of classical nucleation theory is not employed in our hypothesis, since it is not an appropriate framework for understanding crystal nucleation from

solution despite its popularity. This study provides further evidence of its problematic nature. As predicted by the classical nucleation theory, nucleus formation on concave surfaces should be easier with a lower kinetic barrier relative to that on flat surfaces. In contrast, we observed that nucleation on concave surfaces is more difficult. This discrepancy results partially from the fact that classical nucleation theory fails to account for all the essential degrees of freedom for describing nucleation of a crystal, such as the internal orientational order of the nucleus, which we deem to be an important factor dictating the pore shape effect.

3.5. Conclusions

In summary, we synthesized polymer films with nanopores of various shapes using 'Nanoparticle Imprint Lithography' (NpIL) developed in this work, as well as Nanoimprint Lithography coupled with Interference Lithography. We found that nanopore shape plays a key role in determining the kinetics of surface-induced nucleation probed with a small organic model compound. Angular pores of chosen geometry and surface chemistry promoted nucleation, while spherical pores of the same size did not. We identified angles in the square and the hexagonal pores as active nucleation sites. The pore geometry and specific surface-solute interactions jointly determined which crystal facets would nucleate preferentially. We also showed that favorable surface-solute interactions are required for angular pores to promote nucleation. We further proposed a molecular mechanism by which the pore shape affects nucleation by altering the molecular orientational order near the angles of the pores. Our results provide new insight into surface-induced crystallization, which should find use in many areas of science and technology from controlling pharmaceutical polymorphism to inhibiting ice nucleation on airplanes.

Chapter 4

4. Role of Polymer Microstructures in Gel-Induced Nucleation

4.1. Introduction

In Chapter 3, we investigated the role of surface morphology in heterogeneous nucleation by tuning the shape of surface nanopores, with pore sizes of 10-120 nm. In this chapter, we turn our attention to porous materials with sub-10 nm characteristic length scale for understanding the nanoconfinement effect on nucleation. For organic systems, nanoscopic confinement has been utilized to control nucleation kinetics and polymorphic outcome. Recent studies have shown that mesoporous silica with 5-10 nm pores induced protein crystallization from aqueous solution.[67,68] A Monte Carlo (MC) simulation of nucleation for a one component system in a square shaped open pore indicated the existence of an optimum pore size corresponding to a maximal nucleation rate.[51] However, this hypothesis has not been directly verified by experiments. Moreover, the effect of interaction between the crystallizing species and the confining wall on nucleation was largely neglected. Recently, however, Maheshwari and co-workers clearly demonstrated the importance of fluid-wall interactions in dictating the freezing behavior of nanoconfined liquids.[70] Currently, mechanistic understanding of nucleation from solution under nanoconfinement remains inadequate, and thus systematic studies are necessary to elucidate the effects of confinement and the interfacial interactions on nucleation.

In contrast to rigid materials with nanoscopic pores used in most previous studies (e.g. controlled pore glass,[52,54,69] mesoporous silicon[68] and zeolites[70]), we have employed crosslinked polymer microparticles or "microgels", whose structure is governed by a mesh-like network, to

study and control heterogeneous nucleation of organic molecules. The crosslinked polymers exhibit a number of promising characteristics. First, their mesh structure can be easily manipulated through synthesis conditions, yielding direct control over the degree of nanoscopic confinement. Second, fluid-polymer interactions can be tuned through the choice of polymer chemistry. These attractive properties enabled us to investigate systematically the role of molecular confinement and interfacial interactions on heterogeneous nucleation.

4.2. Experimental Methods

4.2.1. Materials

Crosslinkable poly(ethylene glycol) diacrylate (PEG_MDA) oligomers with average molecular weights M = 200, 400, 575, and 700 g/mol and tri(ethylene glycol) diacrylate (M = 130 g/mol), poly(ethylene glycol) porogen with M=200 g/mol (PEG_{200}), 2-hydroxy-2-methyl-1-phenyl-propan-1-one (Darocur 1173) photoinitiator, Tween20 non-ionic surfactant, and ethanol (99.9%) were purchased from Sigma Aldrich Chemical Co. and used as received with no further purification. Deionized water (18.3 MΩ) was obtained using a Millipore MilliQ purification system. Hydrogel pre-cursors containing 25% PEG_MDA, 25% PEG_{200}, and 5% Darocur 1173 photoinitiator by volume in ethanol were prepared for each of the values of the molecular weight M used. Aspirin (99%) were purchased from Alfa Aesar and acetaminophen (99.0%) from Sigma Aldrich, both used with no further purification.

4.2.2. Microgel Synthesis and Purification

Cuboid microgel particles were synthesized by stop flow lithography (SFL).[87] Microfluidic channels with straight, rectangular cross-section (width = 300 μm, height = 30 μm) were prepared by soft lithography. Briefly, polydimethylsiloxane (PDMS, Sylgard 184, Dow Corning) was poured on an SU-8 photoresist patterned silicon wafer and cured to create a bas-relief

microchannel device. Channels with end reservoirs were cut from the wafer with a scalpel and inlet and outlet ports were punched into the device with a blunt syringe (Small Parts, Inc.) to introduce the hydrogel pre-cursors. A photomask featured with square shapes was designed using AUTOCAD and printed at 50,800 dpi by FineLine Imaging (Colorado Springs, CO). For SFL, the microfluidic device was placed on a translating stage inverted microscope. The inlet channel was loaded with a hydrogel pre-cursor using a pressure-controlled manifold. The mask was placed in the field-stop of the microscope and square features were projected to the pre-cursor by ultraviolet (UV) exposure from a Lumen 200 lamp (Prior) through a wide excitation UV filter set (11000v2: UV, Chroma) while the flow of pre-cursor was stopped. The ultimate feature sizes of the patterned squares were 30 μm x 30 μm, determined through fluorescence imaging of the microchannel during UV illumination. Pulses of UV exposure were obtained by a computer-aided UV shutter (UniBlitz). Incident UV intensities were measured using a UVA Power and Dose meter (ACCU-CAL-30 UVA, DYMAX). In all experiments, the measured exposure was 0.89 μW, and the UV exposure time was fixed at 200 msec. Particles were collected through the outlet channel into a microcentrifuge tube reservoir containing 0.2% v/v Tween20 in a mixture of 38/62 (v/v) ethanol/water. Tween20 was added to the outlet reservoir in order to render the microgels colloidally stable during purification.

SFL was performed until approximately 50,000 particles were synthesized. The reservoir tube containing particles was then removed from the microfluidic device. The tube was placed in a minicentrifuge (Galaxy MiniStar, VWR Scientific) at 6000 rpm for 8 seconds in order to sediment the microgels. The supernatant was removed, and the particles were re-suspended in 1 mL of a rinsing fluid and vortex mixed for 10 seconds. This procedure was repeated several times in order to eliminate any remaining unreacted pre-polymer solution. The first 3 washes

were performed using 38/62 (v/v) ethanol/water with 0.2% Tween20, and 3 final washes were performed using 38/62 (v/v) ethanol/water with no Tween20 to eliminate excess surfactant.

4.2.3. Characterization of Microgel Microstructures

Purified PEG_MDA microgel cuboids were imaged on a DIC inverted microscope under a 20X objective (PLAN NEOFLUAR, Zeiss) in order to determine both the concentration and size of particles swollen in the 38/62 (v/v) ethanol/water crystallization solvent. For size measurements, at least 50 particles were imaged in order to obtain adequate sample statistics. The length of each square face was measured manually using ImageJ (NIH), resulting in average measurements of the particle size, L_s. Table 4-1 below shows the obtained values of L for the different PEG_MDA molecular weights used.

Table 4-1. Properties of PEG_MDA hydrogel microcuboids

$\bar{M}_n$ (g/mol)	L (μm)	R	ξ (nm)
130	32±1	1.05±0.03	0.76±0.08
200	39±1	1.30±0.03	1.02±0.08
400	45±1	1.50±0.03	1.47±0.08
575	48±1	1.60±0.03	1.77±0.08
700	52±1	1.70±0.03	2.01±0.08

Data courtesy: Matthew E. Helgeson

The apparent mesh size, ξ, of PEG_MDA microgels was estimated using a modified Flory-Rehner theory presented previously.[88] The swelling ratio in the 38/62 (v/v) ethanol/water solvent was calculated as $R=L_s/L_0$, where L_0 is the side length of an unswollen particle, assumed here to be the as-synthesized side length (30 μm). From this, the average PEG_MDA molecular weight between cross-links, $\bar{M}_c$, can be calculated from

$$\frac{1}{\bar{M}_c} = \frac{2}{\bar{M}_n} - \frac{\ln\left(1 - R\phi_{p,0}\right) + R\phi_{p,0} + \chi\left(R\phi_{p,0}\right)^2}{\phi_{p,0}\rho_p V_s\left(R^{1/3} - \frac{R}{2}\right)} \qquad \text{Equation 4-1}$$

Where $\bar{M}_n$ is the average molecular weight of the PEG_MDA monomer, ρ_p is the density of the polymer, $\underline{V}_s$ is the molar volume of the solvent, χ is the Flory chi parameter, and $\phi_{p,0}$ is the volume fraction of polymer in the unswollen state, assumed here to be the volume fraction of PEG_MDA in the hydrogel pre-cursor (25%). Subsequently, the mesh size of the hydrogel is given by [89]

$$\xi = R\phi_{p,0}^{1/3}\left(\frac{2C\bar{M}_c}{\bar{M}_n}\right)^{1/2} l \qquad \text{Equation 4-2}$$

Where C is the characteristic ratio and l is the average bond length of the polymer. Mesh sizes for the PEG_MDA microgels was calculated from experimental measurements of R, and the results are listed in Table 4-1. The model parameters used consisted of values for PEGDA of ρ_p=1.12 g/mL, C = 4.0,[90] l = 1.5,[91] and χ=0.514 reported for PEGDA in a mixture of 75:25 water/ethanol.[92] As expected, the apparent mesh size increases with increasing $\bar{M}_n$ of PEGDA, due primarily to the increase in PEG length between cross-links within the hydrogel network.

4.2.4. Nucleation Induction Time Measurement

Experiments were conducted in an RS10 Clarity Solubility Station (Thermo Fisher Scientific). The Clarity station is comprised of 10 cells, each with independent temperature control, heated electrically and cooled by a Peltier element. Aspirin stock solutions of 38mg/ml were made in 38/62 (v/v) ethanol/water mixture and filtered with 0.2μm PTFE syringe filters to remove as much impurities as possible. Pre-cleaned 2-ml HPLC vials were filled with 1.9ml aspirin solution. 20μl PEG_MDA particle suspension prepared in 38/62 (v/v) ethanol/water mixture with particle concentration of 50 ml^{-1} were injected into each aspirin solution contained in the HPLC vial. Six types of samples were prepared: bulk samples without particles, samples with PEG_MDA

particles of M_n=130, 200, 400, 575, 700 g/mol. For each type of sample, 10 HPLC vials were prepared and loaded into 10 cells on the Clarity station. The samples was cooled at a rate of 5°C/min from 35°C to 15°C to achieve a supersaturation of 2.1. The solution was stirred at 700rpm. For acetaminophen system, 1.0 ml 95mg/ml acetaminophen solution in 38/62 (v/v) ethanol/water with or without particles was cooled at a rate of 5°C/min from 35°C to 8°C to achieve a supersaturation of 3.7. The particle concentration in the HPLC vials was kept the same as that in aspirin solution. The acetaminophen solution was also stirred at 700rpm. The onset of nucleation was detected by an IR probe which measures the transmission signal through the solution. When nucleation occurs, the solution becomes turbid rapidly, because the bulk solution is seeded by crystals broken off from the particles due to attrition induced by stirring. The crystal growth rates of the chosen model compounds are much faster than the nucleation rate, hence the time it takes from the onset of nucleation to the massive crystallization event detected by the IR probe can be neglected. The 10 samples were cycled for 5 to 10 times to yield 50-100 nucleation induction time data for the statistical analysis.

The polymorphic outcome for both systems was the stable polymorph at the crystallization condition, with or without the presence of microgels. This result is not surprising given that crystallizing acetaminophen form II or III from solution by cooling without seed has been shown to be elusive,[39,93,94] even more so for metastable forms of aspirin.[5] Particularly, metastable forms of aspirin and acetaminophen haven't been reported at the crystallization condition we used. Acetaminophen form II has been obtained with the presence of polymers,[6,39,95] however, not by cooling but by solvent evaporation method where much higher supersaturation can be generated that are typically unattainable via cooling method as used in this study.

4.2.5. Partition Coefficient Determination

PEG_MDA gels sufficiently large for convenient handling were synthesized by UV polymerization, following the same formulation as the synthesis of PEG_MDA particles used in the crystallization study. 12μl of pre-polymer mixture held in an Teflon well 0.5mm in depth and 5mm in width was subjected to UV irradiation for 1min, and the UV light was generated from 5000-EC UV Curing Flood Lamp purchased from Dymax Corporation. Four replicas were synthesized for each molecular weight M_n. After polymerization, the PEG_MDA gels were immersed in ethanol and put on the shaker overnight to wash out unreacted species. All gels were washed with ethanol for three times before vacuum dried for 30min to remove the solvent ethanol. The gel was weighed at the dry state then immersed in 10ml 38mg/ml aspirin solution in 38/62 (v/v) ethanol/water at 15°C for overnight. The aspirin solution was filtered beforehand to remove impurities. Since the solution together with the gel was kept quiescent, no crystallization was observed during the equilibration period. After equilibration, the gels were taken out, pad dried, weighed to obtain the swollen weight and put in 20ml D.I. water and kept on a shaker. The concentrations of aspirin and ethanol in the aqueous phase were analyzed by UV-Vis spectroscopy and Gas Chromatography, respectively. The standard line for aspirin in water was determined from UV-Vis absorption of 0.02 to 0.2mg/ml aspirin solutions, at 275nm. The UV-Vis absorption spectrum of aspirin in water was taken every hour to obtain the time-lapsing elution profile for estimating aspirin diffusivity in the gel. Aspirin elution from gels with M_n=700g/mol reached equilibrium at around 3 hours, with M_n=400g/mol around 4 hours and with M_n=200g/mol around 5 hours. A simple estimation following $\delta \sim \sqrt{Dt}$, where δ is the penetration depth, which is 0.25mm, half the gel thickness, D the diffusivity of aspirin in the gel was estimated to be 10^{-11} to 10^{-12} m^2/s, which decreases slightly as the decrease of M_n. The total

mass of aspirin eluted out of the gel was calculated from the UV-Vis absorption at t=5h, and was divided by the total mass of solution absorbed by the gel to obtain the mass concentration of aspirin in the gel. Similarly, the mass concentration of ethanol in the gel was calculated from the ethanol concentration in water by Gas Chromatography.

The partitioning of ACM in gels of various mesh sizes was measured following the same procedure as that of ASA. The ACM solution concentration was 95mg/ml for immersing the gels, which was kept at 8°C. The standard line for aspirin in water was determined from UV-Vis absorption of 0.001 to 0.02mg/ml aspirin solutions, at 244nm.

4.3. Results and Discussion

4.3.1. Microgels with Tunable Microstructures

We synthesized a series of microgels comprised of cross-linked polyethylene glycol diacrylate (PEG_MDA) from PEG_MDA pre-cursors of different average PEG molecular weight, M_n. Specifically, stop flow Lithography (SFL)[87] was used to prepare cube-like PEG_MDA microgels (with approximate dimensions of 30 μm x 30 μm x 25 μm) to study heterogeneous nucleation (Figure 4-1a). The hydrogel pre-cursor consisted of 25% PEG_MDA, 25% polyethylene glycol (M_n = 200 g/mol), and 5% photoinitiator in ethanol. The particles were purified in 38/62 (v/v) ethanol/water, resulting in a kinetically stable dispersion of PEG_MDA hydrogel cubes (Figure 4-1b). The use of SFL allows for synthesis of highly monodisperse, non-spherical particles whose faces are easily distinguished by optical microscopy. The monodispersity is also ideally suited to isolate the effects of polymer microstructure on heterogeneous nucleation.

Particles were prepared from a series of PEG_MDA monomers with molecular weight M_n ranging from 130 to 700 g/mol, resulting in microgels with a range of interior mesh structures with differing cross-link density. The structure of the cross-linked hydrogel mesh is typically

described by the so-called "mesh size", which is related to the average molecular weight between cross-links within the polymer network.[89] In order to determine the changes in hydrogel microstructure between particles of different PEG_MDA molecular weight, equilibrium swelling measurements were used to estimate the apparent mesh size, ξ. Specifically, ξ was computed by the Flory-Rehner theory[88] from the swelling ratio of particles measured in 38/62 (v/v) ethanol/water relative to the as-prepared particles, using literature values of model parameters for PEG_MDA.[96] The resulting estimates of ξ (Figure 4-1c) show that the mesh size varies nearly linearly with PEG_MDA molecular weight from 0.7 to 2.0 nm over the range studied, which is consistent with literature values.[96]

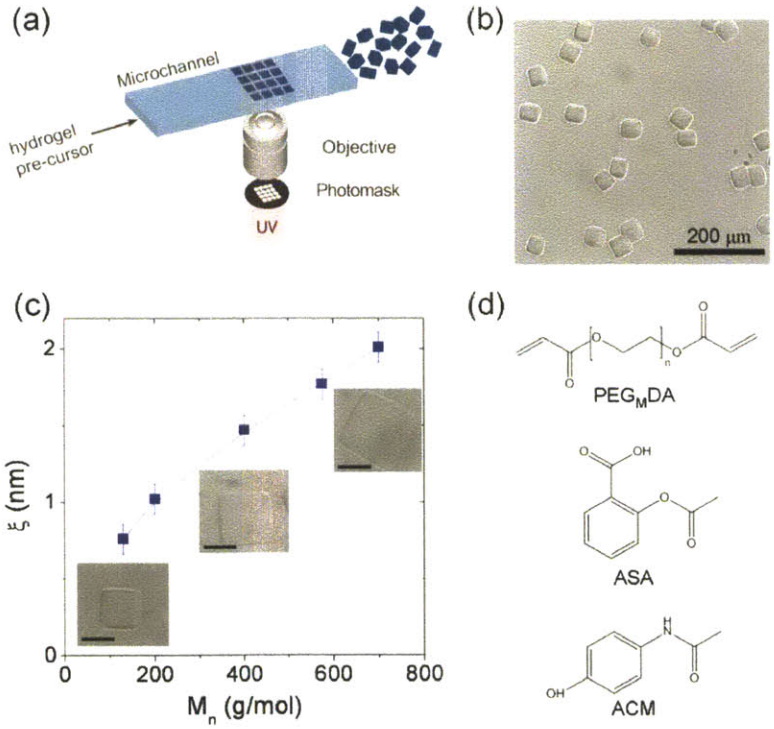

Figure 4-1. Synthesis and characterization of PEG_MDA microgel particles. (a) Schematic diagram of the SFL process. (b) DIC microscopy image of purified $PEG_{400}DA$ microgel cubes suspended in 62/38 water/ethanol. Scale bar is 200 µm. (c) Apparent microgel mesh size versus PEG_MDA molecular weight used in the hydrogel pre-cursor. All measurements are performed in 62/38 water/ethanol at 25 °C. Inset: representative images of swollen particles prepared from respective PEG_MDA molecular weights. Scale bars are 30 µm. (d) Molecular structures of PEG_MDA, ASA, ACM. Image courtesy: Matthew E. Helgeson.

4.3.2. Effect of Gel Microstructure on Nucleation Kinetics

To study the effect of particles with various mesh sizes on nucleation kinetics, aspirin (ASA) and acetaminophen (ACM) were chosen as model compounds, both carrying hydrogen bond donors that could potentially interact with the hydrogen bond acceptors of the polymer mesh. Crystallization of ASA or ACM from a 38/62 (v/v) ethanol/water mixture was induced by cooling, with and without PEG_MDA particles suspended in the solution by stirring. Crystallization in the presence of microgels was found to result in the growth of ASA or ACM crystals on or from within the PEG_MDA particles, as observed by optical microscopy (Figure 4-2). For both systems, the stable polymorph at the crystallization condition was obtained, with or without microgels.

The nucleation kinetics of ASA and ACM templated by PEG_MDA microgels were investigated by measuring the nucleation induction time probability distribution, *P(t)*. The induction time is a useful indicator of the effectiveness of microgels in inducing nucleation because it is highly sensitive to changes in the free energy barrier to nucleation. Due to the stochastic nature of nucleation events, a large number of experiments were performed to obtain the probability distribution of nucleation induction time. The average induction time, τ, was determined from a statistical analysis on the induction time data, described in Chapter 2.

Figure 4-3a shows the statistical analysis of ASA nucleation induction time with and without PEG_MDA particles suspended in a supersaturated aspirin solution at a particle concentration of 15 μg/mL. Clearly, almost all particles successfully promoted aspirin nucleation, except for those prepared with M_n = 130 g/mol PEG_MDA. Specifically, the addition of particles with M_n = 400 g/mol to the aspirin solution dramatically reduced the aspirin nucleation induction time to 66.7 minutes, while under the same experimental conditions, no nucleation event was detected in the

absence of particles. Furthermore, the solute nucleation activity, expressed by the nucleation rate, of the PEG_MDA particles decreased sharply for both $M_n < 400$ g/mol and $M_n > 400$ g/mol. This observation suggests that there exists an optimum mesh size for accelerating nucleation from solution.

Nucleation induction time measurements on the ACM system (Figure 4-3b) further demonstrate the overall success of PEG_MDA particles in facilitating nucleation. In most cases, the addition of particles in ACM solution led to a shorter average induction time compared with the bulk. Furthermore, as in the ASA system, an optimum mesh size corresponding to the shortest nucleation induction time was also observed. However, the effect of PEG_MDA particles was not as dramatic for ACM as in the case of ASA, as evidenced by the following observations. First, the addition of PEG_MDA particles at best resulted in approximately a ten-fold enhancement in the nucleation rate of ACM (Figure 4-3d), whereas for ASA, the degree of enhancement was by many orders of magnitude (Figure 4-3c). Second, the particles were unable to induce ACM nucleation at the lower supersaturation levels (S=2.7, 3.3), within the experimental time frame. At S=3.7, when the particles began to promote ACM nucleation, the bulk solution started to crystallize at a detectable frequency, implying that this condition was fairly close to the upper bound of the metastable zone (Figure 4-3d). As for ASA, the PEG_MDA particles showed effects at a much lower supersaturation (S=2.1). The fact that there was no detectable bulk nucleation under these conditions indicates the solution was far from the boundary of the metastable zone (Figure 4-3c). These observations suggest that the PEG_MDA particles are less effective in inducing ACM than ASA nucleation.

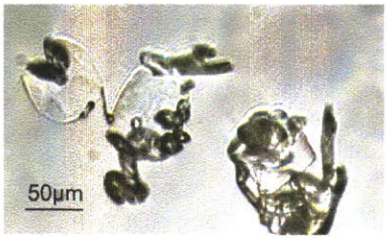

Figure 4-2. ASA crystals on $PEG_{700}DA$ particles as crystallized from 38mg/ml ASA solution in 38/62 (v/v) ethanol/water with 15μg/mL $PEG_{700}DA$ particles at 15°C, solution stirred at 700rpm.

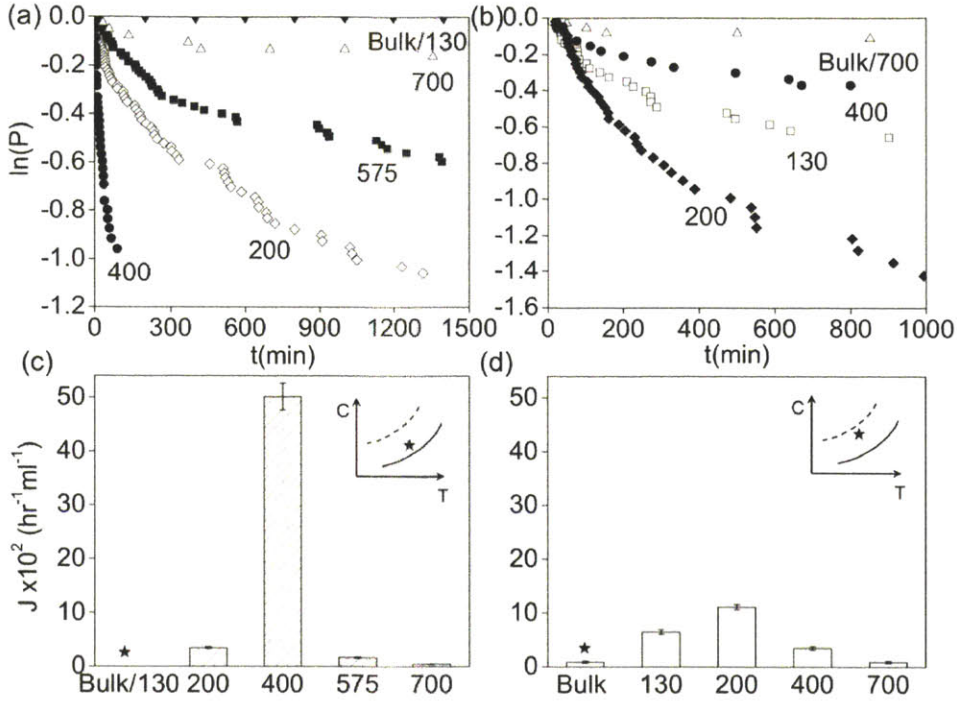

Figure 4-3. The nucleation kinetics of ASA and ACM with PEG_MDA particles of various M_n. (a) & (b) Statistical analysis of nucleation induction time for ASA (a) and ACM (b) at supersaturations (S) of 2.1(a) and 3.7(b). (c) & (d) Nucleation rates of ASA (c) and ACM (d). Nucleation rate J was calculated from the average induction time by $J=1/\tau V$, where τ is the average induction time, and V is the volume of solution. Inset: Schematics illustrating the relative position of the bulk solution in the metastable zone under the crystallization conditions. C and T represent the solute concentration and the temperature, respectively.

Table 4-2. Average nucleation induction times of ASA with the presence of PEGDA microgels.

M (g/mol)	Bulk/130	200	400	575	700
τ (min)	Not detectable	1052	66.7	3500	210000
β	NA	0.52	0.69	0.52	0.36
R^2	NA	0.99	0.96	0.96	0.92

Supersaturation S=2.1. Induction time distribution data were fitted with stretched exponentials via nonlinear least square regression: $P=\exp[-(t/\tau)^{\beta}]$, where P is the probability to observe no crystallization event within time t. The R^2 value corresponding to $PEG_{700}DA$ samples is lower since much fewer samples crystallized within the experimental time frame.

Table 4-3. Average nucleation induction times of ACM with the presence of PEGDA microgels.

M (g/mol)	Bulk	130	200	400	700
τ (min)	37000	1600	480	5300	37000
β	0.50	0.54	0.72	0.50	0.50
R^2	0.97	0.96	0.96	0.97	0.97

Supersaturation S=3.7. Induction time distribution data were fitted with stretched exponentials via nonlinear least square regression: $P=\exp[-(t/\tau)^{\beta}]$.

The nucleation induction time statistics can be faithfully described by stretched exponentials (Table 4-2 and Table 4-3), $P=\exp[-(t/\tau)^{\beta}]$, where P is the probability to observe no crystallization event within time t, τ the average induction time. The stretched exponential exponent β serves as a measure for the spread of time scales[97] characterizing the nucleation process, or the distribution of kinetic barriers[98] arisen from the heterogeniety of the system. In our system, such heterogeniety can be attributed to the heterogeneity of the polymer microstructure (see detailed discussion in Chapter 5), which will result in a distribution of nucleation sites arising from spatial variations in both the mesh size and chemical composition of the hydrogel at nanometer length scales. It is interesting to note that β varies significantly with the average mesh size of the microgel. Aforementioned, we found that the polymer mesh size has a profound impact on the nucleation kinetics and there exists an optimum average mesh size corresponds to the fastest nucleation rate. At the optimum average mesh size, β is found to be the highest in both the cases of ASA and ACM (Table 4-2, M = 400 g/mol; Table 4-3, M = 200 g/mol). This is probably because, out of various types of nucleation sites in the microgel, the one with the optimum mesh size and conformation is dominant in quantity and activity, such that the majority of nucleation events take place at this type of nucleation site, leading to a narrower distribution of nucleation time scales. Taking this senario to extreme, β should approach unity when the activity of a single type of nucleation site is so high that other nucleation sites are inactive by comparison.

4.3.3. Role of Polymer-Solute Interactions

We hypothesize that the success of PEG_MDA particles in facilitating ASA and ACM nucleation results from favorable interactions between the solute and the PEG_MDA polymer matrix in the solution environment. To prove this hypothesis, we first quantified the partitioning of aspirin between the PEG_MDA gel phase and 38/62 (v/v) ethanol/water to determine the actual concentration of aspirin in the particles. PEG_MDA gels sufficiently large for convenient handling were synthesized by UV polymerization, following the same formulation as the synthesis of PEG_MDA particles used in the crystallization study. As shown in Figure 4-4, ASA was concentrated within the PEG_MDA particles by as much as four-fold with respect to the bulk, while the ethanol concentrations remained comparable to that of the bulk. Besides, the partition coefficient for ASA is consistently high for all PEG_MDA molecular weights and remains relatively insensitive to the variation in mesh size. This result indicates that the interaction between aspirin molecules and the polymer matrix is favorable as compared to that between aspirin and solvent.

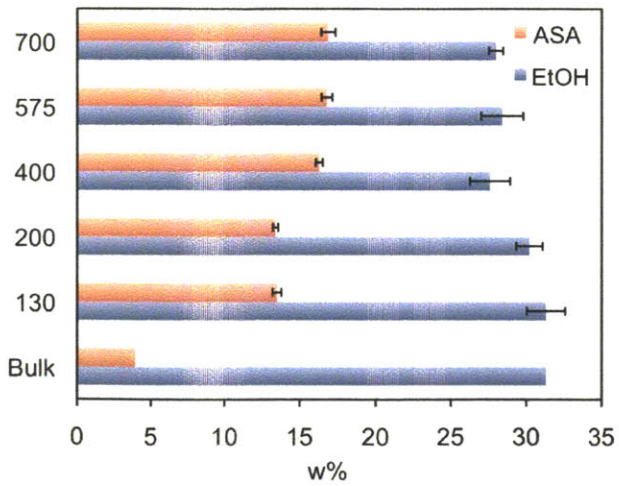

Figure 4-4. Composition of ASA solution in the PEGDA gel phase compared with the bulk phase. Particles of various mesh sizes are denoted by corresponding M_n. The compositions were given in weight percentage.

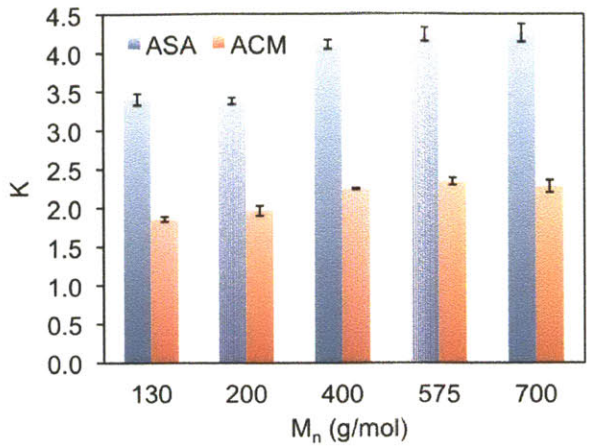

Figure 4-5. Partition coefficient, κ, of ASA and ACM in the PEG_MDA gel, defined as the ratio of solute concentration in the PEG_MDA gel to that in the bulk.

Similarly, ACM also interacts favorably with the PEG_MDA matrix, leading to a concentration approximately twice as high as in the bulk (Figure 4-5), supporting the observation that PEG_MDA particles are generally effective in inducing ACM nucleation. ACM is less concentrated in the PEG_MDA gel phase than ASA (Figure 4-5), indicating weaker interactions with the PEG_MDA matrix. These observations support the hypothesis that polymer-solute interactions contribute to enhanced nucleation activity, since the PEG_MDA particles are less effective in inducing ACM nucleation than that of ASA.

The results discussed above imply that in addition to their microstructures, the effectiveness of the polymeric particles in promoting nucleation also relies on their interactions with the solute. Furthermore, they indicate that the mechanism of PEG_MDA particle-induced nucleation could be partially explained by the higher solute concentration inside the particles due to the effect of preferential partitioning. However, higher solute concentration in the particles alone is insufficient to facilitate nucleation, considering that particles with M_n=130 g/mol do not induce aspirin nucleation despite a high partition coefficient comparable to that of other particles (likewise for ACM nucleation in the presence of particles with M_n=700 g/mol). In addition, a

higher concentration may not result in a higher supersaturation since the solubility in the swollen microgel may be different from that in the bulk, which is further discussed in Chapter 5.

Interestingly, previous studies have shown, contrary to our findings, that strong polymer-fluid or polymer-solute interactions led to the opposite nucleation behavior. Konno and Taylor found that the crystallization of amorphous felodipine was inhibited in polymer-felodipine solid dispersions when the polymers interact with the drug molecule via hydrogen bonding.[99] Vidal *et al.* also found that nucleation of lysozyme from solution was retarded in silica gels with mesh sizes ranging from 10nm to 1μm due to adsorption of protein on the gel surface.[100] An important distinction between our study and the aforementioned studies lies in the microstructure of the polymer present in the crystallization system, among other factors. In addition, our observations that the solute nucleation kinetics are quite sensitive to the polymer mesh size and the existence of an optimum mesh size also imply that the microstructure of the polymer particles plays a crucial role in controlling the nucleation behavior.

4.3.4. Mesh Size Effect

The role of gel microstructure in controlling nucleation can be understood in terms of the effects of the polymer mesh on molecular events in solution leading to nucleation. Nucleation of crystalline solids from solution is preceded by the creation of a distribution of molecular clusters via density fluctuation and alignment of molecules within the cluster via structure fluctuation. [16] This cluster formation is governed by effective solute-solute interactions, which are affected by the presence of the polymer mesh via polymer-solute interactions. On one hand, strong polymer-solute interactions lead to higher solute concentration in the polymer gel, which could potentially facilitate solute-solute interactions; on the other hand, it restricts the motion of solute molecules adsorbed to the polymer mesh, and hence may inhibit solute-solute interactions. This

confinement effect manifests itself in solute diffusivities two to three orders of magnitude lower in the gel than in the bulk, which we estimated from the solute elution profiles from saturated gels to pure solvent. Given strong polymer-solute interactions and low solute-to-polymer ratios in the gel, it is plausible that most solute molecules are associated with the polymer chain for an extended period of time at high volume fraction of polymers, which may inhibit solute-solute interactions necessary for nucleation. However, if the microstructure of the polymer mesh is such that it brings enough absorbed solute molecules to within a sufficient proximity, the confinement effect could instead reinforce solute-solute interactions, which helps reduce the barrier to nucleation.

In our study, the optimum mesh size for inducing ASA nucleation was found to be approximately 15Å, and the diameter of ASA molecules about 6Å (estimated from the crystal density). It is probable that the optimum mesh size allows for aspirin molecules associated with polymer chains to come within sufficient proximity to form a nucleus, given the proper orientation (as would also be the case with ACM). However, as the mesh size becomes smaller, a solute 'sees' more polymer chains than other solute molecules, which prevents the formation of large enough solute clusters; for larger mesh sizes, less solutes are associated with the polymer chain, hence the polymer-solute interaction is less effective in facilitating the solute-solute interaction. Based on the above analysis, we hypothesize that the key to controlling nucleation by nanoconfinement lies in manipulating the effective solute-solute interaction, which is strongly affected by polymer-solute interactions and the spatial confinement imposed by the polymer microstructure, the interplay of which gives rise to the observed optimum mesh size for expediting nucleation. To further test this hypothesis, we performed experiments in which the ASA crystallization temperature was lowered from 15°C to 8°C, thereby increasing the

supersaturation from 2.1 to 3.4. Since this change in supersaturation is significant whilst the absolute temperature was only altered by 2%, this experiment primarily probes the effect of increased supersaturation, which should enhance effective solute-solute interactions due to increased density fluctuations. As a result, the observed optimum mesh size decreased from 15Å to 10Å at the higher supersaturation level (Table 4-4). This supports our hypothesis since fewer solute molecules are needed to overcome the nucleation barrier, which is lowered due to higher density fluctuations.

The mesh size effect is revisited in Chapter 6 and summarized with Figure 6-14.

Table 4-4. ASA average nucleation induction times (τ) with PEG_MDA microparticles of various mesh sizes at higher supersaturation level.

M_n(g/mol)	130	200	400	575	700
τ (min) S=3.4	330±60	**52±3**	123±7	NA	240±20

ASA crystallization was performed at the supersaturation level 3.4. The standard errors of average induction times were calculated from the standard error values of data regression.

4.4. Conclusions

We have demonstrated a new approach to controlling nucleation from solution through the use of polymeric microparticles with tunable microstructure. We found that the nucleation kinetics of aspirin and acetaminophen were very sensitive to variation of the polymer mesh size. Furthermore, an optimum mesh size exists that dramatically enhanced nucleation kinetics, and the overall degree of enhancement was related to the extent of polymer-solute interactions. The uniqueness of employing polymeric microgels to control heterogeneous nucleation from solution is two-fold. First, their microstructure and chemical makeup can be easily tuned over a wide range. Second, their ability to alter the solute concentration in the microgel via thermodynamic partitioning presents an advantage over other types of materials for controlling nucleation. In addition, with PEG-based polymers being biocompatible, these results show promise in a wide

range of applications, from designing nucleants for crystallizing small and macro- molecules to enabling multifunctional pharmaceutical excipient and drug-delivery vehicles.

Chapter 5

5. Role of Molecular Interactions in Gel-Induced Nucleation

5.1. Introduction

As we demonstrated in previous chapters, interfaces present in a metastable liquid are believed to have a profound impact on its nucleation behavior.[3] Considerable strides have been made over the last few decades towards understanding the effect of interfaces on nucleation and several mechanisms have been proposed. The epitaxy mechanism has been well established to describe crystal formation on crystalline surfaces[32,58] or surfaces with two-dimensional symmetry.[26,28,73] Surfaces may also affect nucleation via polarization matching with the crystallizing molecule when both the surface and the crystal exhibit net dipole across the surface/crystal interface.[42,43] These mechanistic understanding should provide guidance for designing surfaces to control crystal nucleation. However, the applicability of these approaches is restricted to a large extent, because the surface properties involved are not freely adjustable catering to the system of interest, and one is very much limited to surfaces with 3D or 2D symmetry, such as crystal facets, self-assembled monolayers, and Langmuir-Blodgett films, etc. Non-crystalline polymeric materials offer a promising alternative, whose structure, topology and chemistry are easily tunable over a wide range by a variety of established fabrication methods, as shown in previous chapters.[77,80,101] Particularly, we have demonstrated polymer gels with tunable microstructures as exceptional materials for controlling nucleation kinetics (Chapter 4).[80] Polymer gels are unique in their ability to concentrate solute molecules via thermodynamic partitioning driven by favorable

polymer-solute interactions, and our previous finding suggested that such intermolecular interactions may hold key to the effectiveness of polymer gels in promoting nucleation.

Intermolecular interactions have been demonstrated to play an important role in dictating the nucleation behavior at interfaces.[39,77] However, mechanistic understanding is still insufficient to enable rational design of surface chemistry for controlling nucleation of molecular crystals from solution. The complexity partially arises from weak intermolecular interactions in molecular systems relative to ionic, metallic and covalent crystals, flexible molecular conformations and intricate solvent effects. In practice, the influence of intermolecular interactions on nucleation is often convoluted with other factors such as surface lattice structures, surface morphology, etc, making it more challenging to study.

This chapter aims to elucidate the role of intermolecular interactions in gel-induced nucleation and its interplay with the effect of polymer microstructures on nucleation. To this end, we chemically modified polymer microgels via copolymerization and studied its effect on nucleation kinetics as compared to unmodified microgels. We found that nucleation kinetics of model compounds is very sensitive to the polymer-solute interactions, and dramatic acceleration of nucleation was observed when the strength of polymer-solute interactions was increased markedly. Besides, the functionalized microgels left distinct signature on nucleation induction time distribution, featuring two characteristic time scales, which may suggest chemical heterogeneity at nanometer scale due to copolymerization. We further explored the underlying mechanism from the perspective of adsorptive partitioning and templating effect to interpret the role of intermolecular interactions in gel-induced nucleation. Hopefully, our results help advance fundamental understanding of nucleation at complex interfaces in molecular systems and facilitate rational design of materials for controlling nucleation from solution.

5.2. Experimental Methods

5.2.1. Microgel Synthesis and Structural Characterization

All materials used are listed in Chapter 4. For PEGDA microgel pre-cursors, solutions containing 25% PEG_MDA, 25% PEG_{200}, and 5% DC1173 by volume in ethanol were prepared for each of the values of the molecular weight M used. Similarly, for PEGDA-co-AM microgels, solutions containing 15% PEG_MDA, 15% AM, 25% PEG_{200}, and 5% DC1173 photoinitiator by volume in ethanol were prepared for each of the values of the molecular weight M used. Microgels were synthesized by SFL as described in Chapter 4.

Microstructures of the microgels were characterized by equilibrium swelling experiments (Chapter 4) and small angle neutron scattering (SANS). SANS was performed at the National Institute of Standards and Technology Center for Neutron Research (NCNR). Samples were prepared by loading hydrogel pre-cursors (with the compositions previously described) for the $PEG_{200}DA$, $PEG_{700}DA$, $PEG_{200}DA$-co-AM, and $PEG_{700}DA$-co-AM microgels into standard titanium scattering cells with a path length of 1 mm. In order to polymerize the material, samples were irradiated with a handheld UV lamp with an output intensity of 0.2 mW/cm^2 for 1 minute, resulting in a total UV dose which is approximately equivalent to that supplied during SFL of microgel particles.

SANS measurements were carried out on the NG7 30 m SANS instrument with the 10CB sample environment. Temperature control was obtained using a Julaba temperature bath unit at 25 °C, and samples were left to equilibrate for at least 30 min prior to measurement. Scattering using incident neutrons of wavelength λ = 6 Å and a wavelength spread (FWHM) of $\Delta\lambda/\lambda$ = 11% was collected at detector distances of 1 m with 20 cm offset, 4 m, and 13.5 m for high-q measurements. Scattering using incident neutrons of wavelength λ = 8.09 Å and a wavelength

spread (FWHM) of $\Delta\lambda/\lambda = 11\%$ was collected at a detector distances of 15.3 m for low-q measurements. USANS measurements were performed on the BT5 perfect crystal diffractometer within the 6CB sample environment. Temperature control was obtained using a Julaba temperature bath unit, and samples were left to equilibrate for at least 30 min prior to measurement. Data were reduced using NIST IGOR software package[102] in order to obtain the absolute scattered intensity, $I(q)$. The incoherent background intensity, I_{bk}, was determined using a Porod analysis of the data at high q-values.[102]

5.2.2. Quantification of Polymer-Solute Interactions

Partition coefficient measurements. Partition coefficients of ASA in PEGDA-co-AM gels from its bulk solution were determined following a similar method described in Chapter 4.[80] In brief, a series of gels with varying mesh sizes of approximately 5mm in diameter and 0.5mm in thickness were synthesized via UV polymerization following the same formula as used in the microgel synthesis. The residue solvent, porogen and monomer molecules were removed by extensive washing with solvent ethanol and subsequent vacuum drying. The dry gels were then immersed in excessive volume of 38mg/ml ASA solution in 38/62 (v/v) ethanol/water at 15°C for overnight. After equilibrium swelling was reached, the swollen gels were pad dried and dropped into excessive volume of water to release ASA. The total mass of ASA released was determined by measuring the equilibrium concentration of its degradation product in water, salicylic acid (SA), with UV-Vis spectroscopy, after ASA aqueous solution was aged for a week to achieve complete hydrolysis. The ASA partition coefficient was calculated as the ratio of ASA mass fraction in solution absorbed by the gel to that in bulk solution. Partition coefficient of ACM was determined by the same method. The gels were immersed in 95mg/ml ACM solution at 8°C instead. Since ACM is stable in water, its concentration was determined directly after the

swollen gel was immersed in water for 24 hours. Three to four independent repeats were carried out for each type of sample to obtain the standard error of the partition coefficient.

Isothermal titration calorimetry (ITC). ITC measurements were performed on a TA Instruments NanoITC calorimeter. All experiments were performed at 23 °C using injections of ΔV = 10 μL of titrant, with a waiting time of 1000 sec in between injections and 25 injections per measurement. For all measurements, The differential heat input, $q(t)$, was measured as a function of time t over all injections, followed by integration of $q(t)$ over each individual injection to obtain the molar heat of injection, $Q(T,P,c)$. The molar heat of injection can then be cumulatively added over all previous injections, yielding the total molar heat, $Q_{tot}(T,P,c)$.

The primary measurement involves titration of a solution containing c_{inj} = 21 mg/mL ASA in 38/62 (v/v) ethanol/water (loaded in the injection syringe) into a suspension containing microgel particles at a concentration of 1 particle/μL in 38/62 (v/v) ethanol/water. For this process, the molar heat of injection contains several contributions

$$Q(T,P,c) = c_{inj}\Delta V\left(\Delta H_{ASA-gel}(T,P,c) + \Delta H_{dil}^{ASA}(T,P,c) + \Delta H_{dil}^{gel}(T,P,c)\right) \quad \text{Equation 5-1}$$

where $\Delta H_{ASA-gel}$ is the molar enthalpy of interaction between ASA and the microgel particles, and ΔH_{dil}^{i} is the molar enthalpy of dilution of component i (ASA or gel, respectively) in 38/62 (v/v) ethanol/water. In order to determine $\Delta H_{ASA-gel}$, independent measurements of the ΔH_{dil}^{ASA} and ΔH_{dil}^{gel} were made by performing measurements where 21 mg/mL ASA in 38/62 (v/v) ethanol/water was injected into a sample containing only 38/62 (v/v) ethanol/water without particles, and where 38/62 (v/v) ethanol/water without ASA was injected into a 1 particle/μL suspension 38/62 (v/v) ethanol/water. Subsequently, eq. (X) was used to subtract the measured dilution enthalpies from the initial measurements of $Q(T,P,c)$ in order to obtain $\Delta H_{ASA-gel}$.

Subsequently, the total, cumulative enthalpy evolved over all injections due to polymer-solute interactions, $\Delta H^{tot}_{ASA-gel}$, is calculated by summing the instantaneous enthalpy of interaction, $\Delta H_{ASA-gel}$, over all injections:

$$\Delta H^{tot}_{ASA-gel}(T,P,c) = \sum_{c_j=0}^{c} \Delta H_{ASA-gel}(T,P,c_j) \qquad \text{Equation 5-2}$$

where c_j is the concentration of the j^{th} injection.

5.2.3. Preferred Crystal Orientation via XRD

Polymer films of various PEG molecular weights were synthesized via UV polymerization using pre-polymer mixtures of the same formulations as used for microgel synthesis, but without adding solvent ethanol and porogen PEG200. 30μl pre-polymer mixture was sandwiched between a glass slide and a quartz slide, both 75mm x 25mm in size. The glass slide was silanized with vinyl trichlorosilane, which co-polymerizes with the monomer to graft the polymer film to the glass substrate via covalent bonds. The quartz slide was used as a template to make polymer films with the minimum surface roughness possible. The sandwiched pre-polymer mixture was subjected to 70 mW/cm^2 UV light for 5min to complete the polymerization, with the whole sample area irradiated fairly uniformly in the 5000-EC UV Curing Flood Lamp (Dymax Corporation). The quartz slide was subsequently lifted to leave the flat and smooth polymer film conformed to the glass substrate. After synthesis, the polymer films were immersed vertically in 25mg/ml ASA solution in 38/62 (v/v) ethanol/water mixture, which was filtered with 0.45μm PTFE membrane syringe filter before adding the polymer films. The solution was then sealed and cooled from 25°C to 3°C, and visually inspected every hour. Once crystals were spotted, the polymer film was withdrawn from the solution to terminate crystallization and immediately dipped into D.I. water tank vertically to remove loosely attached crystals from bulk (ASA is

essentially insoluble in water at 3°C). The backside of the glass substrate was used as a control to determine if all loose crystals were removed from the polymer film. Bulk crystals were obtained at the same condition and serves as the control sample for XRD analysis. For ACM system, same procedure was carried out with 80mg/ml ACM solution in 38/62 (v/v) ethanol/water mixture.

The specific crystal planes grown from the polymer film was analyzed using PANalytical X'Pert PRO Theta/Theta Powder X-Ray Diffraction System with Cu tube and X'Celerator high-speed detector. 20mm x 20mm sample area was irradiated by the X-ray in one scan using programmable divergence slit with 20mm irradiated length and 20mm mask to ensure enough crystals on the polymer film were sampled to yield the statistically representative preferred orientation. Three scans were performed with one polymer film to cover almost the entire surface area. Since only the diffraction from the crystal plane parallel to the polymer film surface was seen by the X-ray detector, the peak that was significantly more intense relative to that of bulk crystals corresponds to the preferred nucleation face.

5.3. Results and Discussion

5.3.1. Structural Analysis on Polymer Microgels

Two model polymer chemistries were chosen for synthesis of microgel particles to use in gel-induced nucleation studies. The first were crosslinked homopolymer gels of poly(ethylene glycol) diacrylate (PEG_MDA) of various monomer molecular weight, M (g/mol). The second were co-polymers of PEGDA and 4-acryloylmorpholine (AM). AM was selected as a co-monomer to functionalize the PEGDA gel because it contains multiple hydrogen-bond acceptors, which may interact favorably with the hydrogen-bond donors of aspirin (ASA) and acetaminophen (ACM), the model compounds employed in this study. Several other co-monomers, including those containing carboxylic and hydroxyl groups, were initially screened

for study. However, incorporation of such hydrogen bond donor groups into the polymer gel led to significant aggregation in organic solvents, preventing their use in well-controlled nucleation studies.

PEGDA microgels were prepared from a range of monomers with M = 130-700 g/mol using pre-cursor fluids containing a fixed concentration of PEGDA of 25 vol%. Similarly, PEGDA-co-AM microgels were prepared using the same range of monomer molecular weights containing 15 vol% PEGDA and 15 vol% AM. The range of PEGDA molecular weights thus represents a range of crosslinking density across the different microgel particles, resulting in a range of the average mesh size, ξ, of the crosslinked gel; i.e., the average distance between crosslinks within the polymer network. The particular pre-cursor concentrations of PEGDA and AM used were chosen to closely match ξ between the two systems in order to isolate the effect of polymer chemistry on nucleation kinetics.

The microstructure of PEGDA and PEGDA-co-AM gels was characterized in order to better elucidate the nature of polymer-API interactions and their effect on nucleation. Estimates of ξ were obtained from equilibrium swelling measurements using a procedure described previously. Figure 5-1 compares the apparent mesh size from swelling measurements (closed symbols) obtained previously measured for PEGDA microgels (blue)[80] to that obtained for PEGDA-co-AM microgels (red) with increasing M. We find that the incorporation of AM into the PEGDA hydrogel network results in a mild increase in mesh size on the order of 10-25% over the range of PEGDA molecular weights studied. This is expected, since the effective lengthening of the acrylic polymer backbone by insertion of AM monomers is small compared to the overall length of PEG chains.

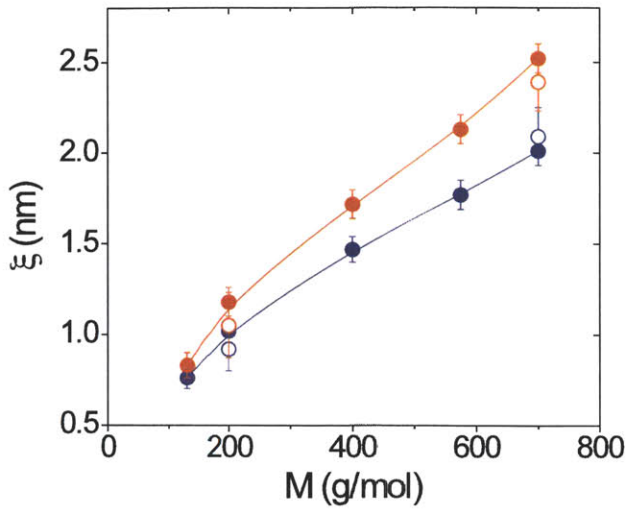

Figure 5-1. Mesh size of PEGDA (blue) and PEGDA-co-AM (red) hydrogels measured in 38/62 (v/v) ethanol/water at 23 °C using estimated by equilibrium swelling measurements (closed symbols) and SANS analysis (open symbols). Image courtesy: Matthew E. Helgeson.

In order to examine the microstructure of the PEGDA and PEGDA-co-AM gels in further detail, as well as to validate several assumptions made in the equilibrium swelling measurements, small angle neutron scattering (SANS) measurements were performed on representative hydrogel samples with M = 200 g/mol and 700 g/mol. The corresponding absolute intensity spectra, I(q) - I_{bk} are shown in Figure 5-2, where the incoherent background intensity, I_{bk}, has been subtracted. The data were fit to a generalization of the Debye-Bueche model,[103]

$$I(q) = \frac{A}{1+(\xi q)^m} + \frac{B}{\left[1+(\Xi q)^n\right]^2} + I_{bk} \qquad \text{Equation 5-3}$$

The first term is used to describe local fluctuations of individual chains with excluded volume constrained by crosslinks,[104] whose length scale is set by the mesh size, ξ. The scaling exponent *m* is related to the solvent quality of the polymer chains; e.g., m = 2 for Gaussian chains, whereas m < 2 for chains in a good solvent.[105] The second term describes the low-q structure, and arises from large-scale heterogeneity (either static or dynamic) within the material, where Ξ is the characteristic length scale of structural inhomogeneity. The scaling exponent *n* is related to the nature of the interface between inhomogeneous regions of the material. It is typically assumed

that $n = 2$, corresponding to sharp interfaces between inhomogeneities.[106] We find that this restrictive assumption generally results in poor fits to the SANS data collected for both PEGDA and PEGDA-co-AM microgels. Therefore, we generalize the Debye-Bueche model by leaving n as an adjustable parameter. This is empirically equivalent to assuming that the density profile between homogeneities can be described by scattering with a surface fractal dimension of n^2; i.e., $n^2 = 4$ for a sharp interface, whereas $3 < n^2 < 4$ for a diffuse interface.

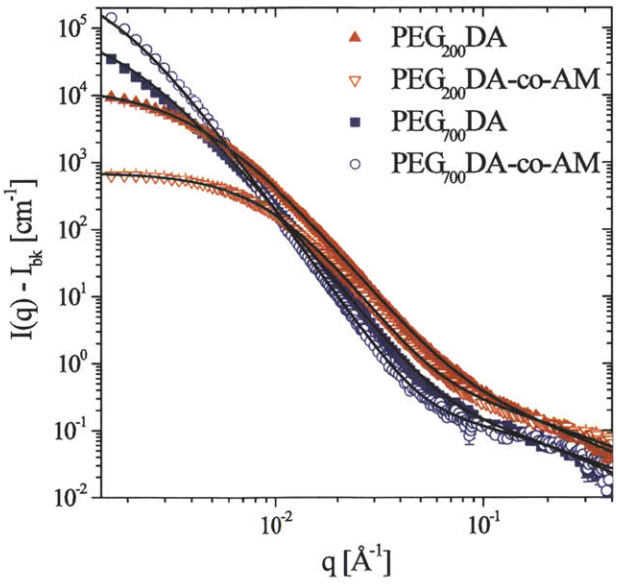

Figure 5-2. Absolute SANS intensity spectra for the polymer hydrogels indicated. Solid lines give best fits to the Debye-Bueche model, Equation 5-3. Image courtesy: Matthew E. Helgeson.

Table 5-1. Structural properties of PEGDA and PEGDA-co-AM hydrogels from SANS analysis.

Polymer	M_n(g/mol)	ξ (nm)	m	Ξ (nm)	n
PEGDA	200	0.92±0.06	1.88	23.3±1.4	1.88
	700	2.09±0.08	1.59	53.6±1.4	2.16
PEGDA-co-AM	200	1.05±0.06	1.38	10.4±1.6	1.80
	700	2.39±0.08	1.34	61.6±1.2	2.04

Eq. 5-3 was fit to the experimental data, and the best-fit model predictions are shown in Figure 5-2, with the corresponding model parameters are listed in Table 5-1. We find that the generalized Debye-Bueche model gives a quantitatively accurate description of the data. Thus, we conclude that the microstructure of both PEGDA and PEGDA-co-AM microgels exhibit

significant structural heterogeneity over length scales ranging from 10-60 nm. The length scale for heterogeneity, given by Ξ, ranges from 10-20ξ for the $PEG_{200}DA$ polymers, and decreases upon addition of the AM co-monomer. By contrast, Ξ is approximately equal for both the $PEG_{700}DA$ homopolymer and its AM co-polymer, with a value that of $\Xi \sim 25\xi$. Furthermore, the Porod exponent $n \sim 2$ for the $PEG_{700}DA$ gels suggest sharp interfaces between structural inhomogeneities, whereas $n \sim 1.8$-1.9 for the $PEG_{200}DA$ samples suggests a transition to more diffuse interfaces at low PEGDA molecular weight.

Although the nature of this heterogeneity is presently unclear, such structure typically arises from microphase separation within the hydrogel,[107] where the structure exhibits distinct regions of different density. For the PEGDA and PEGDA-co-AM gels studied here, the phase separation could either be between the polymer and solvent, between the various constituent moieties of the polymer (ethylene glycol, acrylate, and AM), or a combination of both phenomena. For example, previous studies have shown that formation of PEGDA hydrogels in the presence of high molecular weight PEG "porogens" leads to polymer phase separation and the formation of micron-scale pores within the hydrogel.[108] However, optical imaging of the microgel particles considered here exhibits no evidence of such large-scale porosity. Turning to our SANS results, we note that both Ξ and n are found to primarily depend on the PEGDA monomer molecular weight, and not the presence of AM co-monomer. Since the primary chemical difference between the $PEG_{200}DA$ and $PEG_{700}DA$ monomers is the relative amount of acrylic groups compared to ethylene glycol units, we thus conclude that structural heterogeneity within the hydrogels is driven by microphase separation of the polymerized acrylic groups.

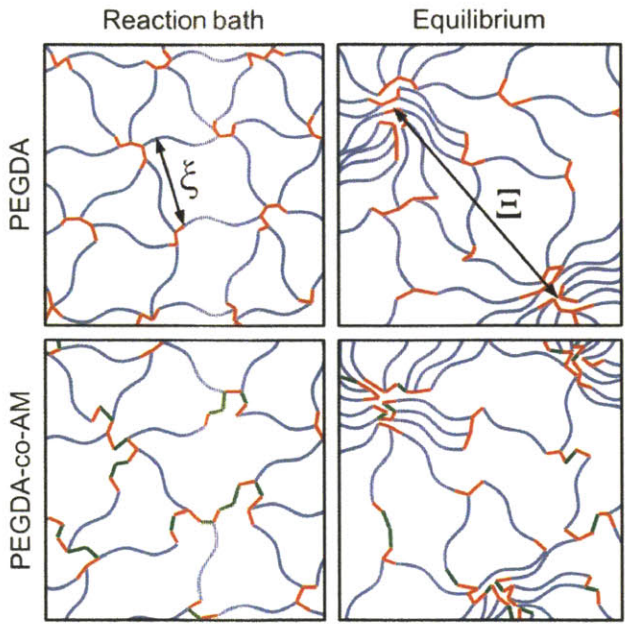

Figure 5-3. Schematics of microgel structures inferred from SANS measurements. Blue, red and green chains denote the PEG subchain, acrylate and AM segments, respectively. Image courtesy: Matthew E. Helgeson.

Figure 5-3 shows diagrams of possible structures for the PEGDA (top) and PEGDA-co-AM (bottom) hydrogels under such a scenario. In the so-called "reaction bath" in which the crosslinked network is formed (left), the nascent hydrogel exhibits homogeneous microstructure.[107] At equilibrium (right), however, phase separation of the acrylic backbone chains leads to phase separation, where acrylate-rich regions coexist with acrylate-poor regions. This depiction of the microstructure is consistent with the observed trends in SANS data, as follows. Since the poly(ethylene glycol) strands of the gel must always be attached at the ends by acrylic groups, the length scale Ξ will be primarily determined by the length of PEG chains (blue) between neighboring acrylic backbone chains (red). This explains the observed trend in Ξ, which increases for 3-5 fold as the PEGDA molecular weight is increased from 200 g/mol to 700 g/mol. Since the addition of AM co-monomer (green) within the gel must occur along the acrylic backbone chains, the AM groups will thus primarily be contained within the AM-rich regions. This explains the fact that neither Ξ nor n change significantly upon co-polymerization with AM, since the AM groups will not significantly affect the structure of the AM-poor regions.

We now turn our attention to the smaller length scale structure of the gels, given by the mesh size ξ and free volume exponent m. Given the previous discussion, it is clear that the definition of a uniform average mesh size, such as that obtained from swelling measurements, is inadequate to sufficiently describe the microstructure of the microgels. Surprisingly, however, we find that the measured values of ξ from the SANS measurements are generally in fair quantitative agreement with those measured by equilibrium swelling measurements (Figure 5-1). It is reasonable to presume that averaging of the mesh size over various polymer-rich and polymer-lean regions within the gel may result in an average mesh size that is similar to that measured in a macroscopically-averaged measurement such as swelling. However, given the number of assumptions in the modeling of both experiments, it is likely that such a result in the present study is merely coincidental.

In contrast to the large-scale heterogeneous structure, we find that m depends significantly on the presence of AM co-monomers within the hydrogel. For the PEGDA homopolymer gels, m~1.6-1.8, indicating that the polymer exhibits behavior characteristic of flexible chains in a good solvent, as expected for PEG in aqueous solution.[109] By contrast, m~1.3-1.4 for the PEGDA-co-AM co-polymer gels. This value of m is significantly outside the range of $5/3 < m < 2$ expected for flexible chains in a good solvent, and in the range of $1 < m < 1.5$ expected for semi-flexible chains. Although the source of such behavior is unclear, one possible explanation is a change in stiffness of the acrylic backbone chains upon co-polymerization of the bulky AM co-monomers, resulting in an overall decrease in flexibility of the polymer at length scales less than the mesh size.

5.3.2. Strength of Polymer-Solute Interactions

The strength of intermolecular interactions between the PEGDA-co-AM polymer network and the molecule to crystallize was characterized with the solute equilibrium partition coefficient at the same condition as used in the crystallization study. Solute partition coefficient $\varkappa$, defined as the ratio of solute mass fraction in solution confined in the gel to that in the bulk, is a relevant parameter because it informs the solute concentration in the gel at the crystallization condition, which is an important factor affecting nucleation. Shown in Figure 5-4a, $\varkappa$ of ASA increased by 60% on average after introducing AM into the PEGDA gel, and the ASA concentration in the PEGDA-co-AM gels reached as high as six times as that in the bulk solution. This result indicates much stronger interactions between ASA and the polymer matrix after functionalization. It is also worth noting that before chemical modification, $\varkappa$ climbed from 3.4 to around 4.2 with the increase of M_n, the PEG molecular weight of the PEGDA monomer, while after modification, $\varkappa$ became insensitive to M_n. This observation suggests that ASA mainly interacts with AM segments of PEGDA-co-AM polymer in the solution environment, for reasons discussed as following. The PEGDA polymers are comprised of the PEG subchain and the acrylate crosslinkers. As M_n increases, the mass ratio of PEG to acrylate increases, so does $\varkappa$ in the case of PEGDA system, indicating that ASA primarily associates with the PEG subchain. This inference is further supported by the fact that the molar ratio of ethylene oxide units in PEG to ASA remained constant (7.7) for all mesh sizes, calculated from the partition experiments. In the case of PEGDA-co-AM, the mass fraction of AM doesn't change with M_n, and correspondingly, $\varkappa$ also turned invariant yielding a constant AM to ASA molar ratio of around unity. This result provides strong evidence that ASA prefers to interact with AM than with PEG or acrylate groups constituting the polymer gel.

The ASA-polymer interactions were further quantified with the solute adsorption enthalpy via Isothermal Titration Calormetry (ITC), which also helps to deepen the understanding of partitioning effect. Figure 5-5 shows the results of ITC measurements, where the enthalpy of interaction between ASA and both $PEG_{400}DA$ and $PEG_{400}DA$-co-AM microgels is plotted versus the equilibrium concentration of ASA. The data are presented both as instantaneous enthalpies at a given concentration, $\Delta H_{ASA-gel}$ (top), and as cumulative enthalpies up to a certain concentration, $\Delta H^{tot}_{ASA-gel}$ (bottom). At low ASA concentrations, $\Delta H_{ASA-gel}$ exhibits a plateau for both PEGDA and PEGDA-co-AM gels. After titration of ASA to a concentration of 10 mM or greater, $\Delta H_{ASA-gel}$ decreases monotonically, approaching zero at large ASA concentrations. This behavior suggests that the mechanism of ASA-polymer interactions is by adsorption of ASA onto the polymer network. This is particularly apparent when examining the cumulative interaction enthalpy, $\Delta H^{tot}_{ASA-gel}$, which exhibits the qualitative features of an adsorption isotherm, such that $\Delta H^{tot}_{ASA-gel}$ is related to the equilibrium surface coverage of ASA on the polymer hydrogel. At low concentrations, the increase of $\Delta H^{tot}_{ASA-gel}$ with ASA concentration is roughly linear, corresponding to ideal adsorption of ASA where a majority of the injected solute molecules adsorb to the surface. However, at sufficiently large ASA concentrations, $\Delta H^{tot}_{ASA-gel}$ tends toward a plateau value, suggesting saturation of the hydrogel surface due to monolayer coverage of ASA. Attempts to fit simple, one-site adsorption isotherms to the data in Figure 5 were unsuccessful, most likely due to the complicated structure and chemistry of the hydrogel surface. Nevertheless, the considerable range of concentration over which $\Delta H^{tot}_{ASA-gel}$ increases linearly with ASA concentration allows for calculation of the enthalpy of adsorption of ASA at

infinite dilution, $\Delta H^{\infty}_{ASA-gel}$ by averaging $\Delta H_{ASA-gel}$ over ASA concentrations in the plateau region (Figure 5-5), resulting in $\Delta H^{\infty}_{ASA-gel}$ = -9.8 kcal/mol for $PEG_{400}DA$ and $\Delta H^{\infty}_{ASA-gel}$ = -12.3 kcal/mol for $PEG_{400}DA$-co-AM. This confirms that ASA-polymer interactions are significantly more favorable for PEGDA-co-AM hydrogels compared to PEGDA hydrogels, and further suggests that the presence of the AM co-monomer significantly enhances adsorption of ASA.

Compared with the ASA system, the ACM-polymer interactions turned out to be much weaker in both the microgels (Figure 5-4b), indicated from lower $\varkappa$ values. A marginal increase in $\varkappa$ was seen with modified gels, ranging from 35% (M_n= 130 g/mol) to 14% (M_n= 700 g/mol). Similar to ASA, ACM partitioned to a similar extent into the modified gel of all mesh sizes, whereas in unmodified gels, $\varkappa$ exhibited more apparent variation as a function of M_n. This result may also imply that ACM interacts stronger with AM than with PEGDA. Comparing the ASA to ACM systems, it is not obvious why ASA interacts stronger with both the polymers than ACM. Following the chemical intuition, one would expect the reverse since the ACM molecule carries more hydrogen-bond donors, and both PEGDA and AM are rich in hydrogen-bond acceptors. Complimentary functional group interactions, commonly solicited for interpreting the substrate effect on nucleation from solution, fails to explain our observations, because this approach does not account for the fact that both the polymer and the solute are well solvated. Increased cost of de-solvation required for ACM adsorption onto the polymer may have led to its decreased partitioning, since solute-solvent interactions are stronger for ACM than for ASA indicated by higher ACM solubility in 38/62 (v/v) ethanol/water mixture (90mg/ml at 25°C) than that of ASA (32mg/ml at 25°C).

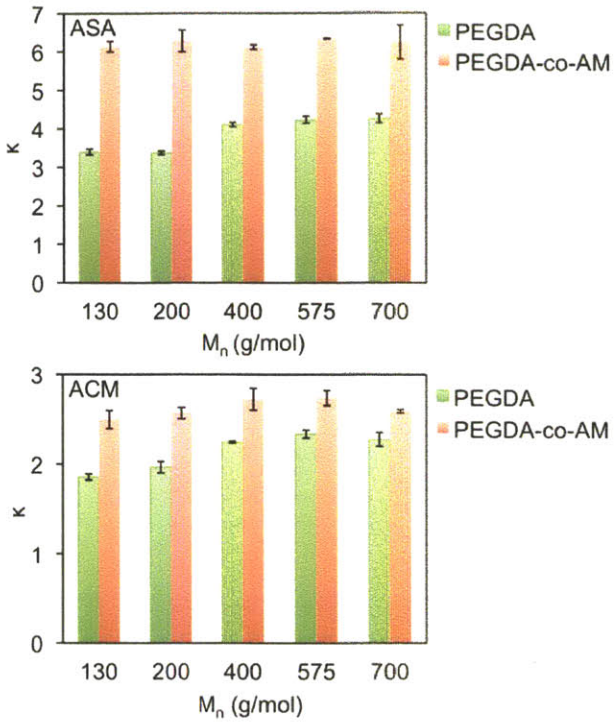

Figure 5-4. Comparison of partition coefficient, κ, in the PEGDA gels vs. PEGDA-co-AM gels for ASA (top) and ACM (bottom) systems. κ is defined as the ratio of solute mass fraction in solution confined in the gel to that in the bulk. The error bars are calculated from three to four independent repeats.

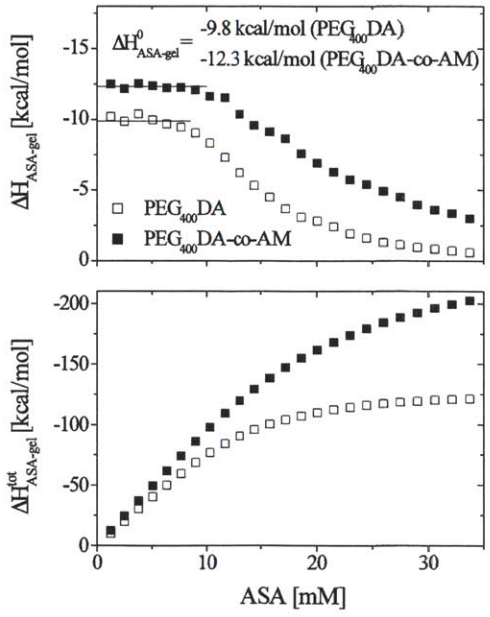

Figure 5-5. Enthalpy isotherms for adsorption of ASA onto $PEG_{400}DA$ (open symbols) and $PEG_{400}DA$-co-AM (closed symbols) microgels, including instantaneous (top) and cumulative (bottom) enthalpies of adsorption. Straight line gives fit to obtain the infinite dilution enthalpy of adsorption. Solid lines show the region over which the infinite dilution enthalpy of adsorption was calculated.

5.3.3. Effect of Gel Chemical Modification on Nucleation Kinetics

To evaluate the impact of polymer-solute interactions on nucleation kinetics, induction times of ASA and ACM were measured with microgels of a series average mesh sizes before and after chemical modification suspended in respective supersaturated solutions. The volume fraction of microgels in the solution is so small ($\sim 10^{-5}$) that the solute partitioning in the gels does not affect the bulk concentration. For each system, a large number of experiments (50-100) were conducted to obtain the induction time probability distribution. Ideally, the nucleation induction time should follow the Poisson distribution, verified in Chapter 2.[80] However, deviations can occur, as discussed in Chapter 4 and in this chapter, when there is more than one type of nucleation sites in a sample, giving rise to multiple Poisson processes with different characteristic time scales. For samples with PEG_MDA microgels, the nucleation induction time distributions reported in Chapter 4 can be faithfully described by stretched exponentials (Table 4-2, Table 4-3), $P=\exp[-(t/\tau)^{\beta}]$, where P is the probability to observe no crystallization event within time t, τ the average induction time.

Modification of PEGDA microgels with AM resulted in much faster nucleation kinetics of ASA overall. The nucleation induction time distributions were better described by two-exponential models (Table 5-2, Figure 5-6) instead of the stretched exponentials obtained with PEGDA microgels. Two exponential processes yielded two distinct time scales, τ_1 and τ_2, with τ_1 an order of magnitude faster than τ_2. Both the two exponential processes were much faster than those obtained with PEGDA microgels, supporting our hypothesis that strong polymer-solute interactions lead to overall success of polymer gels in promoting nucleation. Two time scales possibly result from the presence of two dominant types of active nucleation sites on PEGDA-co-AM microgels. Recalling the hypothesized polymer microstructure as determined by SANS

(Figure 5-3), it is likely that the segregation of AM functional monomers into regions of high local acrylate density results in two largely different types of active sites for nucleation. One type, in the acrylate-lean (and thus AM-lean) regions of the gel, will be such that interactions between the solute and PEG subchain will dominate the nucleation process. The other, in the acrylate and AM-rich regions of the gel, will be such that interactions between the solute and AM will dominate the nucleation process. The latter AM-rich domains may serve as the more active nucleation sites due to favorable solute-AM interactions (as characterized by higher partition coefficient and adsorption enthalpy), which correspond to the shorter average induction time of ASA, and the vise-versa for the AM-lean domains. This interpretation is also consistent with the observation that the shorter time scale τ_1 is much less sensitive to the variation in the PEG molecular weight M than τ_2, the longer time scale (Table 5-2), since the AM-rich domain should be less affected by variation in the PEG subchain length than the AM-lean domain. In the case of PEGDA microgels, although there also exists structural heterogeneity due to microphase separation between acrylate-rich and acrylate-lean domains, such dramatic split of nucleation times scales was not observed, probably because only the acrylate-lean domains are nucleation active given that ASA mainly interacts with the PEG subchain in PEGDA, as discussed earlier.

Similarly, nucleation of ACM in the presence of PEGDA-co-AM microgels split into two exponential processes as well (Table 5-3), probably for the same reasons discussed above. In contrast to the observations from ASA systems, the slower time scale τ_2, possibly associated with the PEG rich, AM lean nucleation sites, was not reduced from those obtained with PEGDA microgels, although the faster time scale τ_1 was shortened by at least an order of magnitude as in the case of ASA. This observation indicates that modification of PEGDA with AM promoted nucleation of ACM in terms of the overall effect, however, to a lesser extent compared with the

ASA system. The data also suggest that the AM-rich nucleation sites are much more active than the AM-lean ones, evidenced by the two orders of magnitude difference between τ_1 and τ_2. However, such difference is not reflected in the partitioning results, where no significant improvement in the partition coefficients was seen after chemical modification. Others factors such as the templating effect may play a more important role in this case, which are discussed later.

Table 5-2. Average nucleation induction times of ASA with the presence of PEGDA-co-AM microgels.

M (g/mol)	130	200	400	575	700
τ_1 (min)	170	21	39	51	33
τ_2 (min)	4900	99	400	470	720
a	0.52	0.05	0.62	0.79	0.68
R^2	0.98	0.99	0.99	0.99	0.99

Bulk solution is at the same crystallization condition as that with PEGDA microgels. Induction time distribution data were fitted with two exponentials via nonlinear least square regression: $P=a\times\exp(-t/\tau_1)+(1-a)\times\exp(-t/\tau_2)$.

Table 5-3. Average nucleation induction times of ACM with the presence of PEGDA-co-AM microgels.

M (g/mol)	130	200	400
τ_1 (min)	55	88	70
τ_2 (min)	1360	12400	35000
a	0.23	0.36	0.29
R^2	0.91	0.96	0.97

Bulk solution is at the same crystallization condition as that with PEGDA microgels. Induction time distribution data were fitted with two exponentials via nonlinear least square regression: $P=a\times\exp(-t/\tau1)+(1-a)\times\exp(-t/\tau2)$. The results from bulk samples and PEG700DA microgels were the same as in Table 4-3.

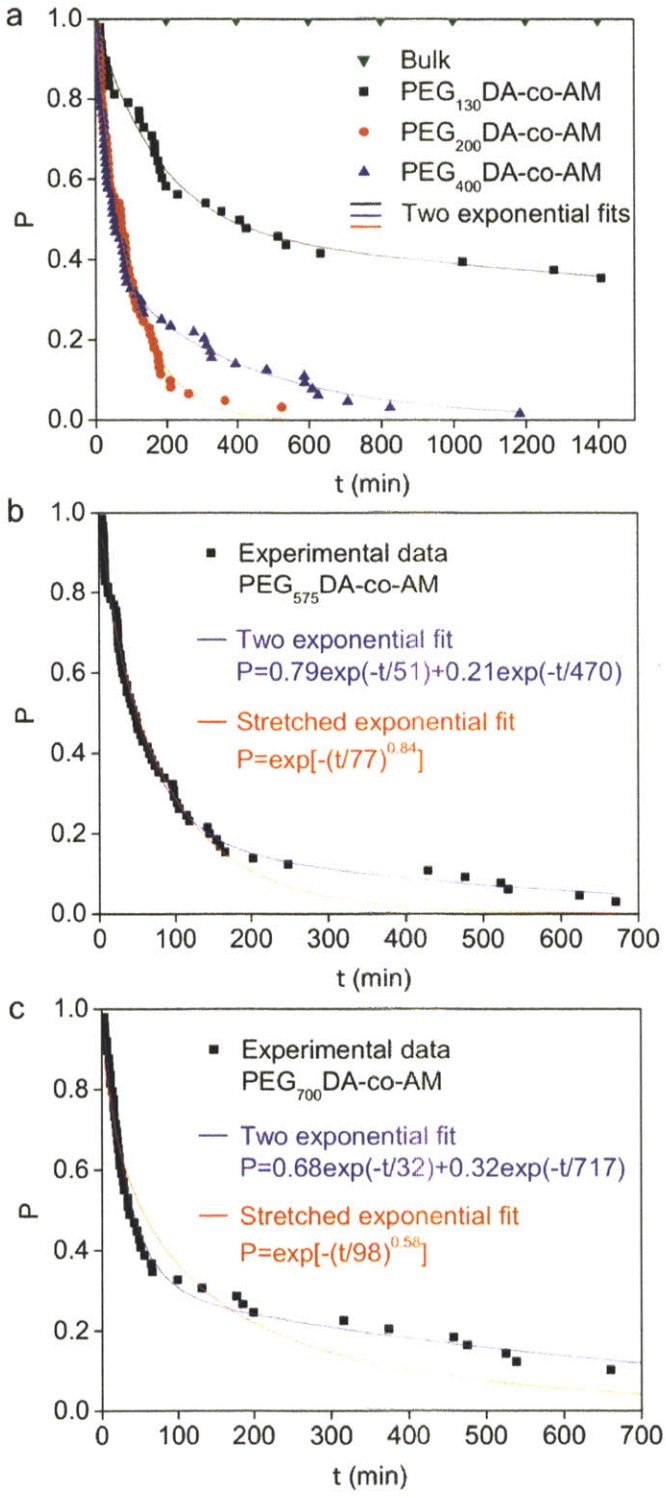

Figure 5-6. Effect of PEGDA-co-AM microgels on nucleation induction time statistics of ASA. P is the probability for no nucleation event to occur within time t. a) Effect of polymer mesh sizes on nucleation kinetics. Fitted parameters following the two-exponential model are listed in Table 5-2. Data for M_n= 575 and 700 g/mol are shown separately for clarity. b) and c) Comparison of two exponential vs. stretched exponential models using PEG_{575}DA-co-AM (b) and PEG_{700}DA-co-AM (c) as representative examples.

Several effects may have contributed to the observed enhancement in nucleation kinetics with chemically modified polymer gels. First, preferential partitioning increases solute concentration in the gel. Particularly, given the adsorptive partitioning mechanism discussed earlier, the solute molecules are likely to be enriched around the polymer matrix. The resultant increase in local concentration may enhance effective solute-solute interactions. It is natural to deduce that higher solute concentration leads to higher supersaturation in the gel, and hence larger driving force for nucleation. However, it is not true in our case for reasons discussed below. Supersaturation (S) is defined by the chemical potential difference ($\Delta\mu$) in relationship $\Delta\mu=\mu_s-\mu_c=kT\ln S$, where μ_s and μ_c are chemical potentials of solute in the solution or gel phase and in the crystal phase. Since the gel and the solution are at equilibrium, the solute molecules possess the same chemical potential in the two phases, and therefore the supersaturation is not different in the gel from that in solution. Although the thermodynamic driving force is not increased due to the presence of the polymer, the polymer may still serve as a 'catalyst', which reduces the kinetic barrier to nucleation by concentrating the solute molecules to facilitate molecular cluster formation. PEGDA-co-AM gels were much more effective than PEGDA in promoting ASA nucleation, which can be partially credited to higher average solute concentration in the gel (Figure 5-4), especially considering that the concentration in local domains may be even higher due to chemical heterogeneity of the gel, as discussed earlier. As for the ACM system, the average solute concentration increased only marginally in the modified gel (Figure 5-4b), and as such its contribution to overall nucleation expedition is less significant than in the case of ASA. However, it is still remarkable that by incorporating AM into the PEGDA matrix, a fast nucleation process was created with average induction times orders of magnitude shorter than those obtained with PEGDA alone (Table 5-3). It is hard to explain this phenomenon with solely

the concentration effect, since even though the chemical heterogeneity polarizes the solute concentration between the AM-rich and AM-lean segments, the extent of concentration polarization should be small, based on the fact that the partitioning coefficient didn't increase much after replacing 50 v% of PEGDA with AM. Other contributing factors may include the difference in specific polymer-solute interactions (templating effect), or the nanoscale structural heterogeneity of the polymer gel. Here, we investigated the templating effect by studying preferred crystal orientation on PEGDA and PEGDA-co-AM polymer films via X-ray diffraction.

5.3.4. Nucleation-Templating Effect of the Polymer Gel

The templating effect may affect crystal nucleation by aligning the solute molecules along the polymer chain via specific polymer-solute interactions. To realistically capture specific polymer-solute interactions in a solvent environment, we chose to determine the crystal facets preferentially grown from a polymer surface in the solvent of interest and infer the complimentary functional group interactions by inspecting the molecular structures of surfaces in contact. Smooth and flat polymer films were prepared following the same formulation as used in the microgel synthesis, except that no porogen and solvent were added to the pre-polymer mixture so as to minimize the variation in polymer mesh sizes, allowing us to focus on the polymer chemistry effect.

Shown in Figure 5-7a, PEGDA films preferentially templated the growth of (002) plane of ASA, and PEGDA-co-AM the (011) plane, judging from the relative peak intensities in the XRD patterns compared with those of the bulk crystals. This result was verified by the observations under the optical microscope that ASA crystals with elongated plate-like shapes lay on their sides on the PEGDA surface via the (002) planes (Figure 5-7d, e), and stood tilted on the

PEGDA-co-AM film via the (011) plane (Figure 5-7c). Comparing the molecular structures of (002) and (011) planes, it can be deduced that the methyl and phenyl groups of ASA (colored blue in Figure 5-7h) dominating the (002) plane mainly interact with the PEGDA polymer, and the carboxyl group (colored red in Figure 5-7h) characteristic of the (011) plane is responsible for interacting with the AM segments of PEGDA-co-AM. Such complimentary interactions between PEGDA and ASA are possible, because the phenyl and methyl hydrogens of ASA, being next to electron-withdrawing groups, have increased tendency to interact with the oxygen of PEGDA. This type of C-H···O interactions, though much weaker than primary hydrogen bonding, is found be abundant in many crystal systems,[110] such as the aspirin crystal in which the methyl hydrogen interacts with the carbonyl oxygen in the ester group to form a dimer-like supermolecular synthon. However, one might expect that the carboxyl group of ASA should primarily interact with PEGDA via hydrogen bonding instead of phenyl and methyl groups. This scenario is not observed probably because the ASA carboxyl group is well solvated by ethanol and water, and as such its interaction with PEGDA is hindered. Compared with PEGDA, the AM segments in the PEGDA-co-AM polymer carry higher density of stronger hydrogen bond acceptors in amide moieties, which may be more effective in completing with ethanol and water to form hydrogen bonds with ASA carboxyl groups. To summarize, the observed preferred crystal orientation induced by specific polymer-solute interactions provides strong evidence for the templating effect of the polymer film on nucleation. ASA interacts with PEGDA via weak C-H···O interactions, whereas its interaction with PEGDA-co-AM is much stronger, possibly via hydrogen bonds formed between ASA and AM. This result is consistent with the observed higher ASA partitioning in PEGDA-co-AM, and stronger binding between the two as measured by the ASA adsorption enthalpy on the polymer. Given stronger interactions with one end of the

ASA molecule, AM is supposed to be more effective in aligning ASA molecules along the polymer chain, and thereby lowers the entropic penalty during nucleus formation, leading to further shortened induction times.

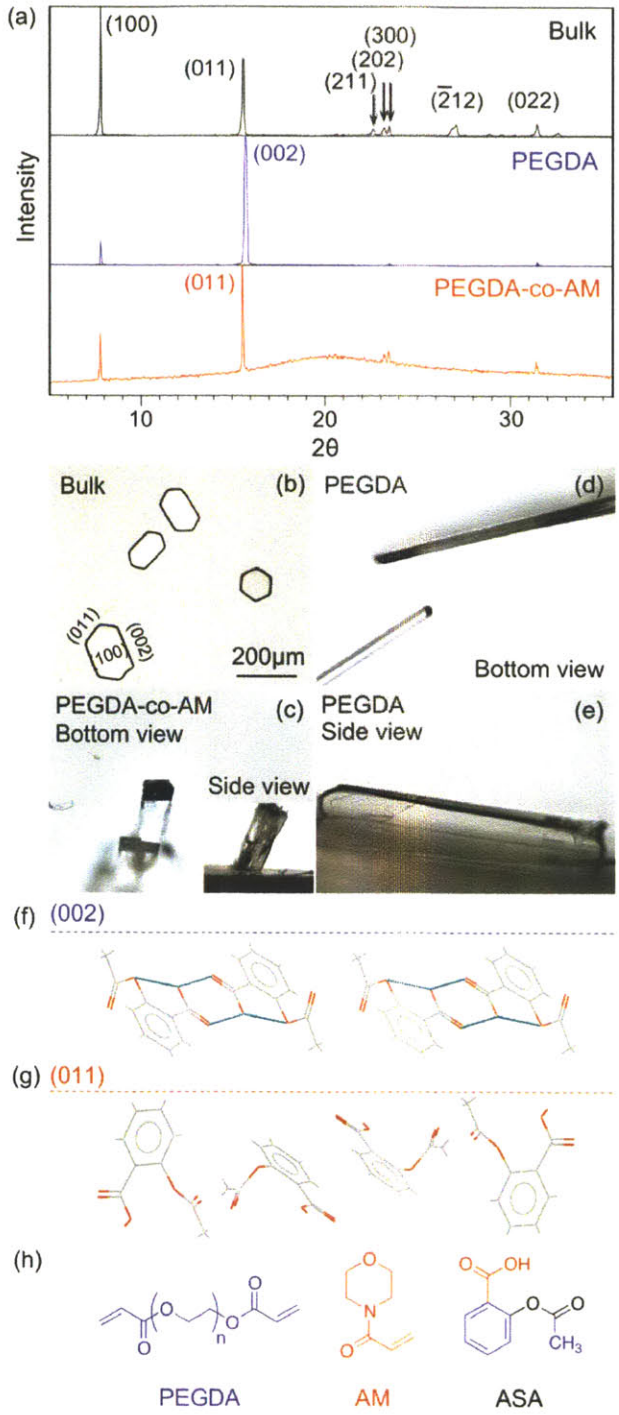

Figure 5-7. Preferred orientation of ASA crystals on polymer films. (a) Comparison of XRD patterns of ASA crystals grew from PEGDA and PEGDA-co-AM polymer films to that of bulk crystals. The results are not

sensitive to variation in M_n and representative patterns are shown. (002) peak is separated from the (011) peak by a 2θ angle of 0.17 degree (calculated from Cambridge Structure Database). The two peaks can be unambiguously identified given that the resolution of XRD measurement is 0.02°. (b-e) Optical images of ASA crystals nucleated from bulk (b), the PEGDA-co-AM surface (c), and the PEGDA surface (d-e). Scale bar is the same for all images. (f-g) Molecular structures of (002) and (011) facets of ASA crystal. The dotted line indicates the top surface of the corresponding facet. (h) Molecular structures of monomers of PEGDA, AM and ASA. ASA functional groups colored blue are inferred to preferentially interact with PEGDA, and those colored red with AM.

Similarly, preferred orientation of ACM crystals on polymer films was also observed, which further verifies the existence of templating effect imposed by the polymer network. XRD study showed that PEGDA induced growth of (011) and its higher index plane (022) almost exclusively, while PEGDA-co-AM preferentially templated $(10\bar{1})$ and its higher index plane $(20\bar{2})$ as well as $(11\bar{1})$ (Figure 5-8a). It is evident from the optical images (Figure 5-8 b-e) that the prism-shaped ACM crystals exhibited random orientations when crystallized from bulk, and seemed to assume certain through-plane orientations when nucleated on the respective films, judging from similar crystal morphology from the top view. Seen from molecular structures of templated crystal facets (Figure 5-8 f-h), all planes present phenolic hydroxyl groups to the surface, on the other hand, $(10\bar{1})$ and $(11\bar{1})$ planes are different in chemistry from (011) in that they better expose the amide group, although the difference is not as apparent as that between (002) and (011) of ASA. Such difference implies that after introducing AM into the PEGDA network, the polymer strengthens its interactions with ACM by forming hydrogen bonds with the amide group of ACM, in addition to with the phenolic hydroxyl group. These observations can help explain the moderate increase in partition coefficients after gel modification. Interestingly, both the amide and phenolic hydroxyl groups that AM preferentially interacts with are also critical for forming the ACM crystal structure (Form I), which is essentially a network of intermolecular hydrogen bonding between the two groups. This may suggest that, with the ability to hydrogen bond with both the groups in the solvent of interest, the AM segment could act like a 'catalyst' for crystal nucleation by facilitating hydrogen bond formation among the aligned ACM

molecules, and lead to a fast nucleation process observed in the induction time study with modified gels (Table 5-3).

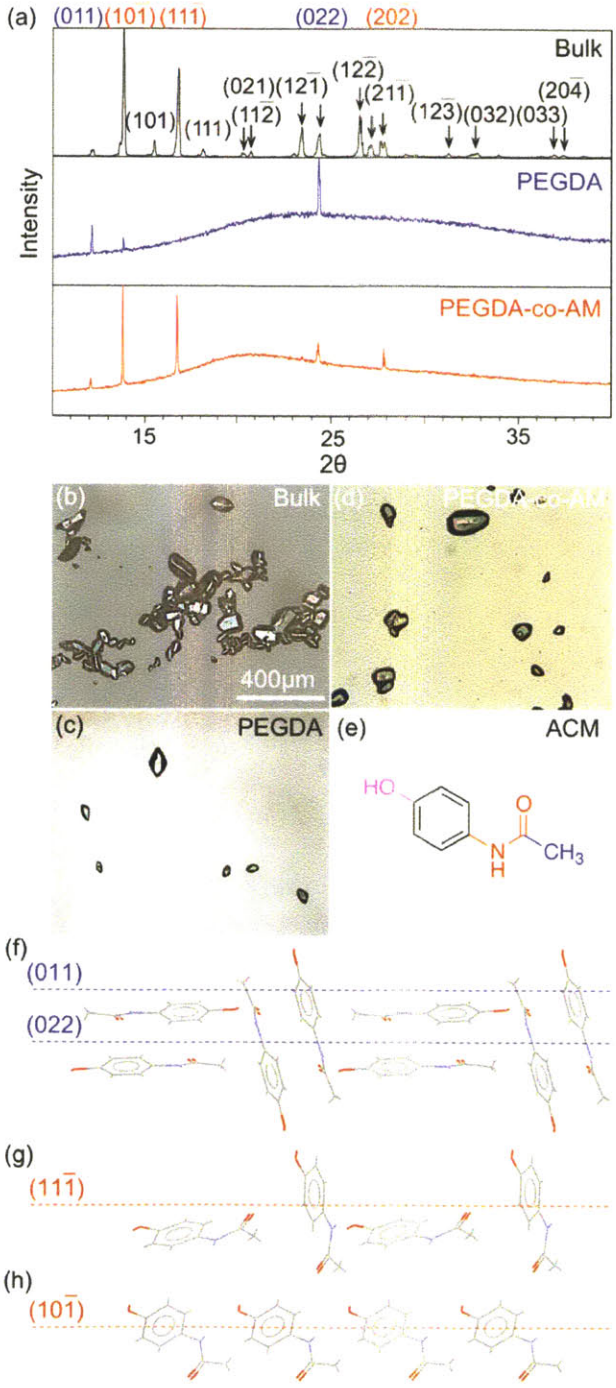

Figure 5-8. Preferred orientation of ACM crystals on polymer films. (a) Comparison of XRD patterns of ACM crystals grew from PEGDA and PEGDA-co-AM polymer films to that of bulk crystals. All ACM crystals are form I, the monoclinic form. The miller indexes (hkl) of facets preferentially oriented parallel to the polymer surface were colored blue and red, corresponding to PEGDA and PEGDA-co-AM polymer films, respectively. (b-d) Optical images of ACM crystals nucleated from bulk (b), the PEGDA surface (c), and the

PEGDA-co-AM surface (d). Scale bar is the same for all images. (e) ACM molecular structure. The functional group colored blue is inferred to preferentially interact with PEGDA, and those colored red with AM. The one colored purple interacts with both PEGDA and AM. (f-h) Molecular structures of (011), (022), (11 $\bar{1}$) and (10 $\bar{1}$) facets of ASA crystal. Above the dotted line is the top surface of the corresponding facet.

5.4. Conclusions

We have demonstrated the essential role of polymer-solute interactions in controlling solute nucleation by tuning the chemical composition of the polymer microgels used for inducing nucleation. When AM co-monomer was introduced into the PEGDA matrix via co-polymerization, ASA nucleation kinetics was promoted by up to four orders of magnitude, while nucleation of ACM was also enhanced by up to two orders of magnitude. Comparing the ASA and ACM systems, the extent of nucleation acceleration generally correlates with the strength of polymer-solute interactions as characterized by solute partition coefficients and adsorption enthalpy. The effect of polymer-solute interactions on nucleation further manifested in the split of nucleation time scales due to the presence of nucleation sites of distinct chemical compositions in the microgels, inferred from SANS data. We further propose that favorable polymer-solute interactions promote nucleation by two means. First, it leads to higher solute concentration in the gel, which enhances the effective solute-solute interactions. Second, specific polymer solute interactions, as evidenced by the preferred crystal orientation on polymers, facilitate molecular alignment along the polymer chain. Our results provide insights into nucleation of molecular crystals at complex interfaces and help set the stage for rational design of 'nucleants' to direct nucleation as desired.

Chapter 6

6. Crystallization of Polymorphs at Confined Interfaces

6.1. Introduction

Controlling polymorphism, the ability of a compound to self-assemble into multiple crystal structures, has been a long-standing challenge in various fields of application.[111] In particular, for pharmaceutical systems, polymorphs often exhibit distinct physical properties, which have profound impact on drug bioavailability, stability, processibility, etc. Both nucleation and crystal growth, two steps constituting a crystallization process, were shown to affect polymorphic outcomes.[112-115] The lack of understanding and control of nucleation, however, remains as a major roadblock in current polymorphism research.[116] One of the most challenging, yet less-explored aspects in controlling nucleation of polymorphs is to decipher the role of interfaces in the nucleation process, since in practice almost all nucleation events occur heterogeneously, a.k.a, at an foreign interface.[3] Designed nucleation substrates can be very useful in controlling polymorphism. For instance, some molecular compounds tend to crystallize in multiple polymorphs concomitantly under the same condition,[117] which could be caused by assorted unknown nucleation sites in the solution. By 'seeding' the solution with designed nucleation 'catalyst' to selectively lower the nucleation barrier of a particular polymorph, heterogeneous nucleation induced by unintended contaminants can be avoided and controlled polymorph nucleation can be achieved.

Several types of substrates have been studied for screening or controlling polymorphs of molecular crystals, including crystalline substrates,[1] 2D ordered surfaces such as self-assembled

monolayers,[40,41,43] and insoluble polymer surfaces.[6] On these flat and smooth substrates, polymorph selectivity seems to be best achieved when both lattice matching (epitaxy) and complimentary chemical interactions at the crystal-substrate interface are satisfied.[43,118] In recent years, materials imposing a nanoscopically confined environment for crystallization have also been explored for polymorph control, such as controlled pore glass with pores ranging from a few to a hundred nanometers,[52,54,71] and microemulsions with drop sizes of 2-10 nanometers.[119,120] Stabilization of metastable polymorphs in nanoconfinement sufficiently small was often observed,[52,54] but not always.[52,120] To explain these observations, evidence was presented that the large surface area to volume ratio can alter the relative polymorph stability.[71] Another hypothesis frequently evoked states that when the pore size becomes smaller than the critical nucleus size of a polymorph, its crystallization was hindered in confinement.[54] However, these arguments fail to account for the nucleation-templating effect of confinement interfaces. Moreover, the kinetic aspect of polymorph control under nanoconfinement has been ignored, which is particularly glaring given the definitive role of nucleation kinetics in affecting polymorphic outcomes.[116] In fact, systematic studies on the kinetics of polymorph nucleation have been scarcely reported in general, not only in the nanoconfinement literature.

In this chapter, we report the use of a novel material, polymer microgels,[80] for understanding and controlling polymorph crystallization of molecular compounds in a confined environment. As discussed in Chapters 4 and 5, the microgels exhibit a mesh-like structure, formed by cross-linking polyethylene glycol diacrylate (PEG_MDA) of various PEG subchain molecular weight M (g/mol). When immersed in solution, the microgel swells by uptaking solute and solvent molecules owing to favorable interactions, and the degree of swelling, which varies as a function of the PEG subchain length, defines its average mesh size, a quantity typically used for

describing the microstructure of the swollen polymer network.[89] With mesh sizes ranging from a few angstroms to several nanometers, the polymer network partitions the absorbed solution and restricts the mobility of adsorbed solute molecules,[80,121] as such providing a confined environment for crystallization to take place.

Using polymer microgels of tunable mesh sizes, we investigate systematically the nanoconfinement effect on polymorphism with two model compounds, carbamazepine (CBZ) and 5-methyl-2-[(2-nitrophenyl)amino]-3-thiophenecarbonitrile (ROY). We find that their polymorphic outcomes are strongly dependent on the polymer mesh size and chemical composition. In addition, there exhibits an evident correlation between the nucleation kinetics and the polymorphic outcome. We examine the underlying mechanism from three aspects, the influence of mesh size, preferential partitioning and specific polymer-solute interactions. We further propose that the selectivity of polymorph nucleation arises from the templating effect driven by specific polymer-solute interactions, which, facilitated with an optimum spatial configuration imposed by the confinement effect, enhances the nucleation of a particular polymorph to the greatest extent.

6.2. Experimental Methods

Materials. Poly(ethylene glycol) diacrylate with average molecular weights of M_n = 200, 400, 575, and 700 g/mol and tri(ethylene glycol) diacrylate (M_n = 130 g/mol), poly(ethylene glycol) with M_n=200 g/mol (PEG_{200}), 2-hydroxy-2-methyl-1-phenyl-propan-1-one (DC1173) photoinitiator, and Tween20 non-ionic surfactant were purchased from Sigma Aldrich Chemical Co. and used as received with no further purification. Deionized water (18.3 MΩ) was obtained using a Millipore MilliQ purification system. For PEGDA microgel pre-cursors, solutions containing 25% PEG_MDA, 25% PEG_{200}, and 5% DC1173 by volume in ethanol were prepared

for each of the values of the molecular weight M_n used. Carbamazepine was purchased from Sigma Aldrich (Form III) and ROY (Form ON) is a gift from Eli Lilly, both used without further purification.

Microgel synthesis and characterization. Methods for PEGDA microgel synthesis and microstructure characterization via swelling measurements were described in detail in previous chapters. In brief, cuboid microgel particles were synthesized by Stop-Flow Lithography (SFL). Microfluidic channels with straight, rectangular cross-sections (width = 300 μm, height = 30 μm) were prepared by Soft Lithography. The inlet channel was loaded with a hydrogel pre-cursor using a pressure-controlled manifold. The mask was placed in the field-stop of the microscope and square features were projected on the pre-cursor by ultraviolet (UV) exposure from a Lumen 200 lamp (Prior) through a wide excitation UV filter set (11000v2: UV, Chroma) when the flow of pre-cursor was stopped. The ultimate feature sizes of the patterned squares were 30 μm x 30 μm, determined through fluorescence imaging of the microchannel during UV illumination. Particles were collected through the outlet channel into a microcentrifuge tube reservoir containing 0.2% v/v Tween20 in a mixture of 62/38 water/ethanol (v/v). Tween20 was added to the outlet reservoir in order to render the microgels colloidally stable during purification. The particles were washed with 62/38 water/ethanol (v/v) for several times to remove unreacted species. The particles were solvent-exchanged into pure ethanol while maintaining the original particle concentration, right before used in crystallization experiments. The apparent average mesh size ξ was estimated using Flory-Rehner theory by measuring the swelling of the polymer microgel in the crystallization media as compared to the as synthesized state.

Nucleation induction time distribution. Crystallization measurements of CBZ from ethanol in the presence of PEGDA microgels of various mesh sizes were conducted in an RS10 Clarity

Station (Thermo Fisher Scientific). We found that CBZ crystallization is quite sensitive to experimental conditions such as solid impurity concentration, solution water content, and stirring speed etc. Specifically, unfiltered, unstirred CBZ-ethanol solution (S=2.8, T=3°C, solution volume V=2ml) tends to yield the stable form III or mixtures of form III and II, whereas the same solution filtered with 0.2μm pore size PTFE filters predominantly crystallizes form II. The presence of trace amount of water in ethanol solution was also observed to inhibit CBZ crystallization. Therefore, absolute, anhydrous ethanol was employed for all crystallization studies to avoid the interference from water. All solutions used in nucleation induction time study were filtered with 0.2μm PTFE syringe filters. All procedures involving exposing solution to the air were conducted under the Bio-Safety Cabinet so as to reduce the chance of contamination with unknown impurities, which would affect induction time results.

Around 1000 microgel particles were dispersed in 2 ml of a 34 mg/ml CBZ solution in anhydrous ethanol, and kept suspended by stirring the solution at 300rpm. Ten such samples were loaded into the Clarity station at once. All samples were heated to 42°C at 5°C/min to erase the thermo history of the solution, which was previously found to affect the nucleation induction time. After kept at 50°C for 30min, the solutions were cooled at 5°C/min to 25°C to generate a supersaturation of 1.63 (defined as the ratio of the starting molar concentration to the saturation molar concentration at the crystallization temperature). This supersaturation level is relative to CBZ Form III. The onset of crystallization was signaled by the sudden drop in IR transmission signal through the solution. The time taken from the moment the desired supersaturation was achieved to the moment the IR signal dropped was taken to be the nucleation induction time. Ten samples were cycled 5 to 10 times between 50°C and 25°C to yield the induction time probability distribution. Towards the end of each heating cycle for dissolving the pre-existing

crystals, the solution was inspected under the optical microscope to make sure the microgels were neither aggregated nor degraded. For ROY, the same procedures were followed with 12mg/ml ROY solutions in anhydrous ethanol. Isothermal crystallization experiments were conducted at 21°C to achieve a supersaturation of around 2.7 with respect to Form R.

For both systems, it is important to eliminate the headspace in the HPCL vial used for crystallization experiments by filling it up with the crystallization solution. This is because, when there is sufficient headspace above the solution, crystals were observed a few millimeters above the solution-glass-air contact line, much before the onset of nucleation in the solution, which may potentially cause unintentional seeding in the solution phase. This phenomenon is probably due to the nucleation from the solution film wetting the glass wall above the solution due to evaporation of the volatile ethanol.

After crystallization, the crystals were collected via filtration for XRD analysis (Panalytical X'pert Pro), and were examined via optical microscopy (Carl Zeiss Axio Observer).

Quantification of the polymorph composition. The polymorph compositions of CBZ crystals were quantified for understanding the concentration effects on the polymorphic outcome. Starting concentrations of 30, 34, 40, 54.2, 80, 120, 141.6 mg/ml of CBZ in anhydrous ethanol were tested in bulk crystallization experiments. All experimental conditions were kept the same as used in CBZ nucleation induction time measurements, except for the starting concentration and the temperature setpoints during the heating cycle for dissolving pre-existing crystals. As soon as crystallization ensued, the CBZ crystals were harvested by passing the slurry through a paper filter, placed in the 0.5mm deep well machined on a zero background plate and subsequently analyzed using PANalytical X'Pert PRO Theta/Theta Powder X-Ray Diffraction System with Cu tube and X'Celerator high-speed detector. Crystalline powders collected in this

manner were analyzed without grinding to avoid polymorph transformation during this process. Though CBZ crystallized as needles, preferred orientation was not a concern even without grinding since the powder mixture was comprised of very fine crystallites due to vigorous stirring during crystallization and that the crystals were collected at the initial stage of crystal growth. All samples analyzed from bulk experiments were mixtures of Form I and II.

The mass fraction of Form I, η, was calculated following

$$\eta = k\frac{I(\theta_{\mathrm{I}})}{I(\theta_{\mathrm{I}}) + I(\theta_{\mathrm{II}})} \tag{1}$$

where I denotes relative peak intensity. θ_{I} and θ_{II} are the characteristic peak positions (2θ in Figure 2) for Forms I and II, respectively. In this case, θ_{I} = 12.345° and θ_{II} = 5.046°, both are the most intense peaks among characteristic peaks of respective phases. Coefficient k is determined experimentally, which converts the peak intensity fraction to the polymorph mass fraction. A calibration curve was made to determine k using CBZ crystal mixtures of known mass fractions of Form I and II. For this purpose, pure Form I and II powders were prepared. Form I crystals were converted by keeping Form III crystals at 150°C in an oven for 4 hours. The crystals were taken out of the oven to enable fast cooling to room temperature, which 'lock' the polymorph in the metastable Form I state. Form II crystals were obtained from solution crystallization induced by minimal amount of PEGDA microgels with M = 400-700 g/mol. Form I and II powders were mixed to yield five samples with Form I mass fractions of 0, 0.20, 0.51, 0.67, 0.75, 1. In the subsequent XRD measurements, the X-ray irradiated length and mask size were set to cover the whole sample area, so that the peak relative intensities thus obtained are not dependent on the mixing uniformity of the Form I and II powders. The linear regression results following Equation (1) yielded k = 1.16, R^2 = 0.98.

Polymorph frequency of occurrence. For the ROY system, the polymorph frequency of occurrence was quantified instead of the polymorphic composition. This is because the ROY crystals we harvested from one sample vial as soon as crystallization was detected by IR were almost always a single polymorph, not a mixture of several polymorphs. This observation was verified via XRD and optical microscopy. To evaluate the ROY concentration effect on the polymorph frequency of occurrence, bulk crystallization experiments were performed at starting ROY concentration of 12, 15, 18 mg/ml, with all other experimental condition kept the same as used in the induction time study. At each starting concentration, 25-50 samples were tested, examined via XRD and optical microscopy. The polymorph frequency of occurrence was calculated as the percentage of samples crystallized in a particular form out of the total number of samples tested.

Partition coefficient measurements. Partition coefficients of CBZ and ROY in PEGDA gels from the bulk solution were determined. A series of gels with varying mesh sizes of approximately 5mm in diameter and 0.5mm in thickness were synthesized via UV polymerization following the same formula as used in the microgel synthesis. The residue solvent, porogen and monomer molecules were removed by washing the gels three times with solvent ethanol, with each wash lasted 12 hours to allow enough time for unreacted species to diffuse out of the gels. The gels were subsequently vacuum dried for 30 minutes and weighed one by one to obtain the dry gel mass. Each dry gel was then immersed in an excess volume (20 ml) of filtered 34mg/ml CBZ-ethanol solution at 25°C for overnight. After equilibrium swelling was reached, the swollen gel was pad dried, weighed and dropped into an excess volume of ethanol (20 ml) to release CBZ. The total mass of CBZ released was determined by measuring its concentration in ethanol after equilibrating for 24 hours, with UV-Vis spectroscopy. The

absorbance at 285nm was recorded for quantitative analysis. The CBZ partition coefficient was calculated as the ratio of CBZ mass fraction in solution absorbed by the gel to that in bulk solution. The partition coefficient of ROY was determined by the same method. The gels were immersed in filtered 12mg/ml ROY solution at 25°C for overnight. The swollen gels were immersed in excessive ethanol to release ROY. Its concentration was determined by measuring the UV absorbance at 397 nm. Three to four independent repeats were carried out for each type of sample to obtain the standard error of the partition coefficient.

Crystal preferred orientation. Polymer films of various PEG molecular weights were synthesized via UV polymerization using pre-polymer mixtures of the same formulations as used for microgel synthesis, but without adding solvent ethanol and porogen PEG200. Thirty microliter of pre-polymer mixture were sandwiched between a glass slide and a quartz slide, both 75mm x 25mm in size. The glass slide was silanized with vinyl trichlorosilane, which co-polymerizes with the monomer to graft the polymer film to the glass substrate via covalent bonds. The quartz slide was used as a template to make polymer films with the minimum surface roughness possible. The sandwiched pre-polymer mixture was subjected to 70 mW/cm^2 UV light for 5min to complete the polymerization, with the whole sample area irradiated fairly uniformly in the 5000-EC UV Curing Flood Lamp (Dymax Corporation). The quartz slide was subsequently lifted to leave the flat and smooth polymer film conformed to the glass substrate. After synthesis, the polymer films were immersed vertically in 20mg/ml CBZ-ethanol solution or 10mg/ml ROY-ethanol solution, which was filtered with a 0.45μm PTFE membrane syringe filter before adding the polymer films. The solution was then sealed, cooled from 25°C to 3°C, and inspected visually every hour. Once crystals were spotted, the polymer film was withdrawn from the solution to terminate crystallization and immediately dipped into a D.I. water tank

vertically to remove loosely attached crystals from the bulk solution (CBZ and ROY are essentially insoluble in water at 3°C). Almost all crystals were found attached to the polymer films conformed to the glass substrate, whereas the back side of the glass had almost none crystals attached. Bulk crystals were obtained under the same conditions and served as the control sample for XRD analysis.

The specific crystal planes grown from the polymer film were analyzed with XRD (PANalytical X'Pert Pro) in the Bragg-Brentano configuration. The polymer film on the glass substrate was mounted horizontally onto the flat stage. A sample area of 20mm x 20mm was irradiated with X-rays in one scan using a programmable divergence slit with 20mm irradiated length and a 20mm mask to ensure enough crystals on the polymer film were sampled to yield the statistically representative preferred orientation. Three scans were performed with one polymer film to cover almost the entire surface area. Since only the diffraction from the crystal plane parallel to the polymer film surface was seen by the X-ray detector, the peak that was significantly more intense relative to that of randomly oriented bulk crystals corresponded to the preferred nucleation face induced by the polymer.

Analysis on the XRD data was carried out by normalizing the measured peak intensities I_{p}^{i} with the reference peak intensities I_{bulk}^{i} from the bulk sample, following the formula

$$\eta_i = \frac{I_{\mathrm{p}}^{i} / I_{\mathrm{bulk}}^{i}}{\sum_{i} (I_{\mathrm{p}}^{i} / I_{\mathrm{bulk}}^{i})} \times 100 \qquad (2)$$

where η_i is the percentage of crystals in orientation i, and p is short for polymer.

6.3. Results and Discussion

6.3.1. Systems

Monodispersed cubelike PEG_MDA microgels (Figure 6-1 left), with M ranging from 130 to 700 g/mol were synthesized by Stop-Flow Lithography,[87] following a procedure described in Chapter 4.[80] Their mesh sizes vary from 0.7 to 1.5 nm in solvent ethanol (Table 6-1), estimated from equilibrium swelling by the Flory-Rehner theory.[80,88] The accuracy of this method for obtaining mesh sizes has been confirmed with Small-Angle Neutron Scattering in a different solvent (Chapter 5).[121] The microgels were utilized for controlling polymorph crystallization by suspending ~ 10 μg of microgels per 1 ml solution by stirring. Such a low microgel concentration is already sufficient to effect drastic change in the crystallization behavior (discussed later), underscoring the effectiveness of polymer microgels in controlling crystallization. In all crystallization experiments, supersaturation of the solution was generated by cooling instead of solvent evaporation, despite its popularity in numerous polymorph studies, to yield better control over the crystallization process.

We selected CBZ and ROY as model compounds to represent both packing polymorphism (CBZ) and conformational polymorphism (ROY), where CBZ polymorphs have the same conformer arranged in differing molecular packing motifs,[122] and ROY, in comparison, assumes distinctive molecular conformations in various packing arrangements, altering its conjugation state and thus the color among different polymorphs.[123] Both molecules have been studied extensively for purposes of polymorph screening[6,41] and control.[54] CBZ possesses 4 known anhydrous forms, and ROY has 10 known forms with 7 structurally characterized. The complexity of the two systems poses challenges for their polymorph control. Specifically, concomitant crystallization (simultaneous crystallization of multiple forms in the same liquid),[117]

has been reported for both the systems.[124-127]. In addition, crystallization of ROY polymorphs also suffers from poor reproducibility,[126] owing to the stochastic nature of its polymorph crystallization.[41]

6.3.2. Crystallization of CBZ Polymorphs Induced by Microgels

Out of the 4 known anhydrous forms of CBZ, namely, Triclinic form I, Trigonal form II, Primitive monoclinic form III and C-centered monoclinic form IV, form III is the most stable under ambient conditions, followed by form I, IV and II, with the energy separation between form III and II less than 0.7 kcal/mol.[122] Such a narrow energy window suggests the sensitivity of CBZ crystallization to experimental parameters. Not surprisingly, there have been some inconsistencies in previous reports on the CBZ polymorphic outcome during crystallization from solution under similar conditions. For instance, when crystallized from highly supersaturated ethanol solution (often with supersaturation $S > 3$) by cooling to low temperatures ($T < 10°C$), Grzesiak et al[122] obtained pure form II; Nokhodchi et al[128] crystallized pure form III; Getsoian et al[129] reported pure form II, but in fact it was a mixture of forms I and II judging from their XRD results. At a lower supersaturation (S=2) and higher temperature (T=25°C), concomitant crystallization of forms II and III was observed by Kelly et al,[124] also from ethanol solution. In this study, we found that CBZ crystallization is indeed quite sensitive to experimental conditions such as solid impurity concentration, solution water content (trace amount), and stirring speed etc, which could explain some of the aforementioned inconsistencies. Therefore, all crystallization conditions were strictly controlled to yield reproducible results.

At the experimental conditions we employed (S=1.63, T=25°C, 2ml purified solution stirred at 300rpm), concomitant crystallization of Forms I and II was consistently observed (~100 trials) when crystallized from the bulk of ethanol solution (Table 6-1, Figure 6-2), both polymorphs

with needle-like crystal habits. Occasionally, pure Form III was also obtained from bulk experiments. The possibility of observing both I and II forms due to solvent-mediated polymorph transformation was eliminated because the polymorphic composition didn't exhibit statically significant change during aging of the crystal mixtures in solution from the onset of nucleation, which were sampled at intervals and characterized by XRD. Interestingly, when PEG_MDA microgels with $M \geq 400$ g/mol were added into the solution, pure Form II was crystallized (~250 trials) as identified by XRD (Figure 6-2), whose needle-shaped crystals were observed to grow from the microgel surface (Figure 6-1 right). However, such polymorph selectivity could not be attained using microgels with $M < 400$ g/mol (~100 trials) where the polymorphic outcome was quite similar to that of the bulk samples (Table 6-1), only with a decreased mass fraction of Form I in the mixture obtained (Figure 6-2, Figure 6-5 discussed later) and a lower frequency of occurrence of Form III.

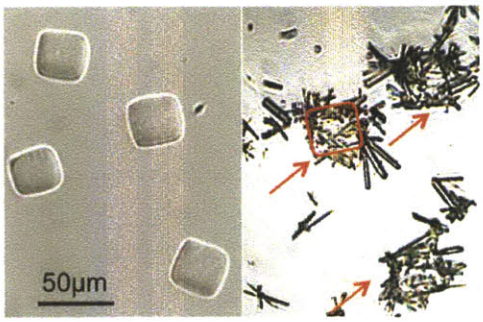

Figure 6-1. Optical micrographs of $PEG_{400}DA$ microgels as synthesized (left) and CBZ form II needles grown on $PEG_{400}DA$ (right), in which three microgels covered with CBZ needles are indicated with red arrows, and the contour of the middle one is traced with red lines to delineate the cubic gel.

Table 6-1. Effect of PEG_MDA microgels on the average nucleation induction times and polymorphic outcomes of CBZ.

M (g/mol)	Bulk	130	200	400	575	700
ξ (nm)	NA	0.7	0.8	1.1	1.3	1.5
Polymorph	II & I, occasionally III	II & I	II & I	II	II	II
τ (min)	427 ± 13	222 ± 5	174 ± 11	10.9 ± 0.3	33 ± 1	49 ± 1

β	0.86	0.99	0.73	1.00	0.61	0.94
R^2	0.986	0.982	0.960	0.976	0.981	0.987

Average mesh size ξ was estimated from equilibrium swelling experiments[80] in solvent ethanol. Polymorphic outcomes were analysized by XRD (Figure 6-2), and corresponding polymorphic compositions were shown in Figure 5. Induction time distribution data were fitted with stretched exponentials via nonlinear least square regression: $P=\exp[-(t/\tau)^{\beta}]$, where P is the probability to observe no crystallization event within time t.

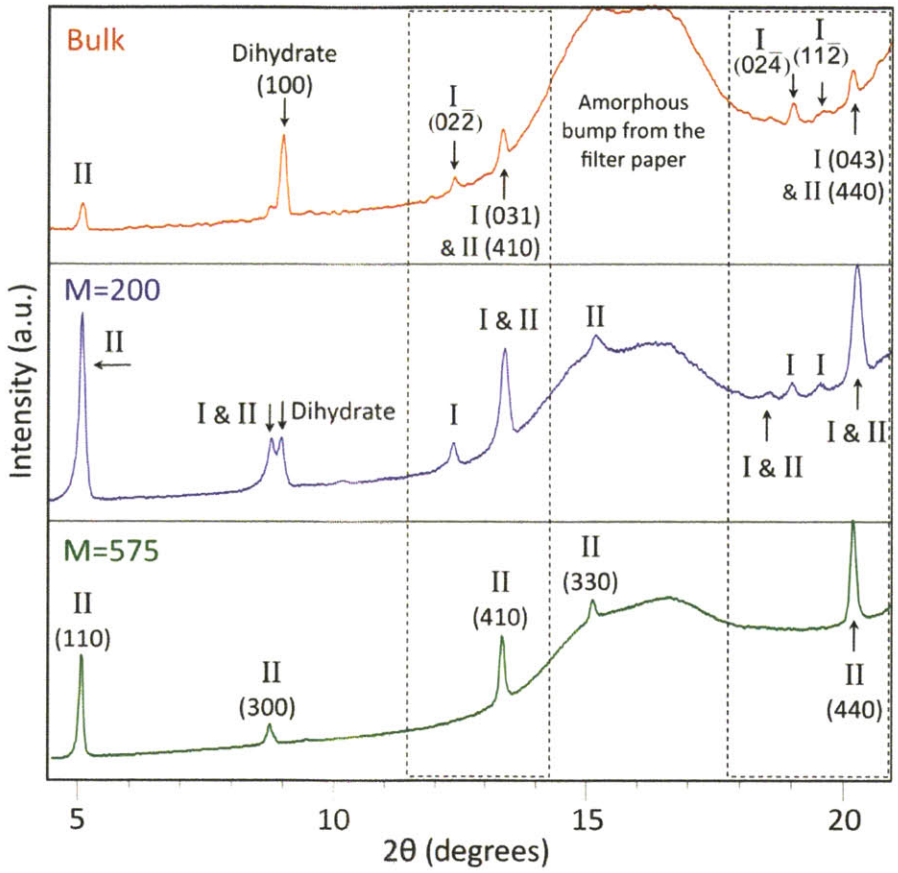

Figure 6-2. X-ray Diffraction patterns of CBZ from bulk solution (top) and in the presence of PEG_MDA microgels, for which representative patterns are shown with M=200 (middle) and 575 (bottom) g/mol. CBZ forms I and II peaks are labeled with miller indexes (hkl) in the top and bottom panels respectively. The regions where major characteristic peaks of form I reside are outlined with black dotted lines. The hump between 12 to 20° is from the filter paper, since the crystals, harvested as soon as the crystallization ensued, are too few to be scraped off form the filter paper. A peak at 9.00° appears in some patterns, corresponding to CBZ dihydrate which forms during filtration, especially when the ambient humidity is high. This explanation is corroborated with control experiments where clear CBZ solution was passed through the filter paper, the XRD scan on which revealed only the dihydrate peak.

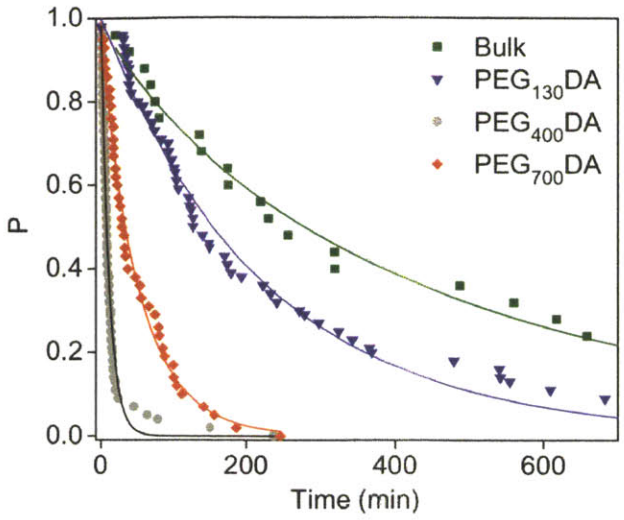

Figure 6-3. Nucleation induction time statistics of CBZ with or without the presence of PEGDA microgels. P is the probability for observing no crystallization event within time t. Stretched exponential model was employed to fit the data (see Table 6-1), and the fitted curve is displayed as solid lines. Data obtained with $PEG_{200}DA$ and $PEG_{575}DA$ are omitted for clarity.

Accompanying the impact on CBZ polymorphic outcomes is the exceptional ability of the microgels in altering the CBZ nucleation kinetics, characterized by the average nucleation induction time τ (Table 6-1). Induction time was measured by monitoring IR transmission signal passing through a solution in controlled temperature environment and stirring condition. Once nucleation occurs, the solution becomes turbid in seconds indicated by a sharp drop of IR signal, due to secondary nucleation and rapid crystal growth. The statistical nature of nucleation necessitates a large number of experiments (50-100) for obtaining the distribution of induction times, from which the average induction time τ is regressed with a stretched-exponential model, $P(t)=\exp[-(t/\tau)^{\beta}]$, where P is the probability to observe no crystallization event within time t. This approach was detailed in Chapter 4.[121] In brief, the stretched-exponential model modifies the single exponential model derived from the Poisson statistics,[77] $P(t)=\exp(-t/\tau)$ by adding an exponent β to the dimensionless induction time t/τ to capture the spread in characteristic time scales caused by a distribution of nucleation active sites present in the system.

Shown in Table 6-1 and Figure 6-3, microgels with M=130 and 200 g/mol effectively shortened the CBZ average induction time by 2-3 fold relative to that of the bulk samples, whereas at least an order of magnitude reduction was observed with microgels of higher M. More importantly, there exhibits a strong correlation between the extent of nucleation acceleration and the polymorph selectivity, wherein Form II was exclusively obtained only with the microgels sufficiently effective in promoting nucleation. Considering that Form II is the least stable polymorph at ambient conditions, this correlation leads us to hypothesize that the observed polymorph selectivity towards a higher energy form may be driven by kinetic factors, in which case, the presence of microgels preferentially lowers the kinetic barrier to Form II nucleation, as opposed to switching the relative stability between Form I and II.

6.3.3. Mechanistic Investigations into CBZ Polymorph Selectivity

The microgels could alter the relative nucleation rates of CBZ polymorphs through various means. First, we investigated the 'concentration effect', based on the knowledge that the microgels have the ability to concentrate solute molecules via favorable polymer-solute interactions.[80] Indeed, equilibrium partitioning experiments revealed that CBZ concentration in the polymer gel is 3-4 times as high as that in the bulk (Figure 6-4). In addition, a generally higher partition coefficient $\varkappa$ in microgels with larger M suggests that CBZ prefers interacting with PEG to acrylate segments. To assess the effect of solute concentration on polymorphic outcomes, bulk crystallization experiments were conducted at a series of starting concentrations and the resultant Form I and II mixtures were analyzed with XRD to quantify the polymorph compositions. Shown in Figure 6-5, increasing solute concentration reduces the Form I mass fraction and thus biases the polymorphic outcome towards the less stable Form II. This trend is not unexpected since in practice less stable forms are typically generated by increasing the

supersaturations to drive the system towards kinetic control regime. However, using this strategy we could not eliminate Form I to obtain pure Form II, even at concentration as high as 140 mg/ml (S=6.7). In fact, when concentration increased beyond 60 mg/ml, the polymorph composition became irreproducible since before the solution was cooled to desired supersaturation level, crystallization already ensued. In contrast, the microgels can take the system into a parameter space inaccessible through conventional means. For samples with microgels, we observed the same trend as did with the bulk samples (Figure 6-5), which indicates higher solute concentration in the gel could faciliate selective nucleation of Form II. Yet, the high degree of selectivity cannot be explained quantitatively with only the concentration effect, which prompted us to examine other contributing factors, such as the nucleation templating effect of the PEGDA polymer.

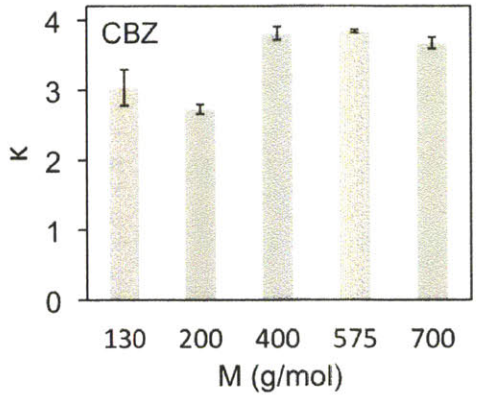

Figure 6-4. Partition coefficients (κ) of CBZ in PEG_MDA microgels from ethanol solutions. κ is defined as the ratio of solute mass fraction in solution confined in the gel to that in the bulk. The error bars are calculated from three to four independent repeats.

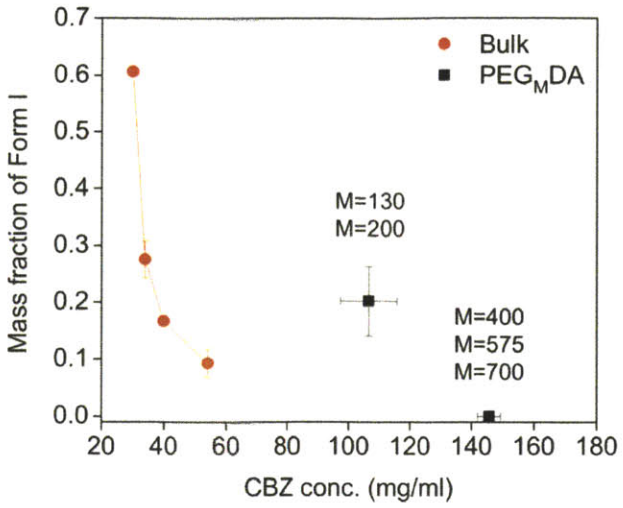

Figure 6-5. Effect of solute concentration on the polymorphic composition of CBZ crystals. For samples with PEG$_M$DA microgels, X-axis corresponds to the effective solute concentration of solution inside the gel, calculated by multiplying the solute partition coefficient (Figure 6-4) with the bulk concentration, 34mg/ml for all samples with microgels. The X error bars are from partition coefficient measurements, and the Y error bars calculated from XRD measurements on three independent samples. The mass fraction of Form I, η, was calculated following $\eta = k\frac{I(\theta_I)}{I(\theta_I)+I(\theta_{II})}$, where I denotes relative peak intensity. θ_I and θ_{II} are the characteristic peak positions (2θ in Figure 6-2) for Forms I and II, respectively. In this case, $\theta_I = 12.345°$ and $\theta_{II} = 5.046°$. Coefficient k, experimentally determined, converts the peak intensity fraction to the polymorph mass fraction.

Besides increasing the solute concentration in the gel, favorable polymer-solute interactions can also induce 'templating effect', by which it directs the CBZ molecules towards a particular orientation via molecular recognition events and thereby reducing the entropic cost during nucleus formation. This microscopic phenomenon should be expressed macroscopically as preferred orientation of crystals on flat polymer surfaces, which can be detected via XRD.[77,121] Expectedly, we observed that the PEGDA polymer surface only induced nucleation of a particular set of crystal planes of Form II, i.e., (110) and its higher index planes, irrespective of the polymer mesh size, or the PEG subchain molecular weight (Figure 6-6a). Specificity as high as such strongly suggests that the templating effect holds key to the microgel-induced polymorph selectivity. To identify the specific polymer-CBZ interaction responsible for directing Form II nucleation, the surface chemistry of II (110) and II (440) were compared against other major

crystal facets not nucleated from the polymer surfaces, namely, II (410), I ($02\bar{2}$) and I ($02\bar{4}$) (Figure 6-2; note that the XRD patterns in Figure 2 were obtained with randomly oriented crystal powders, and therefore capture a statistical average of all crystal facets grown from the system). All II (410), I ($02\bar{2}$) and I ($02\bar{4}$) facets exhibit similar surface chemistries, dominated by the phenyl group on the azepine ring and decorated with carboxamide group (Figure 6-6d; only I ($02\bar{2}$) is shown), which leaves the vinyl group a distinctive functionality characterizing the II (440) facet. This analysis implies that it is the vinyl group of CBZ mainly engaged in its interaction with PEGDA (Figure 6-6e), possibly by forming the C-H···O contact[110] between the CBZ vinylic hydrogen of CBZ and the oxygen of the PEG subchain. Albeit weak, such interactions were found to play an important role in directing nucleation process[43,121] and in distinguishing polymorphs of many organic crystals.[110]

In summary, both the concentration effect and the templating effect are found to contribute to the observed CBZ polymorph selectivity induced by polymer gels. Considering the striking similarity of the intermolecular interactions between Form I and II of CBZ,[122] the polymorph selectivity achieved with the microgels is indeed remarkable. It is also worth noting that the CBZ polymorphic outcomes seem to be quite sensitive to the polymer mesh sizes, with exclusive nucleation of Form II only obtained using microgels of larger mesh sizes, the implication of which is discussed later and summarized as the 'mesh size effect'.

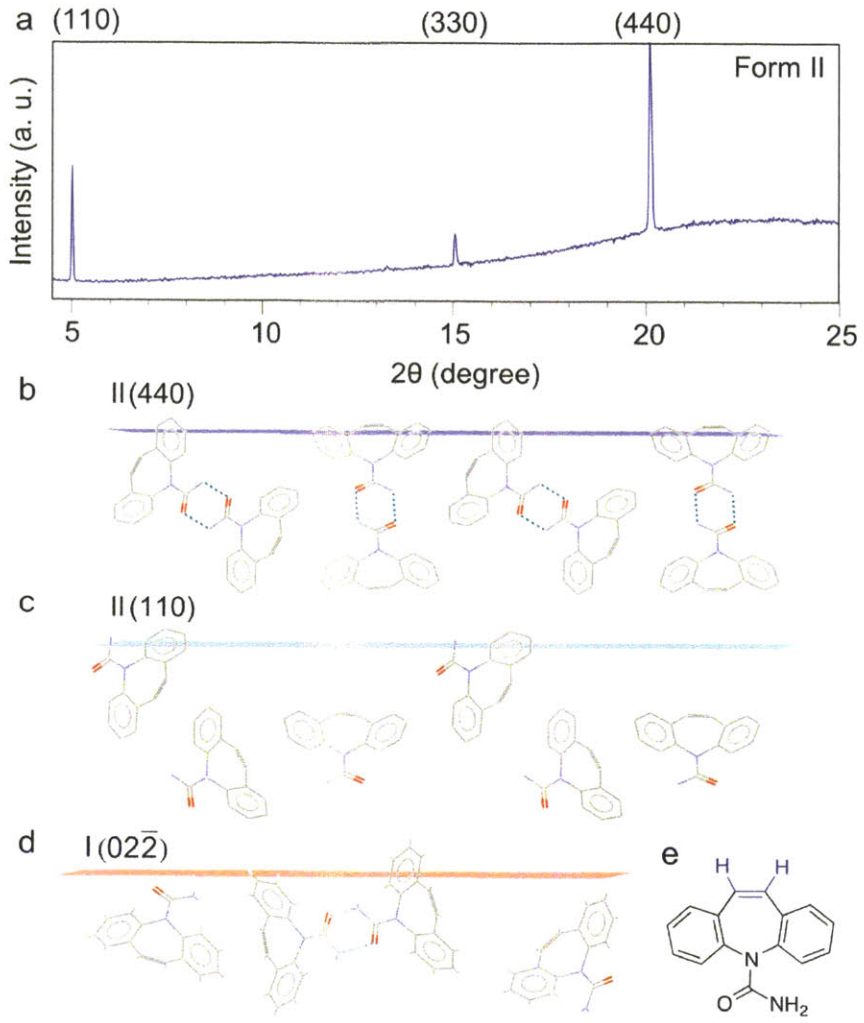

Figure 6-6. Specific CBZ-polymer interactions inferred from preferred crystal orientations. (a) XRD pattern of CBZ crystals grown on PEG_MDA films. Relative peak intensities were found to be independent of M. A representative pattern is shown. (b, c) Surface structures of Form II facets preferentially nucleated on polymer surfaces. (d) Surface structure of a facet characteristic of Form I not grown from polymer surface. (e) Functionality inferred to preferentially interact with PEGDA polymer (colored blue).

6.3.4. Crystallization of ROY Polymorphs Induced by Microgels

ROY crystallization is well known for its poor polymorph selectivity for two reasons. First, when crystallized from solution, multiple polymorphs can be obtained (often in pure forms, occasionally concomitant) from the same solution under seemingly identical condition.[41,126,127] Second, during crystallization from supercooled melt, concomitant polymorphs are frequently observed controlled by both the nucleation and crystal growth kinetics.[114] Here we are interested

in solution crystallization, where the poor selectivity may arise from a broad distribution of molecular conformations in solution, in addition to the small free energy difference between ROY polymorphs as in the case of CBZ.[126]

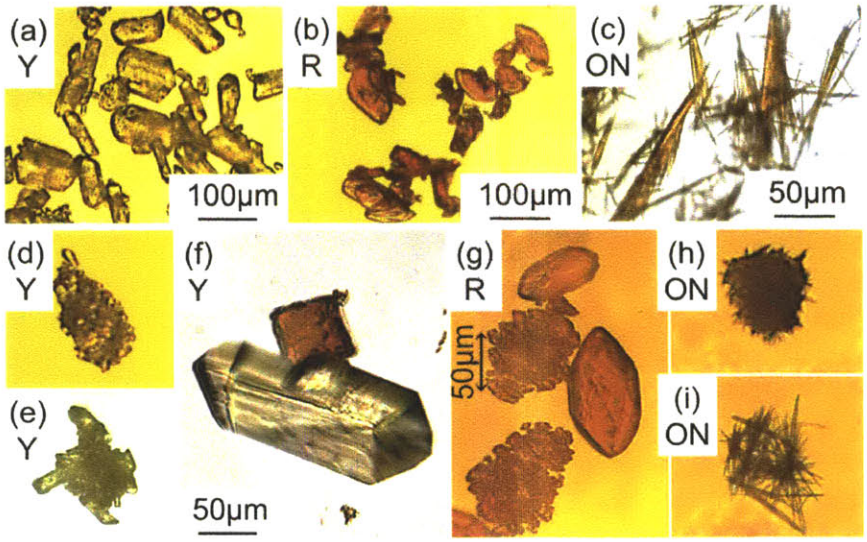

Figure 6-7. Optical micrographs of ROY crystallized from (a-c) bulk and on (d-i) microgels, specifically, with M=400, 575, 700, 400, 400, 400 g/mol in images d, e, f, g, h, i respectively. Y, R and ON denote yellow prism, red prism and orange needle forms. Scale bars for images (d-i) are the same as shown in (f). In images (d, e, g, h, i), the cubic microgels are buried with tiny ROY crystals grown from their surfaces, whereas in image (f), only one large single crystal nucleated on the gel, leaving the red-colored microgel clearly visible. The originally transparent microgel became red in solution due to high preferential partitioning of ROY into the gel (Figure 6-10) or polymer-solute interaction induced conformation change.

In each experiment, we observed crystallization of pure forms of either Y (yellow prisms), R (red prisms) or ON (orange needles) from ethanol solution stochastically (Figure 6-7), and their frequencies of occurrence were calculated by conducting 50-150 experiments in each case (Figure 6-9). Nucleation induction time data from bulk solution or with $PEG_{130}DA$ microgels were fitted with the stretched exponential model and the average induction time thus regressed represents an average of all forms (Figure 6-8a, Table 6-2), since the frequencies of occurrence for R and ON were too low for separate statistical analysis. Low values of stretched exponential exponent β (Table 6-2) indicate a wide spread of nucleation times scales, possibly associated with a broad conformation distribution of ROY in solution since β as low as such has not been observed with systems exhibiting packing polymorphism.[121] Induction time data obtained with

microgels of M=200-700 g/mol can be described very well with multi-exponential models (Figure 6-8, Table 6-3), with each exponential decay process corresponding to each particular form, and its characteristic time scale the average nucleation induction time of each form. In the multi-exponential model, each exponential decay process may be better represented with a stretched exponential, however, a simple exponential suffices in this case and decent fit was obtained with R^2 very close to unity (Table 6-3). This is probably because when the time scales corresponding to different polymorphs are at least an order of magnitude apart, the spread of times scales within each decay process, described by the stretched exponential exponent β, becomes secondary in comparison.

For bulk crystallization without microgels, we observed predominant Form Y at the chosen experimental condition, occasionally Form R and ON (Figure 6-7 a-c, Figure 6-8a, Figure 6-9 left). The relative stability of the three observed polymorphs are Y>ON>R at this condition. Our observation is consistent with previous reports, for instance, Alvarez obtained primarily Y from various supercooled solutions.[130] The addition of microgels had a great impact on ROY nucleation kinetics and polymorph frequency of occurrence, the extent of which varied considerably with the polymer mesh size. Shown in Figure 6-8a and Table 6-2, $PEG_{130}DA$ microgels expedited nucleation of Y form, however, its effect on crystallization of other forms was not very pronounced. When $PEG_{200}DA$ microgels were injected into the ROY solution, nucleation of Y was further accelerated, all of which occurred within 100 min, and Form R also started appearing at a detectable rate. Naturally, the observed promotion of Y and R nucleation kinetics was reflected in increased frequencies of occurrence for both the forms (Figure 6-9 left). With addition of PEGDA gels of larger mesh sizes (Figure 6-8b-d, Table 6-3), Form ON nucleation was accelerated into the detectable range as well, but its average rate was much

slower than those of Forms Y and R in all cases. Meanwhile, nucleation of Form R continued to be promoted, until a maximum was reached with $PEG_{575}DA$ microgels, at which point the average induction time of R was reduced to 200 min from well over 10000 min without microgels. Correspondingly, the frequency of occurrence for R also peaked at M=575 g/mol, replacing Y to become the dominant polymorph (Figure 6-9 left). Evidence of ROY polymorphs nucleated on microgels was shown in Figure 6-7 d-i.

Notably, previous researchers found that the frequency of occurrence of Form R has been quite low compared with Y, ON during solution crystallization from various solvents,[41,127,130] particularly when supersaturation was achieved by cooling as did in this study. Alvarez[130] showed that R polymorph was obtained only once out of 42 experiments despite the use of multiple solvents and cooling rates. Hilden[127] also obtained predominantly Form Y and ON by evaporating ethanol in capillaries. Though other methods have been used for screening rare ROY polymorphs,[6] the reproducibility and selectivity were not reported. In this study, we demonstrate that addition of polymer microgels improved the Form R frequency of occurrence by up to 20 times even at relatively low supersaturation, which is not attainable by conventional means.

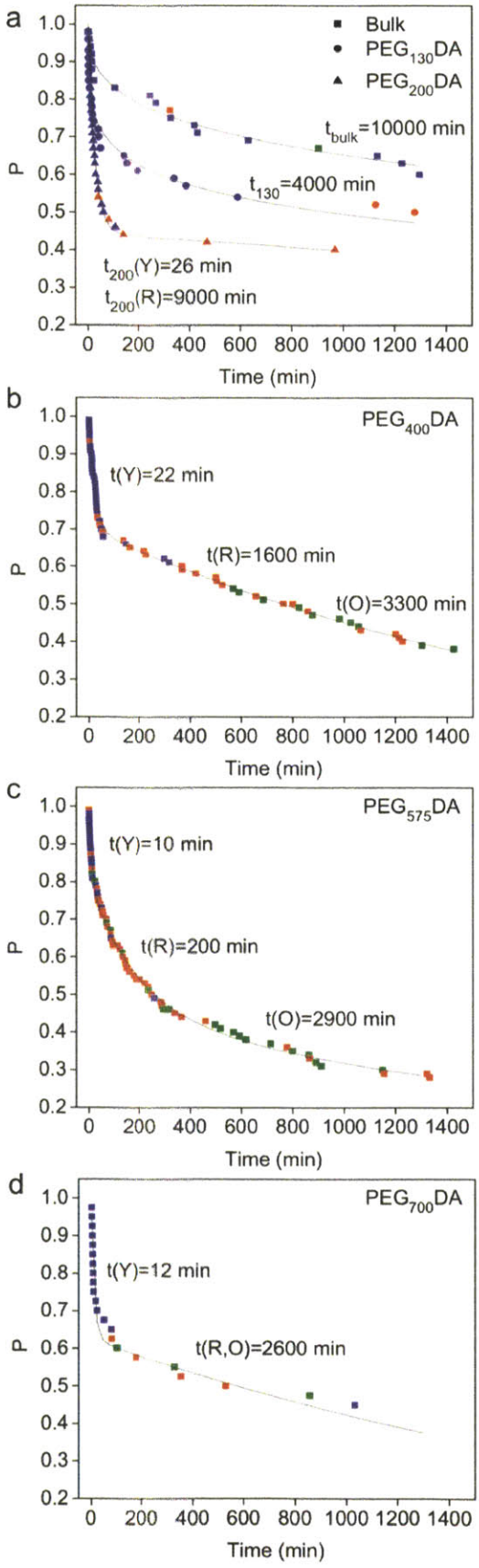
a
Bulk
PEG130DA
PEG200DA
tbulk=10000 min
t130=4000 min
t200(Y)=26 min
t200(R)=9000 min
P
Time (min)
b
PEG400DA
t(Y)=22 min
t(R)=1600 min
t(O)=3300 min
P
Time (min)
c
PEG575DA
t(Y)=10 min
t(R)=200 min
t(O)=2900 min
P
Time (min)
d
PEG700DA
t(Y)=12 min
t(R,O)=2600 min
P
Time (min)

Figure 6-8. Nucleation induction time statistics of ROY with or without the presence of PEGDA microgels. Each data point corresponds to one individual crystallization experiment. A data point is colored blue, red or green if form Y, R or ON is obtained from this experiment. For each type of samples, 50-100 experiments were performed to obtain the induction time statistics. P, the probability for observing no crystallization event within time t is estimated from the fraction of samples haven't crystallized at this time point. Either stretched exponential model or multi-exponential models were employed to fit the data (see Tables 2 and 3), and the fitted curve is displayed as a black solid line. Each exponential decay process was labeled with its characteristic time scale obtained from the model fitting.

Table 6-2. Average nucleation induction times of ROY in bulk and with $PEG_{130}DA$ microgels.

Samples	τ, min	β	R^2
Bulk	10000 ± 2000	0.37 ± 0.02	0.97
$PEG_{130}DA$	4000 ± 750	0.25 ± 0.01	0.97

Induction time distribution data were fitted with stretched exponentials via nonlinear least square regression: $P=\exp[-(t/\tau)^{\beta}]$, where P is the probability to observe no crystallization event within time t. τ is an average of induction times for all Y, R, ON forms.

Table 6-3. Average nucleation induction times of ROY with PEG_MDA microgels, (M = 200-700 g/mol).

Microgels	τ(Y), min	τ(R), min	τ(O), min	a	b	R^2
$PEG_{200}DA$	26.0 ± 1.5	9000 ± 6000	NA	0.550	NA	0.983
$PEG_{400}DA$	22.0 ± 0.6	1600 ± 400	3300 ± 1200	0.298	0.330	0.995
$PEG_{575}DA$	10.0 ± 0.8	200 ± 20	2900 ± 500	0.205	0.350	0.996
$PEG_{700}DA$	12.0 ± 1.2	2600 ± 400*		0.375	NA	0.967

Induction time distribution data were fitted with superposition of two or three exponentials via nonlinear least square regression. Two-exponential fit was employed for $PEG_{200}DA$ and $PEG_{700}DA$ samples: $P=a\cdot\exp[-t/\tau(Y)]+(1-a)\cdot\exp[-t/\tau(R)]$, with τ(R) an average of forms R and O for the $PEG_{700}DA$ sample. Three-exponential fit was used for $PEG_{400}DA$ and $PEG_{575}DA$ samples: $P=a\cdot\exp[-t/\tau(Y)]+b\cdot\exp[-t/\tau(R)]+(1-a-b)\cdot\exp[-t/\tau(O)]$, where Y, R, and O represent the yellow, red and orange needle forms respectively. *τ, an average induction time of Form R and ON, given the lack of data points to distinguish the two.

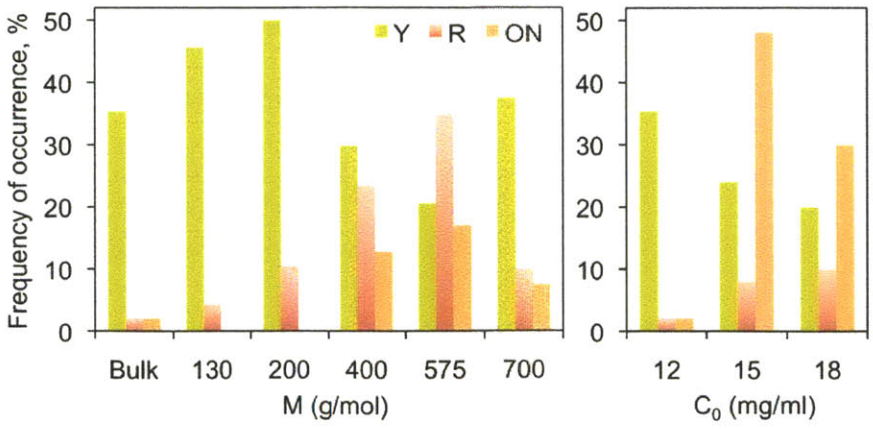

Figure 6-9. Polymorph frequency of occurrence in 12 mg/ml ROY-ethanol solution with or without microgels of various mesh sizes (left) and at higher solution concentrations, C_0 (right). Frequency of occurrence is

calculated as the percentage of samples crystallized in a particular form within 1440min out of the total number of samples. The analysis for 12 mg/ml solution is carried out on the same data set as in Figure 8.

In summary, addition of PEGDA microgels accelerated crystallization of all three forms, Y, R and ON. Particularly, nucleation of a metastable form R was preferentially induced as to become the dominant form at an optimum mesh size M=575 g/mol, whereas Y crystallized almost exclusively without any microgels. Nucleation of another metastable form ON was also promoted when M>200 g/mol, however, to a much less extent compared with R. Interestingly, ROY nucleation kinetics is extraordinarily sensitive to the variation in mesh sizes, particularly Form R.

6.3.5. Mechanistic Investigations into ROY Polymorph Selectivity

The impact of microgels on ROY polymorphic outcome can be comprehended from the perspectives of the concentration effect, the templating effect and the mesh size effect. Similar to CBZ, ROY also exhibits preferential partitioning in the gel phase (Figure 6-10), which leads to concentrations 6-11 times as high as that of the bulk solution. This result is visibly reflected in the red color of microgels (Figure 6-7f) imparted from highly concentrated ROY. Besides, the fact that $\varkappa$ is much higher at larger M indicates ROY predominantly interacts with the PEG subchain. The influence of higher solute concentration on polymorphic outcomes was investigated with bulk crystallization experiments (Figure 6-9 right). Clearly, ON became the dominant form with the increase of concentration, which is in accordance with previous reports.[127] This concentration effect could help explain accelerated nucleation of ON when microgels with M=400-700 g/mol were added (Figure 6-9 left), considering that the ROY concentration in these microgels is much higher than in others (Figure 6-10). Apparently, the concentration effect cannot fully account for the observation that crystallization of R form was particularly promoted by microgels. The strong dependence of R form nucleation kinetics and

frequency of occurrence on M suggests that the mesh size effect and the ROY-polymer interactions may have key roles to play in controlling R form nucleation.

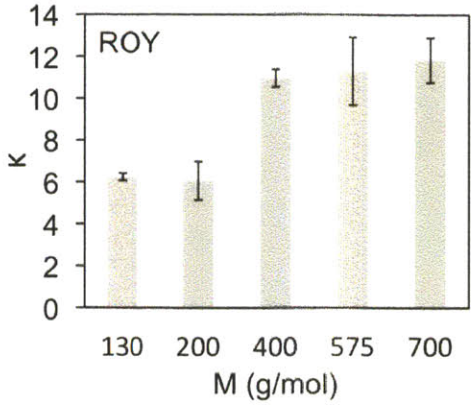

Figure 6-10. Partition coefficients of ROY in PEG_MDA microgels from ethanol solution.

The ROY-polymer interactions were probed via preferred crystal orientations on flat PEG_MDA films. From the bulk solution, ROY crystallized in Form Y predominantly (Figure 6-11). In comparison, PEG_MDA films templated nucleation of R, as well as Y, which is consistent with the observations with microgels. In particular, a few crystal facets show much stronger XRD peak intensities compared with the bulk sample, i.e., Y (020), R (111) and R (220), indicating that they are the dominant crystal facets nucleated on the polymer. To verify this observation, we quantified the contribution from each crystal facet and listed the prominent ones in Table 6-4. Interestingly, the preferred crystal orientation varies significantly as a function of M, the PEG subchain molecular weight. Polymers with M=130, 200 g/mol favor R (111) and R (220). As M increases, percentage of R decreases and Y increases to become the dominant polymorph on M=575, 700 g/mol, which is contact with the polymer via Y (020) and/or (040) facet. This observation implies that the acrylate group of PEGDA is responsible for templating R, whereas the PEG subchain induces nucleation of Y. Furthermore, it underscores the point that the polymorph crystallization is extraordinarily sensitive to polymer-solute interactions.

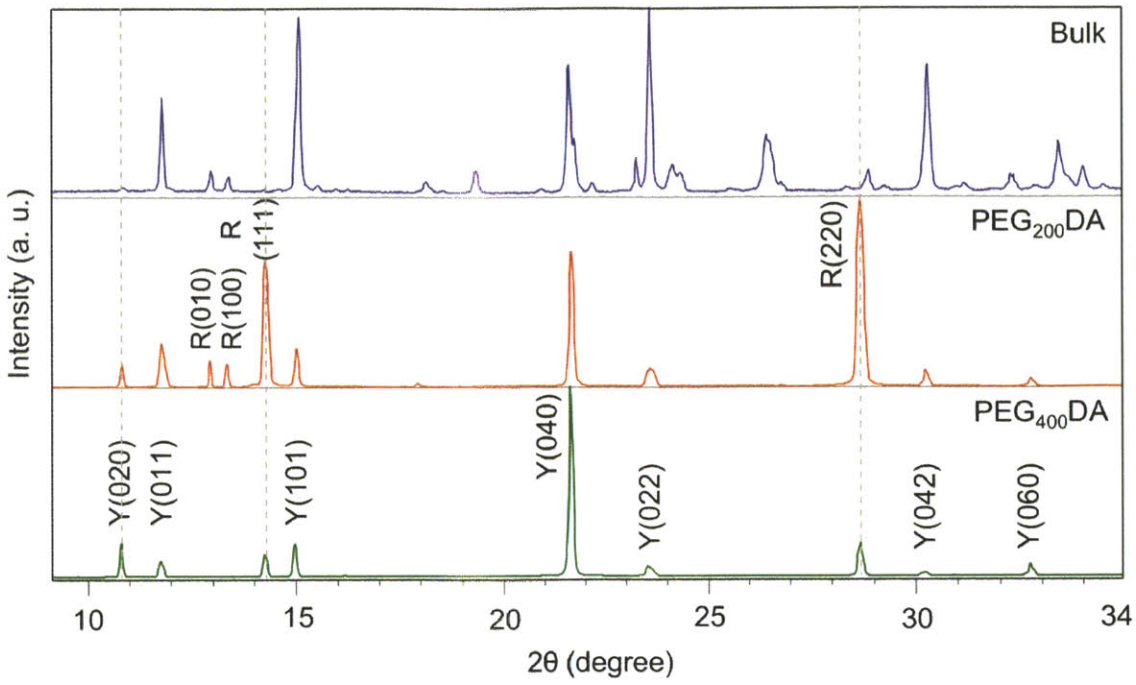

Figure 6-11. XRD patterns of ROY crystallized from bulk solution (top) and on PEGDA films (middle and bottom) under the same conditions. Additional peaks observed from crystals templated by polymer films but not from bulk crystals are marked with vertical grey dotted line. Reference patterns are calculated from CSD using POWD-12++.

Table 6-4. Percentages of ROY crystals in various orientations (hkl) on PEG_MDA polymer films.

M (g/mol)	Y (020), %	Y (040), %	R (111), %	R (220), %
130	7.5	3.4	**38.0**	**46.8**
200	3.5	1.6	**36.2**	**53.6**
400	**23.6**	9.9	**28.8**	**24.9**
575	**26.9**	13.1	12.9	20.0
700	**50.9**	16.9	9.8	14.4

Analysis on the XRD data is carried out by normalizing the measured peak intensities I_p^i with the reference peak intensities I_{bulk}^i from the bulk sample, following the formula $\eta_i = \frac{I_p^i / I_{bulk}^i}{\sum_i (I_p^i / I_{bulk}^i)} \times 100$, where η_i is the percentage of crystals in orientation *i*, and p is short for polymer. Minor orientations (<10% on all films) are considered but not shown in the table. Percentages are highlighted as bold for dominant orientations in each case.

To unveil the specific polymer-solute interactions, we examined the molecular structures of preferentially nucleated crystal facets, shown in Figure 6-12. R (111) and R (220) exhibit very

similar surface functionalities. The cyano and nitro moieties, although exposed to the surface, are engaged in ROY self-interactions, leaving the amine and methyl groups more available to interact with the polymer surface (Figure 6-12d), probably with the acrylate group as inferred from the XRD results (Table 6-4). Specifically, the amine hydrogen of ROY can form hydrogen bond with the carbonyl of acrylate group, and the methyl group of ROY can interact with acrylate by forming C-H···O contact, which is often referred to as a secondary hydrogen bond in the crystal engineering literature.[110] As for Form Y, either Y (020) or Y (040) or both were possibly templated by the polymer, which cannot be distinguished from the XRD results since they are parallel planes. However, it is unlikely for Y (040) to recognize with PEGDA, because it resembles Y (022) and Y (042) in surface chemistry (not shown), which are not favored by the polymer but are among the main facets of bulk crystals (Figure 6-11). All Y (022), (042) and (040) facets are featured with cyano and/or nitro moieties, which are more likely to engage in ROY intermolecular interactions or solvated by ethanol. Therefore, the phenolic hydrogen exposed to the Y (020) surface is inferred to be responsible for interacting with the PEG subchain (Figure 6-12d), probably by forming C-H···O contact with the ethylene oxide oxygen.

The identified specific ROY-polymer interactions can help elucidate the role of templating effect in polymorph selection. By interacting with the phenolic hydrogen of ROY, the PEG subchain brings about two effects. First, it helps align the ROY molecules in a particular orientation, and as such better exposes other moieties in ROY for self-interactions and facilitates molecular clusters formation, which is a key step to nucleation. Second, it hinders the phenolic hydrogen-nitro recognition essential to R polymorph formation (not found in other forms with known structures except for OPR) (Figure 6-13 c-d), resulting in preferential nucleation of Y polymorph on polymer films with higher M. Likewise, by hydrogen bonding with the amine

moiety of ROY, the acrylate group of the polymer interferes with the amine-cyano hydrogen bond unique to Y polymorph (not found in other forms), and as such facilitates crystallization of R polymorph.

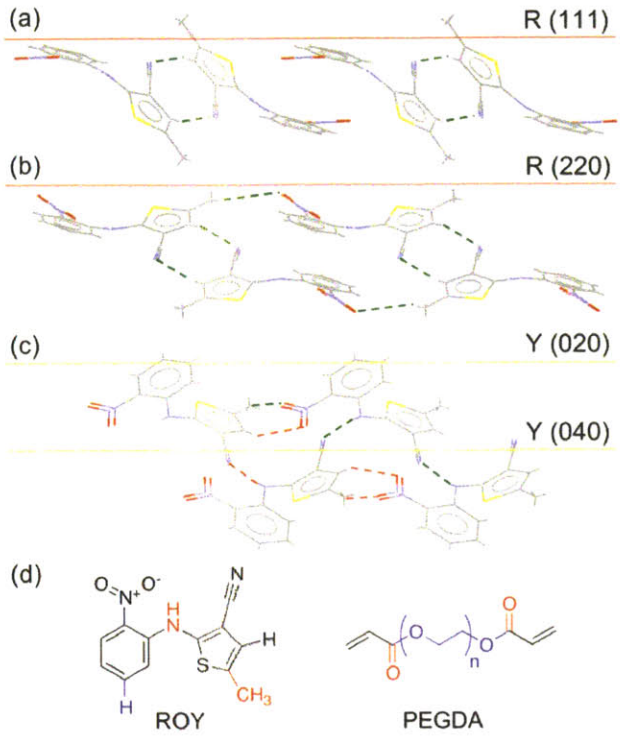

Figure 6-12. Specific polymer-ROY interactions inferred from preferred crystal orientations. (a-c) Molecular structures of ROY crystal facets preferentially grown from the polymer surface. The solid line indicates the top surface of the corresponding facet. R and Y denote red and yellow ROY polymorphs. Prominent intermolecular interactions in ROY crystals are denoted with green dotted lines if the interaction is between the two in-plane molecules as depicted, and with red dotted lines if it is between one in-plane molecule and another molecule in the next layer in through-plane direction. (d) Molecular structures of monomers of ROY and PEGDA. ROY functional groups colored blue are inferred to preferentially interact with PEG subchain, and those colored red with the acrylate group.

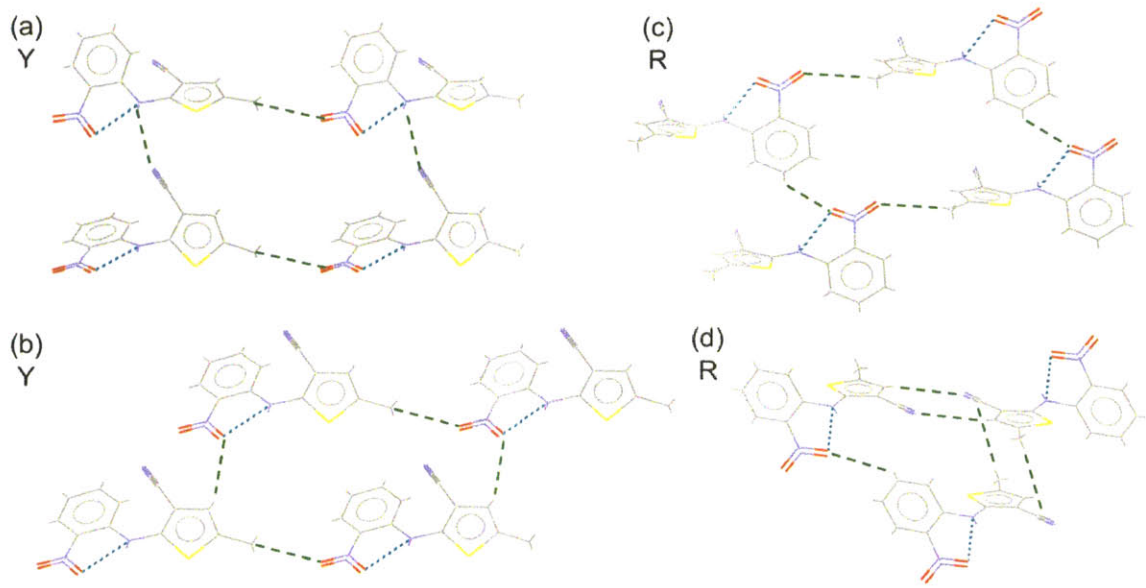

Figure 6-13. Molecular recognition motifs in ROY crystals of forms Y (a-b) and R (c-d). Green dotted line denotes intermolecular interactions, and cyan dotted line intramolecular interactions. Other supermolecular rings can form by different combinations of the same set of intermolecular interactions, however, this figure is not meant to exhaust all the molecular combinations in the ROY crystal, but to illustrate essential intermolecular interactions, which are all depicted here. π-π stacking is also present in both Y and R forms, exhibiting similar motifs (not shown here).

Following the above discussions, the templating effect of the microgels alone is expected to bias the polymorph selectivity towards R at lower M and Y at higher M. We indeed observed continuous nucleation acceleration of Form Y with the increase of M (Table 6-2, Table 6-3), however, the trend of R still cannot be fully explained with the templating effect and concentration effect combined. Now we turn our attention to the mesh size effect. We observed the existence of an optimum mesh size for expediting nucleation of R, at which point, its frequency of occurrence was kinetically driven to a maximum. We hypothesize that the optimum mesh size arises from the interplay between polymer-solute interactions and spatial confinement imposed by the polymer mesh.[80] Specifically, when the mesh size is too small, most of solute molecules are adsorbed to the tightly intertwined polymer chain given the large volume fraction of polymers, thereby reducing the molecular mobility and hindering effective solute-solute interactions essential to nucleus formation (Figure 6-14a); when the mesh size is too large, a

smaller fraction of solute is associated with the polymer and the nucleation-templating effect of the polymer due to specific polymer-solute interactions is much less significant (Figure 6-14c); at the optimum mesh size, the polymer-solute and solute-solute interactions are balanced, enabling the solute molecules aligned by adjacent polymer chains to act concertedly in forming the nucleus given appropriate spacing (Figure 6-14b). This hypothesis implies that the optimum mesh size should not be the same for polymorphs of the same compound, since their nucleation events are templated by different specific polymer-solute interactions as discussed above, and the spacing required for molecular cooperativity may differ as well. For ROY system, the separation of optimum mesh sizes between Y and R is central to the observed favorable polymorph selectivity towards R at M=575 g/mol, which overcomes the opposite trend of templating effect that favors Y with increasing M. As for the CBZ system, the mesh size effect is also evident (Table 6-1). There exhibited an optimum mesh size at M=400 g/mol corresponding to the fastest nucleation rate of Form II, whose mass fraction concurrently attained maximum. The polymorph selectivity maintained at 100% even when M increased beyond optimum, probably because the mesh size effect was counterbalanced by the templating and concentration effect, which favored Form II at higher M.

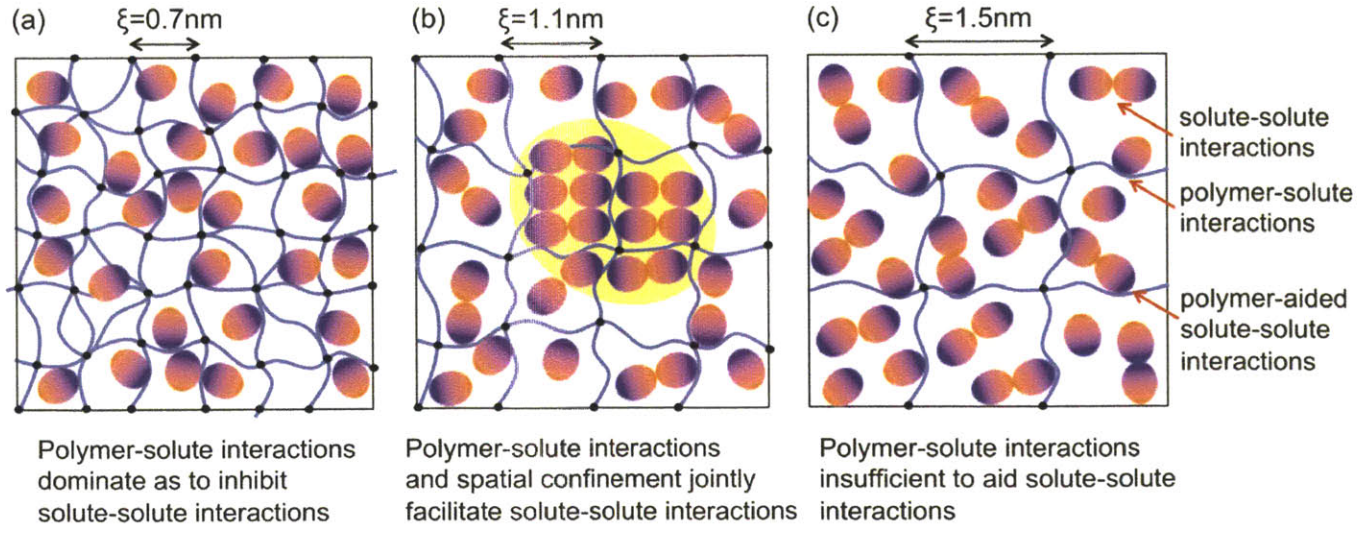

Figure 6-14. Schematic illustrating the mesh size effect on nucleation. Blue lines denote the polymer mesh with crosslinking points colored black. The polymer mesh drawn here not necessarily represents the actual physical model, but is sufficient to illustrate the role of varying confinement size. Solute molecules are signified with ellipsoids, whose one end is colored blue and preferentially interacts with the polymer chain, and the other end color colored red responsible for self-interactions. One example of such molecules is CBZ, with the blue end corresponding to the vinyl group on the azepine ring that interacts with the PEG subchain, and the red end corresponding to the carboxamide group, which dimerizes in CBZ crystals. The molar ratios of solute to monomer units constituting the polymer are drawn to scale, which are calculated from CBZ partitioning experiments. The relative size of the solute to the mesh size is also drawn to scale approximately for CBZ system. The relative fraction of solute molecules adsorbed to the polymer chain is estimated by assuming that the number of solute binding sites scales linearly with the PEG subchain length. The optimum mesh size for CBZ nucleation was found to be 1.1nm (Table 6-1). Therefore the nucleus formation is illustrated in (b) as highlighted with yellow background.

6.4. Conclusions

In conclusion, we demonstrated the polymer microgels as a promising material for controlling crystallization of polymorphs. PEGDA microgels selectively induced nucleation of Form II of CBZ, while concomitant crystallization of Form I and II were observed from bulk. In another example, the microgels improved ROY polymorph selectivity towards Form R by up to 20 times, whereas bulk crystallization predominantly produced Y or ON depending on the supersaturation. Through these examples, the polymer gels show ability to take the polymorphic system into occurrence domains not accessible through conventional methods. Furthermore, through our mechanistic investigations, we found that the nucleation-templating effect and the spatial confinement imposed by the polymer network hold key to achieving polymorph selectivity. With this insight, selective crystallization of a desired polymorph could be achieved by designing the polymer chemistry and microstructure. Our results also help advance the fundamental understanding on crystallization of polymorphs at complex interfaces, in particular, under confined environment.

Chapter 7

7. Conclusions and Future Work

7.1. Conclusions

My thesis aims at elucidating the roles of surface chemistry and nanostructure on nucleation to enable rational design of surfaces for controlling crystallization from solution. To this end, I systematically investigated the role of surface chemistry, morphology, in particular porous structures of various polymeric materials on heterogeneous nucleation using small organic molecules as model compounds.

I have demonstrated quantitatively the significance of surface chemistry to nucleation kinetics using a variety of smooth polymer surfaces. By tuning the surface composition of the polymers, aspirin nucleation was accelerated by up to an order of magnitude compared to the bulk. The mechanism of the surface chemistry effect was further investigated via interfacial free energy approach, which predicted the same trend of polymer surface nucleation activities as indicated by the nucleation induction times. This result indicates that, at thermodynamic level, it is through interfacial free energies that the surfaces influence the surface nucleation activity. Moreover, the underlying molecular interactions were probed via crystal orientation study, which revealed that the nucleation-active polymer surfaces preferentially nucleated the polar facets of aspirin, guided by hydrogen bonds.

I established nucleation induction time statistics as a powerful tool to gain insight into the mechanism of nucleation on controlled surfaces. Equipped with this tool, I found that nanoscopic pores of 50-100 nm led to up to 2 orders of magnitude faster aspirin nucleation rates when compared with surfaces without pores. I hypothesized that the shape of the nanopores, rather

than the pore size, holds key to the observed nanopore-induced nucleation. To test this hypothesis, I fabricated polymer films with surface nanopores of various shapes using a newly developed procedure Nanoparticle Imprint Lithography (NpIL) as well as the conventional UV-assisted Nanoimprint Lithography (UV-NIL). With the nanopatterned polymer films, I demonstrated for the first time that the shape of surface nanopores is essential in determining the nucleation behavior. Contrary to common belief, a rough surface can inhibit nucleation of a molecular crystal from solution depending on surface morphology. For instance, spherical nanopores ranging from 15 to 120 nm hindered nucleation, whereas angular nanopores of the same size promoted it. I also showed that favourable surface-solute interactions are required for angular nanopores to promote nucleation, and proposed that pore shape affects nucleation kinetics through the alteration of the orientational order of the crystallizing molecule near the angles of the pores, the macroscopic expression of which is 'angle-directed nucleation'.

Furthermore, the nanoconfinement effect on nucleation was investigated using polymeric microgels with tunable nanostructures and chemistry, whose mesh sizes range from 0.7-2 nm. In this study, we first demonstrated the existence of an optimum confinement size at which the rate of nucleation is dramatically enhanced by up to four orders of magnitude, the degree to which depends on the extent of polymer-solute interactions. We hypothesized that the key to controlling nucleation by nanoconfinement lies in manipulating the effective solute-solute interaction, which is strongly affected by polymer-solute interactions and the spatial confinement imposed by the polymer microstructure, the interplay of which gives rise to the observed optimum mesh size for expediting nucleation.

Understanding the roles of polymer-solute interactions as well as the polymer nanostructures, we modified the polymer chemistry and further improved the overall effectiveness of microgels

in promoting aspirin nucleation by orders of magnitude. To gain mechanistic understanding, we examined the role of polymer-solute interactions from the perspective of adsorptive partitioning and nucleation-templating effect, on the basis of which, we proposed that favorable polymer-solute interactions promote nucleation by two means. First, it leads to higher solute concentration in the gel, which enhances the effective solute-solute interactions. Second, specific polymer solute interactions, as evidenced by the preferred crystal orientation on polymers, facilitate molecular alignment along the polymer chain. Both are essential in promoting nucleus formation by enhancing density and structural fluctuations in the solution.

In addition, the microgel nanostructure was shown to play an important role in determining the crystal polymorphism of pharmaceutical compounds, which is of great importance in the pharmaceutical manufacturing process. Selective crystallization of metastable polymorphs of carbamazepine and 5-methyl-2-[(2-nitrophenyl)amino]-3-thiophenecarbonitrile (ROY) was achieved using microgels of particular nanostructures. Through our mechanistic investigations, it was found that the nucleation-templating effect and the spatial confinement imposed by the polymer network are central to achieving polymorph selectivity. With this insight, selective crystallization of a desired polymorph could be achieved by designing the polymer chemistry and microstructure.

7.2. Technical Implications

This research provided new insight into heterogeneous nucleation, which could potentially be applied to many areas of science and technology from designing 'seed' particles for regulating crystallization of various fine chemicals, to controlling pharmaceutical polymorphism, orienting biominerals on organic substrates, inhibiting ice formation on airplanes, promoting protein

nucleation for structure determination and enabling multifunctional pharmaceutical excipient and drug-delivery vehicles.

7.2.1. Application in Pharmaceutical Manufacturing

Crystallization is extensively used to purify the active pharmaceutical ingredients in the pharmaceutical manufacturing process. After the crystallization step, the API crystals are then granulated and blended with excipients in a series of solid-state operations. The granulation and blending steps are particularly problematic. They are not only plagued by poor process controllability and final product uniformity, the process parameters are also very sensitive to the properties of the drug crystals. On the other hand, the properties of the drug crystals are constantly varying due to the difficulty in controlling crystallization.

My research help enable heterogeneous crystallization of API from solution on the surface of an amorphous excipient, so that the subsequent API compaction, granulation and blending with excipients can be ultimately eliminated. Furthermore, API nucleation kinetics and final crystal form have the potential to be tuned by designing the excipient surface properties.

Design principles are devised to aid the selection of polymeric material and solvent for crystallizing a given API. To facilitate API nucleation on the excipient, the chemical makeup of the excipient and the solvent should be selected such that the API interacts stronger with the excipient than with solvent molecules (the 'Interaction Criterion'). Hansen parameters can help in the selection of the polymer chemistry that satisfy this interaction criterion. The distance 'd' in the Hansen parameter space provides a semi-quantitative measure for the extent of interaction. We were able to show that 'd' is correlated with 'κ', the partition coefficient of API in the polymer gel from solution, which serves to measure the interaction between API and the polymer. The interaction between the API and solvent is indicated from the API solubility, and

the interaction between the polymer and the solvent can be judged from the degree of gel swelling. According to the 'Interaction Criterion', it is desired to have API partitioning as high as possible, and API solubility and gel swelling as low as possible. However, practically speaking, a stable microgel suspension is needed as well as a reasonable API crystal yield, which requires high degree of gel swelling and high API solubility. To balance the two requirements, the second criterion for selecting appropriate polymer chemistry is to have intermediate gel swelling and API solubility.

7.2.2. Application in Drug Delivery

Recent years have seen great enthusiasm in making nanoscopic drug particles to improve the bioavailability of hydrophobic compounds and to release the drug in a controlled manner from a biocompatible nanoporous matrix. Typically, the drug particles are either broken down mechanically to reduce to desired sizes or are physically absorbed into nanoporous matrix in amorphous state. However, these methods are not ideal because the drugs are prone to phase transformation under mechanical stress or to recrystallize since the amorphous form is metastable. My research opens up the possibility of direct crystallization in the drug carrier and of making nanocrystals in nanoporous polymer matrix to enhance drug availability.

7.3. Future Work

Our results on the role nanopore shape in surface-induced nucleation provide a good starting point and outline an intriguing concept. However, much more work needs to be done before our hypothesis can be fully verified and the concept taken to practical applications. Several directions worth pursuing are listed below.

1. Investigate an array of pore shapes and expand beyond spherical, square and hexagon nanopores. The technical challenge involved is to improve the current lithographic

method to nanopattern the polymer surface in a more robust and cost-effective manner. Interference Lithography can be further explored for making parallelogram-shaped nanoposts on the imprint mold. Nanocrystals of various shapes can be synthesized for templating pores of diverse shapes. However, it is still challenging and time consuming to perfect a synthesis method and obtain nanocrystals with desired crystal habits and well-defined edges.

2. Develop method for nanopatterning pharmaceutically accepted polymeric materials. The current method makes use of UV polymerization for making highly crosslinked polymer films. However, these materials are not FDA approved as of now, preventing them from being applied to pharmaceutical manufacturing process. New method may be explored for templating existing polymeric excipients, such as hot embossing, or the conventional Nanoimprint Lithopraphy.
3. Perform Molecular Dynamic simulations to elucidate the molecular level mechanism of the nanopore shape effect. We hyphothesized the pore shape influences nucleation by altering the molecular orientational order near the pore angles. This hyphothesis could be examined using computational methods.
4. Explore the nanopore shape effect on crystallization of polymorphs. If our hyphothesis is valid, the shape of the nanopores should be able to affect polymorphic outcomes of crystallization considering that each polymorph modification possesses distinctive sets of intrinsic angles.

Regarding the research topic of controlled nucleation and polymorphism using polymer gels, future investigations may include: verify the mesh size effect via Molecular Dynamic combined with kinetic Monte Carlo simultations and develop lattice model to formulate the phenomena

mathematically; further the mechanistic understanding on the role of intermolecular interactions since the ideal material chemistry for inducing nucleation of a given compound cannot be fully predicted yet, given the complexity of solvent effect and the collective importance of weak van der Waals interactions.

Cited References

(1) Ward, M. D. *Chemical Reviews* **2001**, *101*, 1697.

(2) Mullin, J. W. *Crystallization*; 4th ed.; Butterworth-Heinemann: Oxford ; Boston, 2001.

(3) Debenedetti, P. G. *Metastable liquids : concepts and principles*; Princeton University Press: Princeton, N.J., 1996.

(4) Turnbull, D. *Journal of Chemical Physics* **1950**, *18*, 198.

(5) Vishweshwar, P.; McMahon, J. A.; Oliveira, M.; Peterson, M. L.; Zaworotko, M. J. *Journal of the American Chemical Society* **2005**, *127*, 16802.

(6) Price, C. P.; Grzesiak, A. L.; Matzger, A. J. *Journal of the American Chemical Society* **2005**, *127*, 5512.

(7) Kashchiev, D. *Nucleation : basic theory with applications*; Butterworth Heinemann: Oxford ; Boston, 2000.

(8) Santiso, E. E.; Trout, B. L. *Journal of Chemical Physics* **2011**, *134*.

(9) Beckham, G. T.; Peters, B.; Starbuck, C.; Variankaval, N.; Trout, B. L. *Journal of the American Chemical Society* **2007**, *129*, 4714.

(10) tenWolde, P. R.; Frenkel, D. *Science* **1997**, *277*, 1975.

(11) Oxtoby, D. W. *Accounts of Chemical Research* **1998**, *31*, 91.

(12) Erdemir, D.; Lee, A. Y.; Myerson, A. S. *Accounts of Chemical Research* **2009**, *42*, 621.

(13) Granasy, L.; Pusztai, T.; Saylor, D.; Warren, J. A. *Physical Review Letters* **2007**, *98*.

(14) Oxtoby, D. W. *Annual Review of Materials Research* **2002**, *32*, 39.

(15) Talanquer, V.; Oxtoby, D. W. *Journal of Chemical Physics* **1996**, *104*, 1483.

(16) Vekilov, P. G. *Crystal Growth & Design* **2004**, *4*, 671.

(17) Yau, S. T.; Vekilov, P. G. *Nature* **2000**, *406*, 494.

(18) Zhang, T. H.; Liu, X. Y. *Journal of the American Chemical Society* **2007**, *129*, 13520.

(19) Dey, A.; Bomans, P. H. H.; Muller, F. A.; Will, J.; Frederik, P. M.; de With, G.; Sommerdijk, N. *Nature Materials* **2010**, *9*, 1010.

(20) Vekilov, P. G. *Crystal Growth & Design* **2010**, *10*, 5007.

(21) Piana, S.; Reyhani, M.; Gale, J. D. *Nature* **2005**, *438*, 70.

(22) Piana, S.; Gale, J. D. *Journal of the American Chemical Society* **2005**, *127*, 1975.

(23) Gasser, U.; Weeks, E. R.; Schofield, A.; Pusey, P. N.; Weitz, D. A. *Science* **2001**, *292*, 258.

(24) Nellas, R. B.; Chen, B. *Physical Chemistry Chemical Physics* **2008**, *10*, 506.

(25) Gebauer, D.; Volkel, A.; Colfen, H. *Science* **2008**, *322*, 1819.

(26) Aizenberg, J.; Black, A. J.; Whitesides, G. M. *Nature* **1999**, *398*, 495.

(27) Aizenberg, J. *Advanced Materials* **2004**, *16*, 1295.

(28) Weissbuch, I.; Lahav, M.; Leiserowitz, L. *Crystal Growth & Design* **2003**, *3*, 125.

(29) Mao, G. Z.; Chen, D. Z.; Handa, H.; Dong, W. F.; Kurth, D. G.; Mohwald, H. *Langmuir* **2005**, *21*, 578.

(30) Tkatchenko, A. *Physical Review B* **2007**, *75*, 6.

(31) Carter, P. W.; Ward, M. D. *Journal of the American Chemical Society* **1994**, *116*, 769.

(32) Hooks, D. E.; Fritz, T.; Ward, M. D. *Advanced Materials* **2001**, *13*, 227.

(33) Carter, P. W.; Hillier, A. C.; Ward, M. D.; Mw *Journal of the American Chemical Society* **1994**, *116*, 944.

(34) Bonafede, S. J.; Ward, M. D. *Journal of the American Chemical Society* **1995**, *117*, 7853.

(35) Carter, P. W.; Ward, M. D. *Journal of the American Chemical Society* **1993**, *115*, 11521.

(36) Capes, J. S.; Cameron, R. E. *Crystengcomm* **2007**, *9*, 84.

(37) Grzesiak, A. L.; Matzger, A. J. *Journal of Pharmaceutical Sciences* **2007**, *96*, 2978.

(38) Grzesiak, A. L.; Uribe, F. J.; Ockwig, N. W.; Yaghi, O. M.; Matzger, A. J. *Angewandte Chemie-International Edition* **2006**, *45*, 2553.

(39) Lang, M. D.; Grzesiak, A. L.; Matzger, A. J. *Journal of the American Chemical Society* **2002**, *124*, 14834.

(40) Briseno, A. L.; Aizenberg, J.; Han, Y. J.; Penkala, R. A.; Moon, H.; Lovinger, A. J.; Kloc, C.; Bao, Z. A. *Journal of the American Chemical Society* **2005**, *127*, 12164.

(41) Singh, A.; Lee, I. S.; Myerson, A. S. *Crystal Growth & Design* **2009**, *9*, 1182.

(42) Gavish, M.; Wang, J. L.; Eisenstein, M.; Lahav, M.; Leiserowitz, L.; Ht *Science* **1992**, *256*, 815.

(43) Hiremath, R.; Basile, J. A.; Varney, S. W.; Swift, J. A. *Journal of the American Chemical Society* **2005**, *127*, 18321.

(44) Curcio, E.; Curcio, V.; Di Profio, G.; Fontananova, E.; Drioli, E. *Journal of Physical Chemistry B* **2010**, *114*, 13650.

(45) Briseno, A. L.; Mannsfeld, S. C. B.; Ling, M. M.; Liu, S. H.; Tseng, R. J.; Reese, C.; Roberts, M. E.; Yang, Y.; Wudl, F.; Bao, Z. N. *Nature* **2006**, *444*, 913.

(46) van Meel, J. A.; Sear, R. P.; Frenkel, D. *Physical Review Letters* **2010**, *105*, 4.

(47) Sear, R. P. *Journal of Physics-Condensed Matter* **2002**, *14*, 3693.

(48) Page, A. J.; Sear, R. P. *Journal of the American Chemical Society* **2009**, *131*, 17550.

(49) Cacciuto, A.; Auer, S.; Frenkel, D. *Nature* **2004**, *428*, 404.

(50) de Villeneuve, V. W. A.; Dullens, R. P. A.; Aarts, D.; Groeneveld, E.; Scherff, J. H.; Kegel, W. K.; Lekkerkerker, H. N. W. *Science* **2005**, *309*, 1231.

(51) Page, A. J.; Sear, R. P. *Physical Review Letters* **2006**, *97*.

(52) Beiner, M.; Rengarajan, G. T.; Pankaj, S.; Enke, D.; Steinhart, M. *Nano Letters* **2007**, *7*, 1381.

(53) Frenkel, D. *Nature* **2006**, *443*, 641.

(54) Ha, J. M.; Wolf, J. H.; Hillmyer, M. A.; Ward, M. D. *Journal of the American Chemical Society* **2004**, *126*, 3382.

(55) Aizenberg, J.; Black, A. J.; Whitesides, G. H. *Journal of the American Chemical Society* **1999**, *121*, 4500.

(56) Bunker, B. C.; Rieke, P. C.; Tarasevich, B. J.; Campbell, A. A.; Fryxell, G. E.; Graff, G. L.; Song, L.; Liu, J.; Virden, J. W.; McVay, G. L. *Science* **1994**, *264*, 48.

(57) Lee, A. Y.; Lee, I. S.; Dettet, S. S.; Boerner, J.; Myerson, A. S. *Journal of the American Chemical Society* **2005**, *127*, 14982.

(58) Berman, A.; Ahn, D. J.; Lio, A.; Salmeron, M.; Reichert, A.; Charych, D. *Science* **1995**, *269*, 515.

(59) Cox, J. R.; Ferris, L. A.; Thalladi, V. R. *Angewandte Chemie-International Edition* **2007**, *46*, 4333.

(60) D'Souza, S. M.; Alexander, C.; Carr, S. W.; Waller, A. M.; Whitcombe, M. J.; Vulfson, E. N. *Nature* **1999**, *398*, 312.

(61) Chen, J. R.; Wakida, T. *Journal of Applied Polymer Science* **1997**, *63*, 1733.

(62) Fowkes, F. M. *Industrial and Engineering Chemistry* **1964**, *56*, 40.

(63) Laval, P.; Crombez, A.; Salmon, J. B. *Langmuir* **2009**, *25*, 1836.

(64) Knezic, D.; Zaccaro, J.; Myerson, A. S. *Journal of Physical Chemistry B* **2004**, *108*, 10672.

(65) Barlow, T. W.; Haymet, A. D. J. *Review of Scientific Instruments* **1995**, *66*, 2996.

(66) Tanaka, H. *Physical Review Letters* **1993**, *71*, 3158.

(67) Chayen, N. E.; Saridakis, E.; Sear, R. P. *Proceedings of the National Academy of Sciences of the United States of America* **2006**, *103*, 597.

(68) Chayen, N. E.; Saridakis, E.; El-Bahar, R.; Nemirovsky, Y. *Journal of Molecular Biology* **2001**, *312*, 591.

(69) Jackson, C. L.; McKenna, G. B. *Chemistry of Materials* **1996**, *8*, 2128.

(70) Maheshwari, P.; Dutta, D.; Sharma, S. K.; Sudarshan, K.; Pujari, P. K.; Majumder, M.; Pahari, B.; Bandyopadhyay, B.; Ghoshray, K.; Choshray, A. *Journal of Physical Chemistry C* **2010**, *114*, 4966.

(71) Ha, J. M.; Hamilton, B. D.; Hillmyer, M. A.; Ward, M. D. *Crystal Growth & Design* **2009**, *9*, 4766.

(72) Hamilton, B. D.; Hillmyer, M. A.; Ward, M. D. *Crystal Growth & Design* **2008**, *8*, 3368.

(73) Sommerdijk, N.; de With, G. *Chemical Reviews* **2008**, *108*, 4499.

(74) Harrison, A.; Ibberson, R.; Robb, G.; Whittaker, G.; Wilson, C.; Youngson, D. *Faraday Discussions* **2003**, *122*, 363.

(75) Heng, J. Y. Y.; Bismarck, A.; Lee, A. F.; Wilson, K.; Williams, D. R. *Journal of Pharmaceutical Sciences* **2007**, *96*, 2134.

(76) K., O. D.; C., W. R.; Journal of Applied Polymer Science: 1969; Vol. 13, p 1741.

(77) Diao, Y.; Myerson, A. S.; Hatton, T. A.; Trout, B. L. *Langmuir* **2011**, *27*, 5324.

(78) Hamilton, B. D.; Weissbuch, I.; Lahav, M.; Hillmyer, M. A.; Ward, M. D. *Journal of the American Chemical Society* **2009**, *131*, 2588.

(79) Harada, T.; Hatton, T. A. *Langmuir* **2009**, *25*, 6407.

(80) Diao, Y.; Helgeson, M. E.; Myerson, A. S.; Hatton, T. A.; Doyle, P. S.; Trout, B. L. *Journal of the American Chemical Society* **2011**, *133*, 3756.

(81) Stewart, M. D.; Willson, C. G. *Mrs Bulletin* **2005**, *30*, 947.

(82) Xia, Y. N.; Gates, B.; Yin, Y. D.; Lu, Y. *Advanced Materials* **2000**, *12*, 693.

(83) Trujillo, N. J.; Baxamusa, S. H.; Gleason, K. K. *Chemistry of Materials* **2009**, *21*, 742.

(84) Savas, T. A.; Schattenburg, M. L.; Carter, J. M.; Smith, H. I. *Journal of Vacuum Science & Technology B* **1996**, *14*, 4167.

(85) Hammond, R. B.; Pencheva, K.; Roberts, K. J. *Crystal Growth & Design* **2006**, *6*, 1324.

(86) Li, T.; Li, B.; Tomassone, M. S. *Chemical Engineering Science* **2006**, *61*, 5159.

(87) Dendukuri, D.; Gu, S. S.; Pregibon, D. C.; Hatton, T. A.; Doyle, P. S. *Lab on a Chip* **2007**, *7*, 818.

(88) Peppas, N. A.; Hilt, J. Z.; Khademhosseini, A.; Langer, R. *Advanced Materials* **2006**, *18*, 1345.

(89) Canal, T.; Peppas, N. A. *Journal of Biomedical Materials Research* **1989**, *23*, 1183.

(90) Cruise, G. M.; Scharp, D. S.; Hubbell, J. A. *Biomaterials* **1998**, *19*, 1287.

(91) Merrill, E. W.; Dennison, K. A.; Sung, C. *Biomaterials* **1993**, *14*, 1117.

(92) Ravi, N.; Mitra, A.; Hamilton, P.; Horkay, F. *Journal of Polymer Science Part B-Polymer Physics* **2002**, *40*, 2677.

(93) Nichols, G.; Frampton, C. S. *Journal of Pharmaceutical Sciences* **1998**, *87*, 684.

(94) Peterson, M. L.; Morissette, S. L.; McNulty, C.; Goldsweig, A.; Shaw, P.; LeQuesne, M.; Monagle, J.; Encina, N.; Marchionna, J.; Johnson, A.; Gonzalez-Zugasti, J.; Lemmo, A. V.; Ellis, S. J.; Cima, M. J.; Almarsson, O. *Journal of the American Chemical Society* **2002**, *124*, 10958.

(95) Di Profio, G.; Tucci, S.; Curcio, E.; Drioli, E. *Chemistry of Materials* **2007**, *19*, 2386.

(96) Mellott, M. B.; Searcy, K.; Pishko, M. V. *Biomaterials* **2001**, *22*, 929.

(97) Martin, J. E.; Wilcoxon, J.; Odinek, J. *Physical Review A* **1991**, *43*, 858.

(98) Edholm, O.; Blomberg, C. *Chemical Physics* **2000**, *252*, 221.

(99) Konno, H.; Taylor, L. S. *Journal of Pharmaceutical Sciences* **2006**, *95*, 2692.

(100) Vidal, O.; Robert, M. C.; Boue, F. *Journal of Crystal Growth* **1998**, *192*, 271.

(101) Diao, Y.; Harada, T.; Myerson, A. S.; Hatton, T. A.; Trout, B. L. *Nature Materials* **2011**.

(102) Kline, S. R. *Journal of Applied Crystallography* **2006**, *39*, 895.

(103) Debye, P.; Bueche, A. M. *Journal of Applied Physics* **1949**, *20*, 518.

(104) Gennes, P.-G. d. *Scaling concepts in polymer physics*; Cornell University Press: Ithaca, N.Y., 1979.

(105) Hammouda, B. *Advances in Polymer Science* **1993**, *106*, 87.

(106) Hecht, A. M.; Horkay, F.; Schleger, P.; Geissler, E. *Macromolecules* **2002**, *35*, 8552.

(107) Shibayama, M. *Macromolecular Chemistry and Physics* **1998**, *199*, 1.

(108) Lee, A. G.; Arena, C. P.; Beebe, D. J.; Palecek, S. P. *Biomacromolecules* **2010**, *11*, 3316.

(109) Ho, D. L.; Hammouda, B.; Kline, S. R. *Journal of Polymer Science Part B-Polymer Physics* **2003**, *41*, 135.

(110) Steiner, T. *Chemical Communications* **1997**, 727.

(111) Bernstein, J. *Polymorphism in molecular crystals*; Oxford University Press: OxfordClarendon Press ; New York, 2002.

(112) Rodriguez-Hornedo, N. *Journal of Pharmaceutical Sciences* **1999**, *88*, 651.

(113) Davey, R. J.; Allen, K.; Blagden, N.; Cross, W. I.; Lieberman, H. F.; Quayle, M. J.; Righini, S.; Seton, L.; Tiddy, G. J. T. *Crystengcomm* **2002**, 257.

(114) Chen, S. A.; Xi, H. M.; Yu, L. *Journal of the American Chemical Society* **2005**, *127*, 17439.

(115) Desgranges, C.; Delhommelle, J. *Journal of the American Chemical Society* **2006**, *128*, 15104.

(116) Bernstein, J. *Crystal Growth & Design* **2011**, *11*, 632.

(117) Bernstein, J.; Davey, R. J.; Henck, J. O. *Angewandte Chemie-International Edition* **1999**, *38*, 3441.

(118) Olmsted, B. K.; Ward, M. D. *Crystengcomm* **2011**, *13*, 1070.

(119) Allen, K.; Davey, R. J.; Ferrari, E.; Towler, C.; Tiddy, G. J.; Jones, M. O.; Pritchard, R. G. *Crystal Growth & Design* **2002**, *2*, 523.

(120) Nicholson, C. E.; Chen, C.; Mendis, B.; Cooper, S. J. *Crystal Growth & Design* **2011**, *11*, 363.

(121) Diao, Y.; Helgeson, M. E.; Siam, Z. A.; S., D. P.; Myerson, A. S.; Hatton, T. A.; Trout, B. L. Submitted, 2011.

(122) Grzesiak, A. L.; Lang, M. D.; Kim, K.; Matzger, A. J. *Journal of Pharmaceutical Sciences* **2003**, *92*, 2260.

(123) Yu, L. *Accounts of Chemical Research* **2010**, *43*, 1257.

(124) Kelly, R. C.; Rodriguez-Hornedo, N. *Organic Process Research & Development* **2009**, *13*, 1291.

(125) Lang, M. D.; Kampf, J. W.; Matzger, A. J. *Journal of Pharmaceutical Sciences* **2002**, *91*, 1186.

(126) Yu, L.; Stephenson, G. A.; Mitchell, C. A.; Bunnell, C. A.; Snorek, S. V.; Bowyer, J. J.; Borchardt, T. B.; Stowell, J. G.; Byrn, S. R. *Journal of the American Chemical Society* **2000**, *122*, 585.

(127) Hilden, J. L.; Reyes, C. E.; Kelm, M. J.; Tan, J. S.; Stowell, J. G.; Morris, K. R. *Crystal Growth & Design* **2003**, *3*, 921.

(128) Nokhodchi, A.; Bolourtchian, N.; Dinarvand, R. *Journal of Crystal Growth* **2005**, *274*, 573.

(129) Getsoian, A.; Lodaya, R. M.; Blackburn, A. C. *International Journal of Pharmaceutics* **2008**, *348*, 3.

(130) Alvarez, A. J.; Singh, A.; Myerson, A. S. *Crystal Growth & Design* **2009**, *9*, 4181.